1 Quantitative live-cell imaging and computational modelling yield novel insight
2 into endogenous WNT/CTNNB1 signaling dynamics

3 Author information

4 S.M.A. de Man[1], G. Zwanenburg[2,^], T. van der Wal[1], M.A. Hink[3,4,*,^], R. van Amerongen[1,*,^,#]

5 [1] Developmental, Stem Cell and Cancer Biology, Swammerdam Institute for Life Sciences, University
6 of Amsterdam, Amsterdam, The Netherlands

7 [2] Biosystems Data Analysis, Swammerdam Institute for Life Sciences, University of Amsterdam,
8 Amsterdam, The Netherlands

9 [3] Molecular Cytology, Swammerdam Institute for Life Sciences, University of Amsterdam,
10 Amsterdam, the Netherlands

11 [4] van Leeuwenhoek Centre for Advanced Microscopy, Swammerdam Institute for Life Sciences,
12 University of Amsterdam, Amsterdam, the Netherlands

13 * These authors contributed equally

14 ^ corresponding authors: r.vanamerongen@uva.nl (RvA, lead contact), m.a.hink@uva.nl (MAH),
15 g.zwanenburg@uva.nl (GZ)

16 # Twitter: @wntlab

1

Abstract

WNT/CTNNB1 signaling regulates tissue development and homeostasis in all multicellular animals. Multiple aspects of the underlying molecular mechanism remain poorly understood and critical information on endogenous WNT/CTNNB1 signaling dynamics is missing. Here we combine CRISPR/Cas9-mediated genome editing and quantitative live-cell microscopy to measure diffusion characteristics of fluorescently tagged, endogenous CTNNB1 in human cells with high spatiotemporal resolution under both physiological and oncogenic conditions. State-of-the-art functional imaging reveals that a substantial fraction of CTNNB1 resides in slow-diffusing complexes in the cytoplasm, irrespective of the activation status of the pathway. The identity of this cytoplasmic CTNNB1 complex changes according to the phosphorylation status of CTNNB1 as it undergoes a major reduction in size when WNT/CTNNB1 is (hyper)activated. We also measure the concentration of complexed and free CTNNB1 in both the cytoplasm and the nucleus before and after WNT stimulation, and use these parameters to build a minimal computational model of WNT/CTNNB1 signaling. Using this integrated experimental and computational approach, our work reveals that WNT pathway activation regulates the dynamic distribution of CTNNB1 across different functional pools by modulating three regulatory nodes: the cytoplasmic destruction complex, nucleocytoplasmic shuttling and nuclear retention.

Introduction

36   WNT signaling is one of the most ancient pattern-forming cell signaling cascades. It drives

37   many biological processes from the onset of embryogenesis until adulthood in all multicellular

38   animals (reviewed in van Amerongen and Nusse, 2009; Holstein, 2012; Loh et al., 2016). WNT

39   signaling remains important throughout the lifespan of the organism and controls stem cell

40   maintenance in many mammalian tissues, including the breast, intestine and skin (van

41   Amerongen et al., 2012; Barker et al., 2007; Lim et al., 2013). Disruption of the pathway causes

42   disease, with hyperactivation being a frequent event in human colorectal and other cancers

43   (reviewed in Nusse & Clevers, 2017; Wiese, Nusse, & van Amerongen, 2018).

44   The key regulatory event in WNT/CTNNB1 signaling (traditionally known as 'canonical WNT

45   signaling') is the accumulation and nuclear translocation of the transcriptional co-activator

46   beta-catenin (CTNNB1) (Figure 1A). In the absence of WNT signaling, rapid turnover by the

47   so-called destruction complex maintains low levels of CTNNB1. This cytoplasmic complex

48   consists of the scaffold proteins APC and AXIN, which bind CTNNB1, and the serine/threonine

49   kinases CSNK1 and GSK3, which subsequently phosphorylate residues S45, T41, S37 and S33

50   (Amit et al., 2002; Liu et al., 2002). This primes CTNNB1 for ubiquitination by E3 Ubiquitin

51   Protein Ligase BTRC and subsequent proteasomal degradation (Aberle et al., 1997; Latres et

52   al., 1999). In the current working model for WNT/CTNNB1 signaling, binding of WNT ligands

53   to the FZD/LRP receptor complex sequesters and inhibits the destruction complex at the

54   membrane in a process that involves DVL (Bilic et al., 2007; Schwarz-Romond et al., 2007).

55   This allows newly synthesized CTNNB1 to accumulate. Upon stimulation, CTNNB1 also

56   translocates to the nucleus, where CTNNB1 binds to TCF/LEF transcription factors to regulate

57   target gene transcription as part of a larger transcriptional complex (Behrens et al., 1996;

58   Fiedler et al., 2015; Molenaar et al., 1996; van Tienen et al., 2017).

59 The working model for WNT/CTNNB1 signaling described above is the result of almost 40

60 years of research. The use of traditional genetic and biochemical approaches has allowed

61 identification of the core players, as well as dissection of the main signaling events. However,

62 multiple aspects of WNT/CTNNB1 signaling remain poorly understood. For instance the exact

63 molecular composition of the destruction complex as well as the mechanism for its inhibition

64 remain unclear (reviewed in Tortelote et al., 2017), and how WNT/CTNNB1 signaling regulates

65 the subcellular distribution of CTNNB1 requires further scrutiny.

66 Most biochemical techniques lead to loss of spatial information and averaging of cell-to-cell

67 heterogeneity, since proteins are extracted from their cellular context. Additionally, temporal

68 information is usually limited to intervals of several minutes or hours. Live-cell microscopy

69 offers better spatiotemporal resolution. Currently, however, many of these studies are

70 conducted by overexpressing the protein(s) of interest. This can severely affect activation,

71 localization and complex formation (Gibson et al., 2013; Mahen et al., 2014). Although

72 stabilization of CTNNB1 by WNT signaling has been extensively studied, very few studies have

73 focused on the spatiotemporal dynamics of this process – especially at the endogenous level

74 (Chhabra et al., 2019; Massey et al., 2019; Rim et al., 2020).

75 Here we use CRISPR/Cas9 mediated genome editing in haploid cells to generate clonal cell

76 lines that express fluorescently tagged CTNNB1. Using confocal imaging and automated cell

77 segmentation we quantify the dynamic subcellular increase of endogenous CTNNB1 upon

78 WNT stimulation. Moreover, using Fluorescence Correlation Spectroscopy (FCS) and Number

79 and Brightness (N&B) analysis we measure the mobility and concentration of CTNNB1,

80 providing detailed information on CTNNB1 containing complexes in the cytoplasm and

81 nucleus. Next, we use these biophysical parameters to build a computational model of

82   WNT/CTNNB1 signaling that predicts the levels and subcellular distribution of CTNNB1 across

83   its cytoplasmic and nuclear pools. Using this integrated experimental and computational

84   approach, we find that WNT regulates the dynamic distribution of CTNNB1 across different

85   functional pools by modulating three regulatory nodes: cytoplasmic destruction,

86   nucleocytoplasmic shuttling and nuclear retention. Finally, we strengthen the link between

87   our data and the model via specific experimental perturbations, which shows that the

88   regulatory nodes responsible for nuclear retention and nuclear shuttling of CTNNB1 are

89   equally important under physiological and oncogenic conditions.

90   ## Results

91   ### Generation and functional validation of clonal HAP1$^{SGFP2\text{-}CTNNB1}$ cell lines

92   To visualize and quantify the spatiotemporal dynamics of WNT/CTNNB1 signaling at the

93   endogenous level, we fluorescently tagged CTNNB1 in mammalian cells using CRISPR/Cas9

94   mediated homology directed repair (Ran et al., 2013) (Figure 1). To preserve the existing

95   (epi)genetic control mechanisms of *CTNNB1* expression, only the coding sequence for SGFP2,

96   a monomeric, bright and photostable green fluorescent protein (Kremers et al., 2007), was

97   seamlessly inserted at the starting ATG of the *CTNNB1* coding sequence in HAP1 cells, a WNT-

98   responsive near haploid cell line (Figure 1B, Figure 1 supplement 2A)(Andersson et al., 1987;

99   Carette et al., 2011; Kotecki et al., 1999; Lebensohn et al., 2016). The choice for this haploid

100   cell line ensured homozygous tagging of CTNNB1 (Figure 1C), thus overcoming the limitations

101   of polyploid cell lines where genome editing often results in a combination of correctly and

102   incorrectly edited alleles (Canaj et al., 2019).

103   We isolated clonal cell lines with the desired modification by FACS sorting (Figure 1D-F) with

104   a gating strategy that specifically selected for haploid cells (Figure 1 supplement 1) as HAP1

5

105 cells can become diploid or polyploid over time (Essletzbichler et al., 2014; Yaguchi et al.,

106 2018). Genome editing of wild-type HAP1 (HAP1^{WT}) cells resulted in a small population with

107 low SGFP2 fluorescence (0.2%) (Figure 1D-E). The intensity, but not the number of cells in this

108 population increased upon treatment with CHIR99021, a potent and selective GSK3 inhibitor

109 (Bain et al., 2007), providing a strong indication that these fluorescent events corresponded

110 to HAP1 cells in which the *SGFP2* sequence was successfully knocked into the endogenous

111 *CTNNB1* locus (HAP1$^{SGFP2-CTNNB1}$) (Figure 1F). While scarless tagging of endogenous genes in

112 HAP1 cells was relatively cumbersome (only 0.2% gated events), PCR based screening and

113 sanger sequencing revealed that the desired repair occurred with almost 90% efficiency

114 within this population (Figure 1 supplement 2).

115 **Figure 1:** Generation of HAP1$^{SGFP2-CTNNB1}$ cell lines. A) Cartoon depicting the current model of the WNT/CTNNB1 pathway. In the absence of
116 WNT ligands (left, "OFF"), free cytoplasmic CTNNB1 is captured by the destruction complex consisting of AXIN, APC, CSNK1 and GSK3, which
117 leads to its phosphorylation, BTRC mediated ubiquitination and subsequent proteasomal degradation, resulting in low levels of CTNNB1 in
118 the cytoplasm and nucleus. Binding of the WNT protein (right, "ON") to the FZD and LRP receptors inhibits the destruction complex through
119 DVL. CTNNB1 accumulates in the cytoplasm and subsequently translocates to the nucleus, where it promotes the transcription of target
120 genes, such as AXIN2, as a co-activator of TCF/LEF transcription factors. B) Cartoon depicting exon 2 of the *CTNNB1* locus, which contains
121 the start codon, and the CTNNB1 protein before (top) and after (bottom) introduction of the SGFP2 by CRISPR/Cas9 mediated homology
122 directed repair. C) Schematic of the experimental workflow and timeline for generating HAP1$^{SGFP2-CTNNB1}$ clones. Cas9, gRNA and repair
123 templates are transfected as plasmids. The repair template contains the coding sequence of SGFP2 surrounded by 800 bp homology arms
124 on either side and lacks the gRNA recognition site (see supplement 2 of this figure). A short puromycin selection step is included from 24-48
125 hours after transfection to enrich for transfected cells. Haploid, GFP-positive cells are sorted and single cell clones are expanded for further
126 analysis. D-F) FACS plots illustrating control (D) and SGFP2-CTNNB1 tagged cells (E-F). D) Cells transfected with Cas9 and gRNA in the absence
127 of a repair template were used to set the gate for SGFP2-positive events. E) A small population of cells expressing low levels of SGFP2 can
128 be detected when cells are transfected with Cas9, gRNA and repair template. F) Treatment for 24 hours of cells similar to those depicted in
129 (D) with 8µM CHIR99021 does not change the amount of cells that are SGFP2 positive, but increases the SFP2 signal, most likely reflecting
130 an increase in SGFP2-tagged beta catenin levels on a per cell basis and supporting the notion that the gated events indeed represent
131 successfully tagged cells.
132 The following figure supplements are available for Figure 2:
133 **Figure supplement 1:** FACS Gating strategy for haploid HAP1 cells.
134 **Figure supplement 2 :** *SGFP2-CTNNB1* locus.

135

136
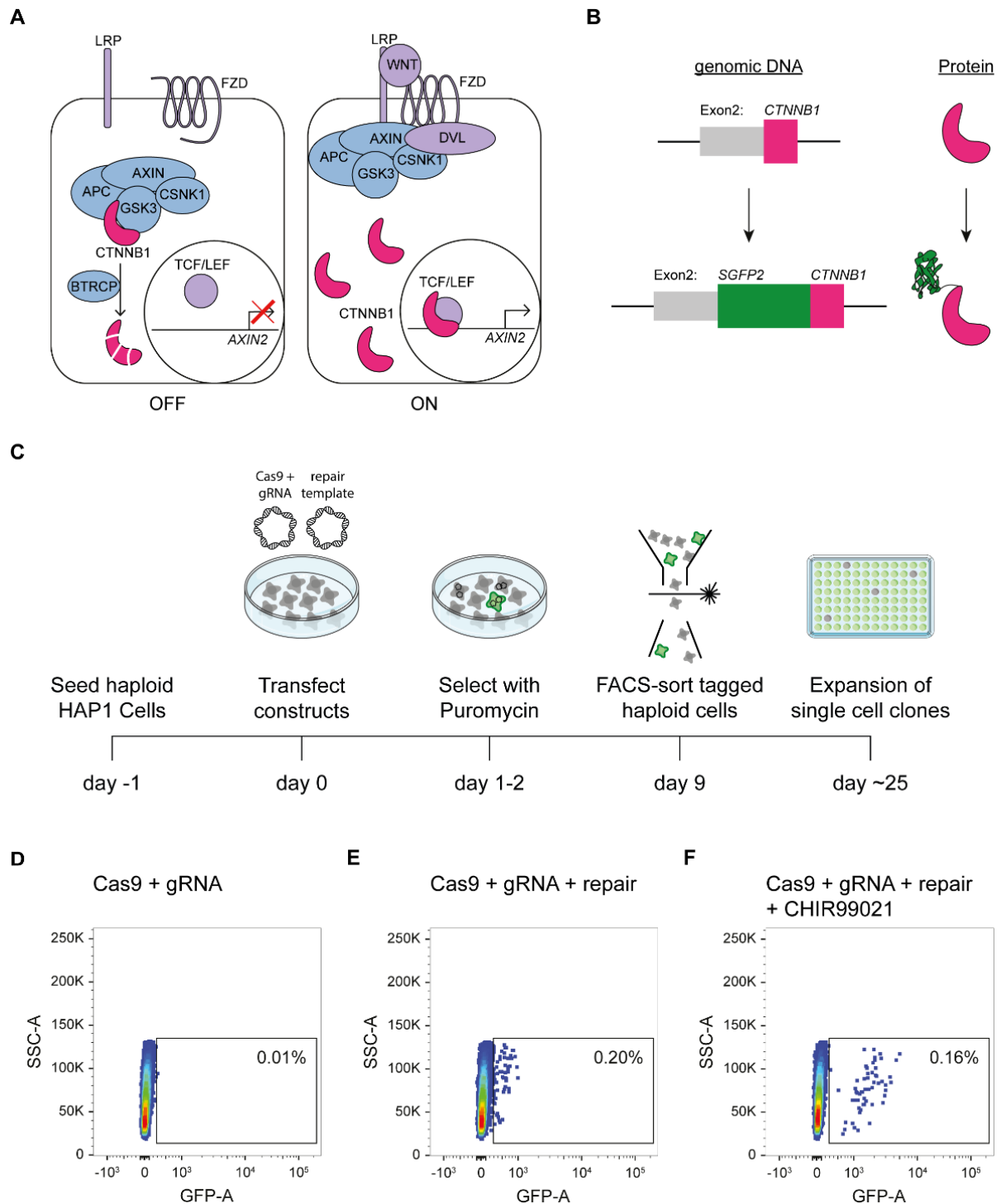
To verify that the SGFP2 tag did not interfere with CTNNB1 function, three clonal HAP1$^{SGFP2-CTNNB1}$ cell lines were further characterized using established experimental readouts for WNT/CTNNB1 signaling (Figure 2 and Figure 2 supplement 1). Western blot analysis confirmed that the HAP1$^{SGFP2-CTNNB1}$ clones did not contain any untagged CTNNB1 but only expressed the SGFP2-CTNNB1 fusion protein (Figure 2A). Moreover, the total levels of SGFP2-

7

142 CTNNB1 in tagged cell lines increased to the same extent as wild-type CTNNB1 in untagged

143 cells in response to CHIR99021 treatment (Figure 2A-B). Similarly, untagged and tagged

144 CTNNB1 induced target gene expression in equal measure, as measured by a TCF/LEF

145 responsive luciferase reporter (Hu et al., 2007) (Figure 2C), and increased transcription of the

146 universal WNT/CTNNB1 target *AXIN2* (Lustig et al., 2002) (Figure 2D). Finally, while

147 unstimulated cells mainly showed SGFP2-CTNNB1 localization at the adherens junction,

148 treatment with purified WNT3A protein (Figure 2E) and CHIR99021 (Figure 2 supplement 1E)

149 increased SGFP2-CTNNB1 levels in the cytoplasm and nucleus consistent with its signaling

150 function.

151 Taken together, WNT-responsive changes in CTNNB1 levels, localization and activity are

152 preserved after CRISPR/Cas9 mediated homozygous tagging of CTNNB1. Although there is

153 some variation between the three clones with respect to CTNNB1 stabilization and target

154 gene activation, this is likely due to the sub-cloning of these cell lines rather than the targeting

155 per se.

156 **Figure2:** Functional validation of three independent HAP1$^{SGFP2\text{-}CTNNB1}$ clones. A) Western blot, showing CTNNB1 (HAP1^{WT}) and SGFP2-CTNNB1
157 (HAP1$^{SGFP2\text{-}CTNNB1}$ clone 1, 2 and 3) accumulation in response to CHIR99021 treatment. All panels are from one blot that was cut at the 70 kDa
158 mark and was stained with secondary antibodies with different fluorophores for detection. Top: HAP1^{WT} cells express CTNNB1 at the
159 expected wild-type size. Each of the three clonal HAP1$^{SGFP2\text{-}CTNNB1}$ cell lines only express the larger, SGFP2-tagged form of CTNNB1, that runs
160 at the expected height (~27 kDa above the wild-type CTNNB1). Middle: Only the tagged clones express the SGFP2-CTNNB1 fusion protein,
161 as detected with an anti-GFP antibody at the same height. Bottom: alpha-Tubulin (TUBA) loading control. A representative image of n=3
162 independent experiments is shown. B) Quantification of Western blots from n=3 independent experiments, including the one in (A),
163 confirming that the accumulation of CTNNB1 in response to WNT/CTNNB1 pathway activation is comparable between HAP1^{WT} and HAP1$^{SGFP2\text{-}}$
164 ^{CTNNB1} cells. Horizontal bar indicates the mean. C) Graph depicting the results from a MegaTopflash dual luciferase reporter assay, showing
165 comparable levels of TCF/LEF reporter gene activation for HAP1^{WT} and HAP1$^{SGFP2\text{-}CTNNB1}$ cells in response to CHIR99021 treatment. Data points
166 from n=3 independent experiments are shown. Horizontal bar indicates the mean. Values are depicted relative to the DMSO control, which
167 was set to 1 for each individual cell line. D) Graph depicting *AXIN2* mRNA induction in response to CHIR99021 treatment, demonstrating
168 that induced expression of an endogenous target gene is comparable between HAP1^{WT} and HAP1$^{SGFP2\text{-}CTNNB1}$ cells. Data points represent n=3
169 independent experiments. Horizontal bar represents the mean. *HPRT* was used as a reference gene. Values are depicted relative to the
170 HAP1^{WT} DMSO control, which was set to 1. E) Representative confocal microscopy images of the three HAP1$^{SGFP2\text{-}CTNNB1}$ clones after 4-hour
171 vehicle control or 100ng/ml WNT3A treatment from n=1 biological experiment, revealing intracellular accumulation of SGFP2-CTNNB1
172 (green). Nuclei were counterstained with SiR-DNA dye (magenta). Scale bar is 10μm.
173 The following figure supplements are available for Figure 2:
174 **Figure supplement 1:** Verification of the WNT/CTNNB1 responsiveness of HAP1 cells.

8
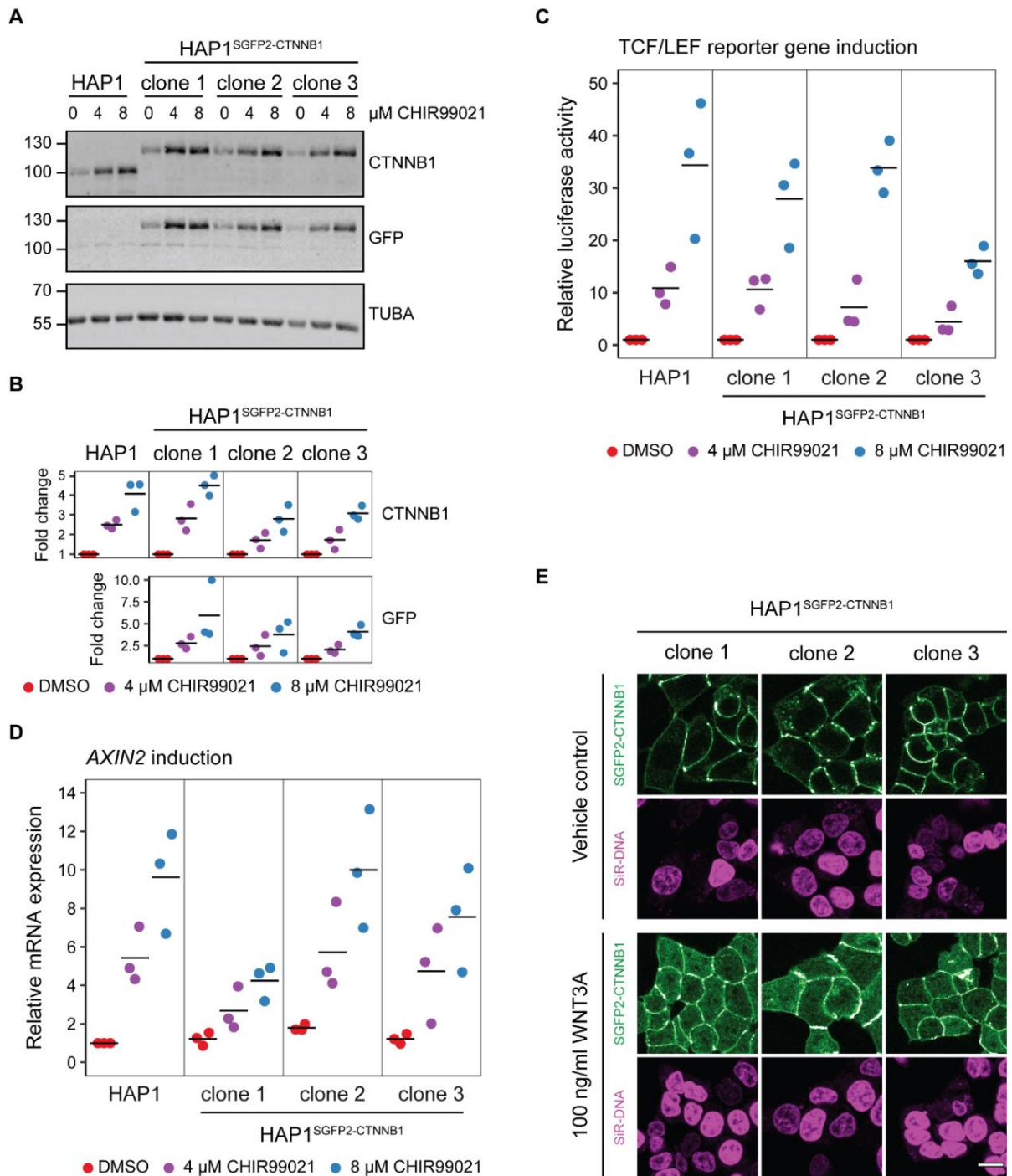
Live imaging of endogenous SGFP2-CTNNB1 during WNT pathway activation

To better understand the temporal dynamics of endogenous CTNNB1 stabilization, we performed live-cell imaging over 12 hours in HAP1[SGFP2-CTNNB1] cells (Figure 3, Supplementary Movie 1-2) with different levels of WNT stimulation. Unstimulated cells showed a stable CTNNB1 signal at the cell membrane throughout the imaging time course (Figure 3A,

9

181   Supplementary Movie 1). The membrane localization of CTNNB1 is consistent with its

182   structural role in adherens junctions (Valenta et al., 2012; Yap et al., 1997), which we will not

183   consider further in the current study. Stimulation with different concentrations of purified

184   WNT3A resulted in a heterogeneous response pattern, with some cells in the population

185   showing a far more prominent increase in CTNNB1 levels in the cytoplasm and nucleus than

186   others (Figure 3A, Figure 3 supplement 2A-B, Supplementary Movie 2).

187   To quantify these dynamic changes, we developed a custom-built automated segmentation

188   pipeline in CellProfiler™ (Figure 3D). Quantification showed that the dynamics of CTNNB1

189   accumulation were independent of the dose of WNT3A (Figure 3B-C, Supplementary Movies

190   4-5). Treatment with 100 ng/ml WNT3A increased SGFP2-CTNNB1 fluorescence 1.74-fold

191   (mean, 95% CI 1.73-1.76) in the cytoplasm and 3.00-fold (mean, 95% CI 2.97-3.03) in the

192   nucleus, with similar results in the other two HAP1$^{SGFP2-CTNNB1}$ clones (Figure 3 supplement 1).

193   Our quantification further shows that nuclear accumulation of CTNNB1 is favored over

194   cytoplasmic increase (compare the fold-changes in Figure 3B-C). Moreover, the first

195   statistically significant increases in fluorescence intensity in the cytoplasm could be detected

196   after ~45 minutes of treatment (Supplementary Movie 4, Figure 3 supplement 2C), whereas

197   in the nucleus an increase was first statistically significant after ~30 minutes (Supplementary

198   Movie 5, Figure 3 supplement 2D). To examine the relation between the cytoplasmic and

199   nuclear CTNNB1 pools more closely, we calculated the ratio between nuclear and cytoplasmic

200   intensities of SGFP2-CTNNB1 (Figure 3D, Supplementary Movie 6). In untreated cells, the

201   nuclear/cytoplasmic ratio was 0.652 (mean [3-5 hours], 95% CI 0.649-0.657), showing that

202   SGFP2-CTNNB1 was preferentially localized to the cytoplasm (Figure 3D, Figure 3 supplement

203   3). For the first 3 hours after WNT3A, nuclear CTNNB1 levels rose considerably faster than

204   cytoplasmic CTNNB1 levels until the nuclear/cytoplasmic ratio showed a slight nuclear

205   enrichment of 1.08 (mean [3-5 hours] 95% CI 1.07-1.10) for 100 ng/ml WNT3A. This indicates

206   that not only the turn-over, but also the subcellular localization of CTNNB1 is actively

207   regulated both before and after WNT pathway activation.
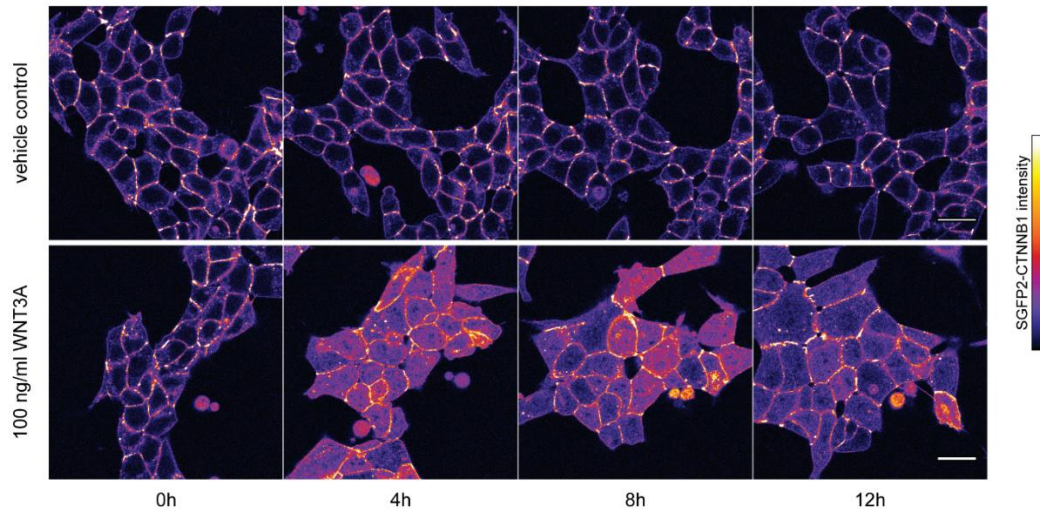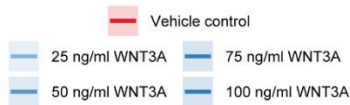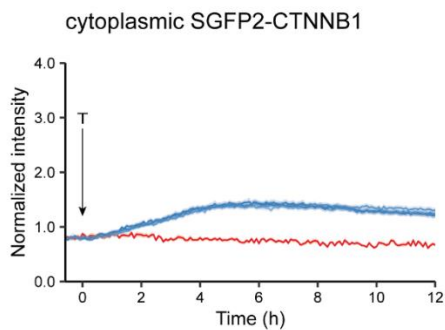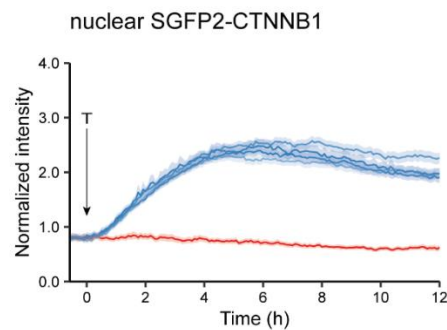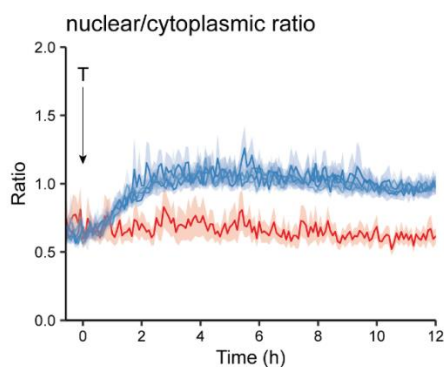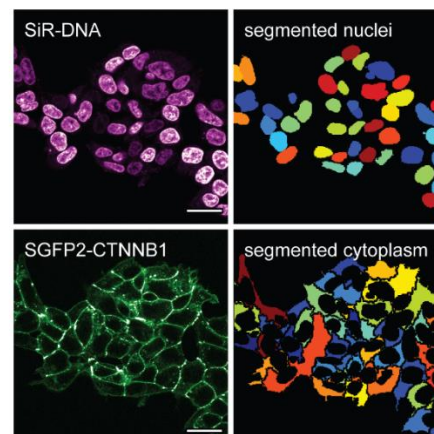

208

209 **Figure 3:** Live imaging of HAP1SGFP2-CTNNB1. A) Representative stills from confocal time-lapse experiments corresponding to
210 Supplementary Movies 1-2, showing an increase of SGFP2-CTNNB1 after treatment with 100 ng/ml WNT3A (bottom) relative to a vehicle
211 control (BSA) treated sample (top). Scale bar = 20 μm. B-D) Quantification of time-lapse microscopy series, using the segmentation pipeline
212 shown in (E). Arrow indicates the moment of starting the different treatments (T, see legend in B for details). B-C) Graph depicting the
213 normalized intensity of SGFP2-CTNNB1 in the cytoplasm (B) or nucleus (C) over time. Solid lines represent the mean normalized fluorescence
214 intensity and shading indicates the 95% confidence interval. n=155-393 cells for each condition and time point, pooled data from n=3
215 independent biological experiments. D) Graph depicting the nuclear/cytoplasmic ratio of SGFP2-CTNNB1 over time, calculated from raw
216 intensity values underlying (B) and (C). E) Segmentation of nuclei (top) and cytoplasm (bottom) based in the SiR-DNA signal and SGFP2-
217 CTNNB1 signal. Scale bar = 20μm.

218 The following figure supplements are available for Figure 3:
219 **Figure supplement 1:** Verification of imaging results with WNT3A three independent HAP1[SGFP2-CTNNB1] clones.
220 **Figure supplement 2:** Difference analysis of SGFP2-CTNNB1 fluorescence.
221 **Figure supplement3:** Unnormalized nuclear and cytoplasmic intensity measurements

Establishing a fitting model for SGFP2-CTNNB1 diffusion

223 Having measured the relative changes in the cytoplasmic and nuclear levels of CTNNB1 in

224 response to WNT3A stimulation, we next sought to exploit our experimental system to

225 quantify additional molecular properties of CTNNB1 in each of these subcellular

226 compartments using Fluorescence Correlation Spectroscopy (FCS). FCS is a powerful method

227 to measure the mobility and absolute levels of fluorescent particles in a nanomolar range,

228 compatible with typical levels of signaling proteins in a cell (reviewed in Hink, 2014). It has for

229 instance been used to gain insight into the assembly of DVL3 supramolecular complexes

230 (Yokoyama et al., 2012), the endogenous concentrations and mobility of nuclear complexes

231 (Holzmann et al., 2019; Lam et al., 2012), and most recently, to quantify ligand-receptor

232 binding reactions in the WNT pathway (Eckert et al., 2020). In point FCS, the fluorescence

233 intensity is measured in a single point (Figure 4A,D-E). Diffusion of labeled particles, in this

234 case SGFP2-CTNNB1, causes fluctuation of the fluorescence signal over time (Figure 4B). By

235 correlating the fluorescence intensity signal to itself over increasing time-intervals, an

236 autocorrelation curve is generated (Figure 4C). To extract relevant biophysical parameters,

237 such as mobility (a measure for size) and the absolute numbers of the fluorescent particles

238 (corresponding to their concentration), this autocorrelation curve is fitted with an

239 appropriate model.
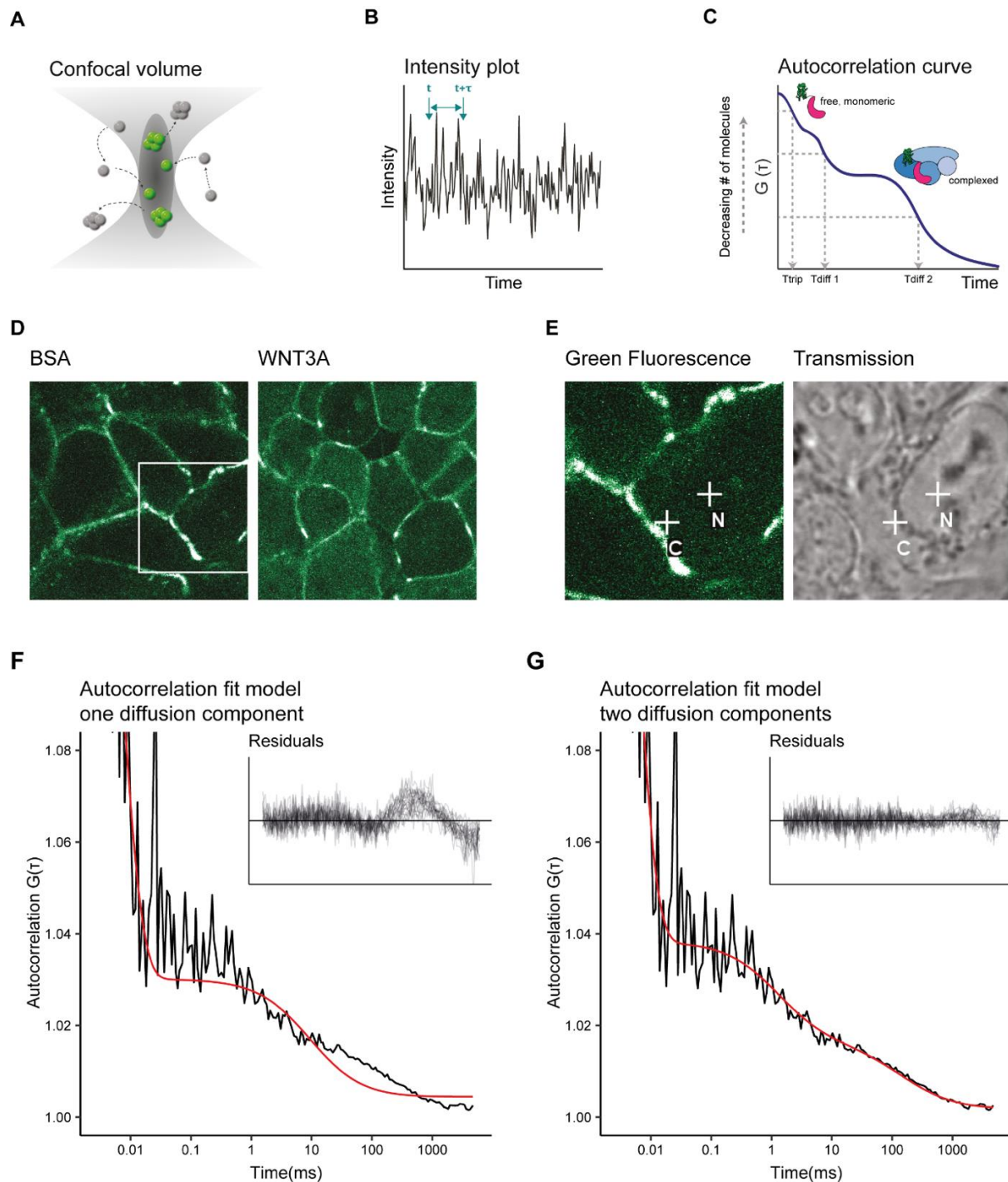
Figure 4: Two diffusion-component fit-model for SGFP2-CTNNB1 FCS measurements. A) Schematic representation of the point FCS technique, depicting the confocal volume with fluorescent particles diffusing in and out. Particles in FCS are defined by their coherent movement; therefore, a particle can be made up of monomers or multimers in isolation or complexed to unlabeled molecules. B) Schematic representation of intensity fluctuations over time as measured in the confocal volume. Fluctuations are the result of both photo-physics (e.g. blinking of the fluorophore) and diffusion. C) Graphical representation of the two diffusion-component fitting model used for our autocorrelation curves. T_{trip} describes the blinking of the SGFP2 fluorophore and the after-pulsing artefact. T_{diff1} and T_{diff2} describe the monomeric and complexed form of SGFP2-CTNNB1, respectively. Details of all fitting parameters are described in Materials and Methods. D) Representative confocal images of HAP1SGFP2-CTNNB1 cells treated for 4 hours with BSA (left) or 100 ng/ml WNT3A (right). E) Zoom in of the white rectangle in (D), with representative locations of FCS measurement points for cytoplasm (C) and nucleus (N) indicated with white crosses in the SGFP2-CTNNB1 channel and transmission channel. F-G) Fitting of a representative autocorrelation curve with one unfixed diffusion-component (F) or a two diffusion-component model (G), where the first diffusion component was fixed to the speed of free monomeric SGFP2-CTNNB1 (14.9μm²/s) and the second diffusion component was unfixed. The black line represents the autocorrelation curve generated from the FCS measurement, the red line represents the fitted model. The residuals after fitting of 25 individual curves are shown in the upper right corner of the graphs.

13

255   We first attempted to fit the autocorrelation curves obtained with point FCS measurements

256   of HAP1$^{SGFP2-CTNNB1}$ cells with a one-component model (i.e. containing one single diffusion

257   speed for SGFP2-CTNNB1). This model was unable to fit most of our data (Figure 4F). The

258   current literature suggests that while a large portion of CTNNB1 is present as a monomer

259   (Gottardi and Gumbiner, 2004; Maher et al., 2010), CTNNB1 is also present in multiprotein

260   complexes in the cytoplasm and in the nucleus (reviewed in Gammons and Bienz, 2018).

261   Therefore, we next used a model with two diffusion components, in which the first diffusion

262   component was fixed to the diffusion speed of monomeric, unbound SGFP2-CTNNB1 (14.9

263   μm^2/s) and the second diffusion component was limited to slower speeds compatible with

264   point-FCS imaging (see materials and methods for details). This model provided good fits for

265   our autocorrelation curves obtained in both cytoplasmic and nuclear point FCS measurements

266   (Figure 4G), consistent with the presence of free monomeric CTNNB1 and larger CTNNB1

267   containing complexes in both the nucleus and cytoplasm.

268   <u>Quantification of absolute SGFP2-CTNNB1 concentrations</u>

269   Using this fitting model, we determined, for the first time, the absolute concentrations of

270   endogenous CTNNB1 in living cells in presence and absence of a physiological WNT stimulus

271   (Figure 5A). In the absence of WNT3A, we determined the total concentration of SGFP2-

272   CTNNB1 to be 180 nM (median, 95%CI 127-218) in the cytoplasm and 122 nM (median, 95%CI

273   91-158) in the nucleus. This is consistent with the nuclear exclusion we observed with

274   confocal imaging (Figure 3).

275   In the presence of WNT3A, we measured a 1.2-fold increase in the total SGFP2-CTNNB1

276   concentration to 221 nM (median, 95%CI 144-250 nM) in the cytoplasm. This increase was

277   smaller than expected from fluorescence intensity measurements (Figure 3B), for which we

14

278 currently have no explanation (Figure 5 supplement 1). In the nucleus the concentration

279 increased 2.0-fold to 240 nM (median, 95%CI 217-325) upon pathway activation. Nuclear

280 concentrations of SGFP2-CTNNB1 therefore exceed cytoplasmic concentrations after WNT3A

281 treatment, consistent with the nuclear accumulation observed with live imaging (Figure 3).

282 These concentrations are in a similar range as those previously determined by quantitative

283 mass spectrometry in different mammalian cell lines (Kitazawa et al., 2017; Tan et al., 2012).

284 Of note, the exact concentrations can vary between cell types and may be dependent on the

285 intricacies and assumptions that underlie each individual technique.

286 **Table 1:** Total number of SGFP2-CTNNB1 molecules and calculated concentrations obtained from FCS measurements in n=3 independent
287 experiments. The concentration is calculated from the number of molecules and the calibrated confocal volume (see material and methods).
288 The number of molecules is consistent with those measured with N&B analysis (Figure 5 supplement 1A, Supplementary file 1)

compartment	treatment	n	Number of molecules		Concentration (nM)	
			median	95% CI	median	95% CI
Cytoplasm	BSA	21	80	70-116	180	127-218
	WNT3A	21	95	85-122	221	144-250
Nucleus	BSA	21	63	53-72	122	91-158
	WNT3A	18	135	127-150	240	217-325

289

290 Our two-component fitting model also allowed us to discriminate between pools of SGFP2-

291 CTNNB1 with different mobility, i.e. fast diffusing monomeric CTNNB1 (Figure 5B) and slow

292 diffusing complexed CTNNB1 (Figure 5C). In the nucleus, the concentration of fast moving

293 CTNNB1 increased 2.0-fold from 87 nM (median, 95%CI 78-119) to 170 nM (median, 95%CI

294 147-214), while slow moving CTNNB1 concentration increased 3.9-fold from 22 nM (median,

295 95%CI 4-40) to 86 nM (median, 95%CI 67-114). This is also reflected by the increase in the

296 bound fraction of SGFP2-CTNNB1 the nucleus (Figure 5D). The preferential increase of the

297 slow-moving fraction is consistent with the notion that upon WNT stimulation CTNNB1 will

298 become associated with the chromatin in a TCF dependent transcriptional complex (or "WNT

299 enhanceosome").

15

Table 2: Number and concentration of SGFP2-CTNNB1 molecules with the fast or slow diffusion coefficient obtained from FCS measurements in n=3 independent experiments. The concentration is calculated from the number of molecules and the calibrated confocal volume (see material and methods).

| | | | Fast SGFP2-CTNNB1 | | | | Slow SGFP2-CTNNB1 | | | |
| | | | Number of molecules | | Concentration (nM) | | Number of molecules | | Concentration (nM) | |
compartment	treatment	n	median	95% CI	median	95% CI	median	95% CI	median	95% CI
Cytoplasm	BSA	21	51	40-63	91	66-139	29	20-37	57	38-76
	WNT3A	21	60	47-80	145	76-168	35	30-41	68.	57-76
Nucleus	BSA	21	48	41-66	87	78-119	13	2-22	22	4-40
	WNT3A	18	96	81-101	170	147-214	47	37-49	86	64-104

Of note, in the cytoplasm, the concentration of both fast and slow SGFP2-CTNNB1 increased

upon WNT3A treatment (Figure 5B-C), with the fraction of bound SGFP2-CTNNB1 remaining

equal between stimulated (median 0.38, 95%CI 0.29-0.46) and unstimulated cells (median

0.34, 95%CI 0.31-0.4) (Figure 5D). The fact that a large portion of CTNNB1 remains in a

complex after WNT stimulation, challenges the view that mainly monomeric CTNNB1

accumulates, as commonly depicted in the textbook model (Figure 1A).

Figure 5: Abundance and mobility of SGFP2-CTNNB1 molecules in living cells after 4 hours WNT3A treatment or control. Details on sample size and statistics can be found in supplementary file 1. A) Graph depicting the total concentration of SGFP2-CTNNB1 particles (monomeric plus complexed) as measured with FCS. B) Graph depicting the concentration of SGFP2-CTNNB1 particles with the fast diffusion component (i.e. free monomeric). C) Graph depicting the concentration of SGFP2-CTNNB1 containing particles with the slow diffusion component (i.e. complex associated).D-E) Graphs depicting the fraction (D) and speed (E) of the second diffusion component (i.e. SGFP2-CTNNB1 containing complex) measured by FCS. F) Example of typical regions of interest in two cells used in N&B analysis. Solid line represents the analysis ROI, dashed line, marks the outline of the nuclear envelope. G) Schematic representation of a confocal volume with different brightness species. On the left are 6 monomers with a brightness of 1, on the right 2 trimers with a brightness of 3, both result in a fluorescence of 6. N&B analysis is able to extract the number and the brightness of such samples, for more detail see supplement 1 of this figure. H) Graph depicting the molecular brightness of SGFP2-CTNNB1 in the cytoplasm and nucleus relative to controls as measured with N&B in the same subcellular compartments. EGFP monomer was used for normalization and EGFP dimer as a control for N&B measurements.
The following supplements are available for Figure 6:
Figure supplement 1: Quantification of SGFP2-CTNNB1 particles, fluorescence and fluorescence lifetime.
Figure supplement 2: Number and Brightness analysis
Supplementary File 1: Lists all summary statistics (mean, median, 95% confidence intervals, differences, p-values) of the FCS and N&B parameters show in Figure 6 and Figure 6 supplement 1.

326
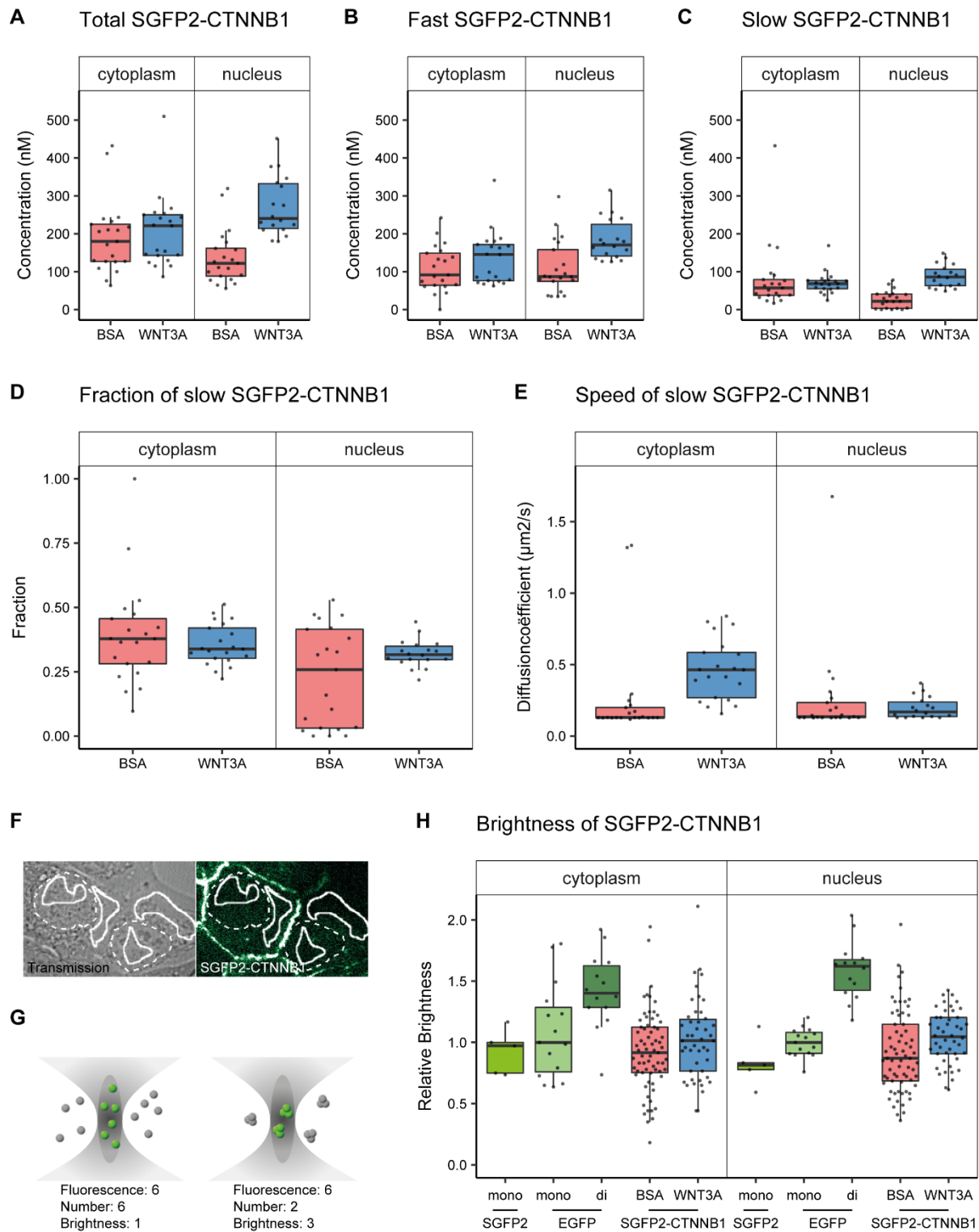
327   Quantification of SGFP2-CTNNB1 mobility

328   While we cannot determine the exact composition of the SGFP2-CTNNB1 complex, we do

329   obtain biophysical parameters that are linked to its size. For instance, the diffusion coefficient

330   of the nuclear SGFP2-CTNNB1 complex was 0.17 $\mu m^2 s^{-1}$, (median, 95%CI 0.14-0.22) in cells

331   treated with purified WNT3A (Figure 5E). This is comparable to the diffusion coefficients

332   measured for other chromatin bound transcriptional activators (Lam et al., 2012), which

333   further supports that this pool represents the WNT enhanceosome.

334   In the cytoplasm, we determined the second diffusion coefficient of SGFP2-CTNNB1 to be

335   0.13 $\mu m^2 s^{-1}$ (median, 95% CI 0.13-0.17) in the absence of WNT3A stimulation (Figure 5E). This

336   is indicative of very large complexes containing SGFP2-CTNNB1 that move with diffusion

337   kinetics comparable to those previously observed for the 26S proteasome (Pack et al., 2014).

338   After WNT3A treatment, the speed of the cytoplasmic complex increased 3.5-fold to 0.46

339    $\mu m^2 s^{-1}$ (95% CI of the median 0.37-0.57). Because a 3.5-fold change in speed would result in

340   3.5^3-change in size for a spherical particle (assuming Einstein-Stokes, see equation 7 in the

341   material and methods section for details), this indicates that the size of the cytoplasmic

342   CTNNB1 complex drastically changes when the WNT pathway is activated. Thus, although the

343   fraction of CTNNB1 that resides in a complex remains the same, the identity of the

344   cytoplasmic complex is quite different in unstimulated and WNT3A stimulated cells.

345   Determining the multimerization status of SGFP2-CTNNB1

346   Recent work suggests that the CTNNB1 destruction complex (also known as the

347   "degradosome") is a large and multivalent complex, mainly as the result of AXIN and APC

348   multimerization (reviewed in Schaefer and Peifer, 2019). The second diffusion coefficient,

349   determined by our FCS measurements (Figure 5E), is consistent with this model. Such a large,

350   multivalent destruction complex would be expected to have multiple CTNNB1 binding sites.

351   To measure the multimerization status (i.e. the number of bound SGFP2-CTNNB1 molecules)

352   within this cytoplasmic complex, we performed Number and Brightness (N&B) analysis

353   (Figure 5F-G, Figure 5 supplement 2). N&B is a fluorescence fluctuation spectroscopy

354   technique similar to point FCS, but it makes use of image stacks acquired over time rather

355   than individual point measurements (Digman et al., 2008). By quantifying the variance in

356   fluorescence intensity of this stack, not only the number of particles but also their brightness

357   can be determined. The number of particles we determined using N&B, were highly similar to

358   those obtained with FCS (compare Figure 5 supplement 1A with Table 1).

359   Because brightness is an inherent property of a fluorophore, a change in brightness is a

360   measure of the number of fluorophores per particle. In our case, the brightness is indicative

361   of the number of SGFP2-CTNNB1 molecules per complex. As N&B does not incorporate

362   diffusion kinetics, we cannot differentiate between monomeric (which would have a

363   brightness of one) and complexed CTNNB1 (which would have a brightness exceeding one if

364   multiple CTNNB1 molecules reside in a single complex). Therefore, the measured brightness

365   of SGFP2-CTNNB1 in our N&B analysis is an average of both fractions. We observe that the

366   total pool of SGFP2-CTNNB1 in both the cytoplasm and nucleus has a brightness similar to

367   EGFP and SGFP2 monomers (Figure 5H, Table 3). Because we found a large fraction of SGFP2-

368   CTNNB1 to reside in a complex using point FCS (Figure 5C-D), this suggests that few, if any, of

369   these complexes contain multiple SGFP2-CTNNB1 molecules. If the cytoplasmic SGFP2-

370   CTNNB1 containing complex indeed represents a large, multivalent destruction complex, this

371   would imply that under physiological conditions, quite unexpectedly, most CTNNB1 binding

372   sites are unoccupied in both the absence and presence of WNT3A.

373   **Table 3:** Brightness of SGFP2-compared relative to EGFP-monomer and -dimer controls in n=2 independent experiments. P-values were
374   calculated using PlotsOfDifferences that uses a randomization test (Goedhart, 2019).Note that only the EGFP-dimer is significantly different
375   to the EGFP-monomer control, while SGFP2-CTNNB1 is not.

Fluorophore	Compartment	Treatment	n	median	95CI median	P-value to matched control (EGFP monomer in the nucleus or cytoplasm)
EGFP-monomer	Cytoplasm	NA	15	1	0.79 - 1.34	1.000
EGFP-dimer	Cytoplasm	NA	14	1.4	1.29 - 1.60	0.011*
SGFP2-CTNNB1	Cytoplasm	BSA	69	0.92	0.83 – 1.00	0.738
SGFP2-CTNNB1	Cytoplasm	100ng/ml WNT3A	46	1.01	0.93 - 1.11	0.919
EGFP-monomer	Nucleus	NA	15	1	0.91 - 1.07	1.000
EGFP-dimer	Nucleus	NA	14	1.62	1.44 - 1.69	<0.001*
SGFP2-CTNNB1	Nucleus	BSA	69	0.87	0.78 - 0.96	0.192
SGFP2-CTNNB1	Nucleus	100ng/ml WNT3A	46	1.05	0.95 - 1.15	0.578

376

377   ## A minimal computational model of WNT/CTNNB1 signaling

378   Quantitative measurements and physical parameters of WNT pathway components and their

379   interactions remain limited (Kitazawa et al., 2017; Lee et al., 2003; Tan et al., 2012), especially

380   in living cells. As we obtained measurements of different functional pools of CTNNB1, we next

381   sought to integrate these biophysical parameters in a minimal computational model of WNT

382   signaling to identify the critical nodes of regulation of subcellular SGFP2-CTNNB1 distribution

383   (Figure 6A, Table 4-5, Materials and Methods). This minimal model is based on a previous

384   model of Kirschner and colleagues (Lee et al., 2003), and incorporates the new data obtained

385   in our study, supplemented with parameters from the literature (Lee et al., 2003; Tan et al.,

386   2012).

387   Our model diverges from the model presented by Lee et al. on two major points. First, the

388   model is simplified by replacing the details of the destruction complex formation cycle and

389   the individual actions of APC and AXIN with a single, fully formed destruction complex. We

390   chose this option because our study does not provide new quantitative data on the formation

391   and dynamics of the destruction complex, but does provide absolute concentrations of

392   CTNNB1 that is in a bound state in the cytoplasm. Second, we explicitly include shuttling of

393   CTNNB1 between the cytoplasm and nucleus in both directions (Schmitz et al., 2013; Tan et

394   al., 2014).

395   Thus, our model (Figure 6A) describes the binding of cytoplasmic CTNNB1 ('CB') to the

396   destruction complex ('DC') leading to its phosphorylation and degradation (described by k3),

397   which releases the DC. Transport of CTNNB1 from the cytoplasm to the nucleus, allows

398   nuclear CTNNB1 ('NB') to bind to TCF forming a transcriptional complex (NB-TCF). When WNT

399   is present in the system, we describe the inactivation of the destruction complex ('DC*') by

400   DVL.   The   model   is   available   as   interactive   app   at

401   https://wntlab.shinyapps.io/WNT_minimal_model/ and allows users to explore the effects of

402   modulating different equilibria and constants in an intuitive way.

403   Our model faithfully recapitulates the dynamic changes that we observe with functional

404   imaging (compare Figure 6B-F to Figure 3 and 5). Moreover, it reveals two critical regulatory

405   nodes in addition to the requisite inactivation of the destruction complex (described by

406   k5/k4). The first additional node of regulation is nuclear import and export (or 'shuttling',

407   described by k6/k7). Upon WNT stimulation, the ratio of k6/k7 needs to increase in order for

408   the model to match the free CTNNB1 concentrations we measured by FCS (Table 5, Figure

409   5B). Thus, the balance shifts from nuclear export before WNT, to nuclear import after WNT.

410   The second additional node of regulation is the association of CTNNB1 with the TCF

411   transcriptional complex (or 'retention'), described by k9/k8. Upon WNT stimulation, the ratio

412 of k9/k8 needs to decrease by almost a factor of 10 in order for the model to reproduce the

413 concentrations of free and bound CTNNB1 in the nucleus as measured by FCS (Table 5, Figure

414 6F, Figure 5B-C). Thus, association of CTNNB1 to the TCF transcriptional complex is favored

415 after WNT stimulation.

416 In summary, our model suggests that WNT/CTNNB1 signaling is regulated at three distinct

417 levels of the signal transduction pathway: destruction complex inactivation,

418 nucleocytoplasmic shuttling and nuclear retention.

419 **Table 4**: Variables Minimal Model of WNT signaling.

Model name	Variable	Compound	Values obtained from	WNT OFF (nM)	WNT ON (nM)
CB	x_1	Free cytoplasmic CTNNB1	FCS data this report	91	145
DC	x_2	Free destruction complex	Model equations	82.4	52
CB*-DC	x_3	DC-bound phosphorylated CTNNB1	FCS data this report*	62.5*	62.5*
DC*	x_4	Inactivated destruction complex	Model equations	0	30.5
NB	x_5	Free nuclear CTNNB1	FCS data this report	87	170
TCF	x_6	Free TCF	Model equations	81	17
NB-TCF	x_7	TCF-bound nuclear CTNNB1	FCS data this report	22.2	86
TCF^0	TCF^0	Total TCF	x_7 and Tan et al., 2012 - Figure 11	103	103

420
421 *Under the assumption that k3 does not change, the levels of CB*-DC remain equal. Since there was no significant difference between the concentration of slow SGFP2-CTNNB1 (Table 2) the average of both medians was used

422
423 **Table 5**: Equilibrium conditions for the Minimal Model of WNT signaling. All rates are multiplied with factor R=20, so that the equilibrium is reached at 4.5h according to Figure 4 C, D.

Rate constant		Biological process	Values based on	WNT OFF	WNT ON
b	nMmin^{-1}	CTNNB1 synthesis	v_{12} from Lee	0.423	0.423
$\frac{k_2}{k_1}$	nM	Binding to and phosphorylation by the destruction complex of cytoplasmic CTNNB1	K_8 from Lee	120	120
k_3	min^{-1}	Dissociation and degradation of phosphorylated CTNNB1 from the destruction complex	Deduced from b and x_3	0.0068	0.0068
$\frac{k_5}{k_4}$	nM	Inactivation of the destruction complex by activated DVL	Fitted to x_1 and x_7	N.A.	1.7
$\frac{k_6}{k_7}$		Ratio between nuclear import and export of CTNNB1	Deduced from x_1 and x_5	0.96	1.17
$\frac{k_9}{k_8}$	nM	Dissociation of nuclear CTNNB1 from TCF	Deduced from x_5, TCF^0, x_7	320	33.6
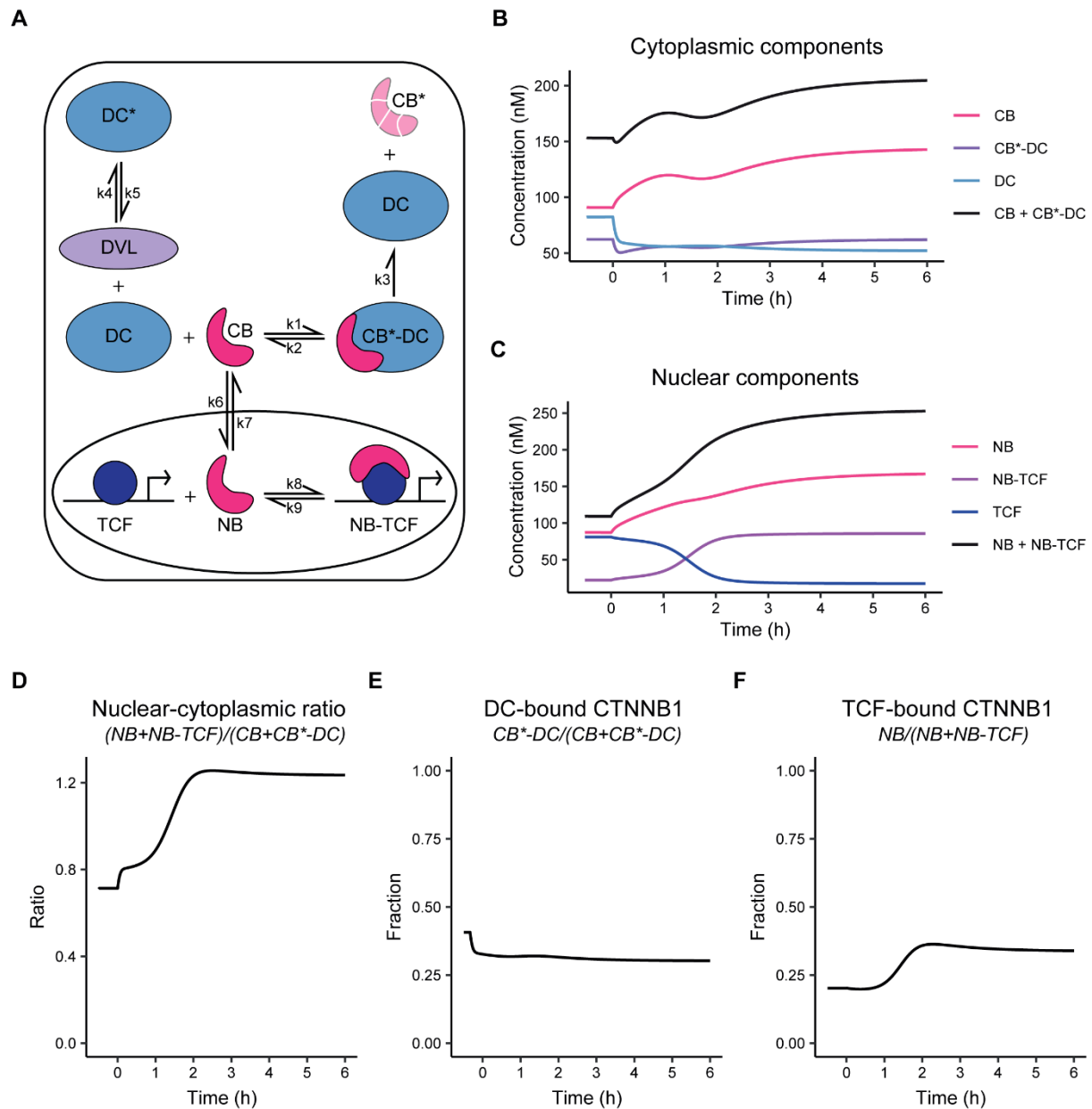
Figure 6: Computational model of WNT/CTNNB1 based on FCS concentrations for free and complexed CTNNB1 (Table 1-2). A) Schematic overview of the model. DC=destruction complex, DC*= DVL-inactivated DC, CB=cytoplasmic CTNNB1, CB*=phosphorylated CB, NB=nuclear CTNNB1, TCF=TCF/LEF transcription factors, DVL=WNT-activated DVL. The model assumes that there is no activated DVL in the absence of WNT, therefore k5/k4 do not play any role in the WNT 'OFF' equilibrium. Note that CB* is degraded and therefore plays no role in the model. B) Graph depicting the modelled concentrations of cytoplasmic components over time. The black line indicates total concentration of cytoplasmic CTNNB1, corresponding to Figure 4C. C) Graph depicting the modelled concentrations of nuclear components over time. The black line indicates total concentration of nuclear CTNNB1, corresponding to Figure 4D. D) Graph depicting the ratio of total nuclear and cytoplasmic CTNNB1 over time, corresponding to the measurements in 4E. E) Graph depicting the DC-bound CTNNB1 fraction ratio over time. F) Graph depicting the TCF-bound CTNNB1 fraction ratio over time.

434   Perturbing the system to mimic oncogenic WNT signaling

435   WNT signaling is often disrupted in cancer (reviewed in Polakis, 2000; Zhan, Rindtorff, &

436   Boutros, 2017), in many cases due to inactivating mutations of negative regulators or

437   activating mutations in CTNNB1 itself (Bugter et al., 2020). One of the earliest identified

438   mutations in CTNNB1 was a substitution of serine-45 for a phenylalanine (S45F) (Morin et al.,

439   1997). This mutation removes the CSNK1 priming phosphorylation site on CTNNB1 that is

440   needed for sequential phosphorylation by GSK3, and thus blocks its proteasomal degradation

441   (Amit et al., 2002; Liu et al., 2002).

442   We generated the S45F mutation in one of our HAP1$^{SGFP2-CTNNB1}$ cell lines through a second

443   step of CRISPR/Cas9 mediated genome editing (Fig 7 supplement 1A-D). As expected, the

444   mutation resulted in higher CTNNB1 levels (Figure 7 supplement 1E-F) and constitutive

445   downstream activation of the pathway (Figure 7 supplement 1G-H). Next, we used this cell

446   line for two purposes. First, we used FCS and N&B to compare the complex-state of wild-type

447   and mutant CTNNB1 in the cytoplasm (Figure 7). Second, we reproduced the same

448   perturbation in silico to strengthen the link between our experimental data and the

449   computational model (Figure 8).

450   Similar to the situation detected under physiological conditions (Figure 5D), we find a large

451   fraction of SGFP2-CTNNB1^{S45F} to reside in a cytoplasmic complex (Figure 7A). As observed for

452   physiological stimulation with WNT3A (Figure 5E), the speed of this complex is increased in

453   SGFP2-CTNNB1^{S45F} compared to unstimulated HAP1$^{SGFP2-CTNNB1}$ cells (Figure 7B). We find

454   similar behavior when we block the GSK3 mediated phosphorylation of wild-type CTNNB1

455   using CHIR99021 (Figure 7C-D). The reduction in cytoplasmic complex size therefore must

456   occur downstream of CTNNB1 phosphorylation. Intriguingly, our N&B analyses suggest that

457 these smaller S45F mutant cytoplasmic complexes have a higher occupancy of CTNNB1

458 (Figure 7E) than the those in WNT3A (Figure 5H) or CHIR99021 (Figure 7F) stimulated wildtype

459 cells. The S45F mutant (median 1.304, 95% CI 1.139-1.418, p=0.002) was significantly brighter

460 than the SGFP2 monomer control (median 0.866, 95% CI 0.573 - 0.949), where the WT tagged

461 HAP1 cells again did not diverge from the monomer (0.886, 95% CI 0.722-1, p=0.845)

462 (Supplementary file 1).
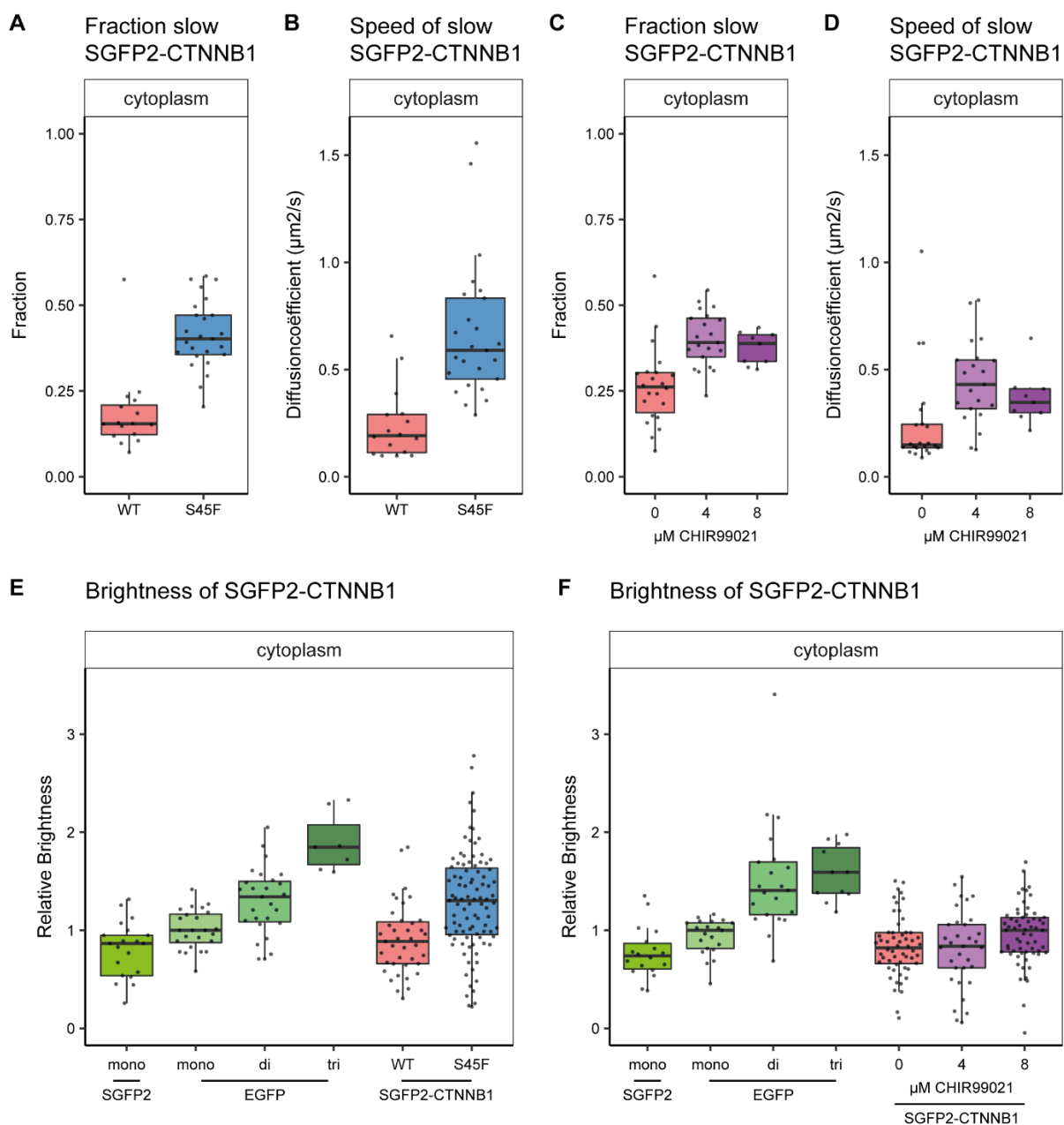
463

464 **Figure7** Cytoplasmic complex characteristics in absence of SGFP2-CTNNB1 N-terminal phosphorylation. The S45F mutant was introduced
465 using CRISPR (see Figure 7 supplement 1) and CHIR treated and control cells were measured after 24 hours. Details on sample size and
466 statistics can be found in supplementary file 1. A) Graph depicting the fraction of particles with the second diffusion component (i.e. SGFP2-
467 CTNNB1 containing complex) measured by FCS for S45F mutant B) Graph depicting the speed of the second diffusion component (i.e. SGFP2-
468 CTNNB1 containing complex) measured by FCS for S45F mutant. C).Graph depicting the fraction of particles with the second diffusion
469 component (i.e. SGFP2-CTNNB1 containing complex) measured by FCS after 24h treatment with CHIR99021 C) Graphs depicting the speed
470 of the second diffusion component (i.e. SGFP2-CTNNB1 containing complex) measured by FCS after 24h treatment with CHIR99021 .E-F)
471 Graphs depicting the molecular brightness of SGFP2-CTNNB1 in the cytoplasm and nucleus relative to controls as measured with N&B in the
472 same subcellular compartments for S45F mutant CTNNB1 (E) or after 24 hours of CHIR99021 treatment (F). EGFP monomer was used for
473 normalization and EGFP dimer and trimer as controls for N&B measurements.
474 The following supplements are available for Figure 7:
475 **Figure 7 supplement 1:** Generation and characterization of a S45F mutant cell line (HAP1$^{SGFP2-CTNNB1(S45F)}$)

476   The S45F mutant shows a substantial increase in SGFP2-CTNNB1 levels in the cytoplasm and

477 nucleus (Figure 8A). As this constitutive mutation does not provide any kinetic information,

478 we also measured the dynamic response of SGFP2-CTNNB1 to CHIR99021-mediated GSK3

479 inhibition (Figure 8 supplement 1, Supplementary movie 3). We see similar initial kinetics as

480 for WNT3A stimulation. However, in contrast to what is observed for WNT3A treatment, no

481 plateau was reached at the highest concentration of CHIR99021 (8 µM). The fact that

482 intracellular SGFP2-CTNNB1 levels in the 8 µM CHIR99021 condition continued to accumulate,

483 suggests that negative feedback, for example through AXIN2 (Lustig et al., 2002) or through

484 internalization of receptor complexes (Agajanian et al., 2019), is overridden under these

485 circumstances. Of note, the quantification also confirms that there is cell to cell heterogeneity

486 in the response, regardless of whether WNT/CTNNB1 signaling is activated at the level of the

487 receptor (WNT3A treatment) or at the level of the destruction complex (CHIR99021

488 treatment), as can be seen from the spread of intensities measured from individual cells

489 (Figure 3 Supplement 2A-B).

490   Finally, we compared our biological measurements from these perturbation experiments to

491 our computational model predictions. Both the S45F mutation and CHIR99021 treatment

492 disrupt one of the critical nodes in the model, namely the degradation of phosphorylated

493 CTNNB1 (corresponding to k3, Figure 6A). With FCS and N&B we quantified the accumulation

494 of CTNNB1 levels of mutant SGFP2-CTNNB1^{S45F} (Figure 8B, Figure 8 supplement 2A) and wild-

26

495   type SGFP2-CTNNB1 upon CHIR99021 treatment (Figure 8 supplement 2B-C). Both exceeded

496   the levels observed with physiological WNT3A stimulation (Figure 3A-C, Figure 5A). In our

497   computational model we simulated reduced degradation by lowering the value of k3. A

498   reduction in k3 from its initial value (k3=0.0068, Table 5) to k3=0.0043, accurately predicted

499   the higher cytoplasmic concentration measured for the S45F mutant (Figure 8C), but a further

500   reduction of k3=0.0038 was needed to match the measured nuclear concentration (Figure

501   8D). However, reducing k3 alone was not sufficient to reproduce either the fraction of

502   CTNNB1 that is bound in the nucleus (Figure 8E-G) or the overall nuclear enrichment of

503   CTNNB1 (Figure 8H). The latter requires a predicted nuclear/cytoplasmic (N/C) ratio greater

504   than one, as observed in both physiological and constitutively active WNT/CTNNB1 signaling

505   (Figure 8I-K).

506   The increase in the bound fraction of SGFP2-CTNNB1 in the nucleus was comparable between

507   our mutant cell line (Figure 8E), CHIR99021 (Figure 8F) and WNT3A (Figure 5D) treatment. To

508   match this experimental observation, we adjusted the k9/k8 ratio as was also required for

509   physiological WNT3A signaling (Table 5, Figure 8G). This shows the importance of this

510   regulatory node not only in physiological, but also in oncogenic signaling. At the same time,

511   the adjustment of k9/k8 on top of k3 still does not predict the observed nuclear enrichment

512   of CTNNB1 (Figure 8H). After changing the nuclear shuttling ratio k6/k7 to the ratio we fitted

513   for the WNT ON situation (Table 5), the model now also reproduces the nuclear enrichment

514   of CTNNB1 (Figure 8L). In figures 8M-N, we show that the changes in parameters k6/k7 and

515   k9/k8 have little effect on the CTNNB1 concentration in the cytoplasm, but do substantially

516   affect the nuclear concentrations of CTNNB1. This suggest that processes downstream of

517   CTNNB1 degradation play a significant and active role in the CTNNB1 dynamics of the cell.

27

518   Taken together, our computational model can describe both physiological and oncogenic

519   signaling. Moreover, it underlines the importance of CTNNB1 regulation downstream of

520   destruction complex activity and confirms a critical role for nuclear import and nuclear

521   retention.

522   **Figure 8**: In silico and experimental perturbation of WNT signaling. Details on experimental sample size and statistics can be found in
523   supplementary file 1. A) Representative confocal images of HAP1-SGFP2WT (WT, top) and HAP1-SGFP2S45F (S45F, bottom) cells acquired
524   with the same image settings. The S45F mutation leads to the accumulation and nuclear enrichment of CTNNB1 in the cell. B) Graph depicting
525   the total concentration of SGFP2-CTNNB1 particles (monomeric plus complexed) as measured with FCS. C-D) Inhibition of CTNNB1
526   degradation is modelled as a reduction in the value of k3. C) Graph depicting the predicted total cytoplasmic CTNNB1 concentration as a
527   function of k3. A reduction in k3 from 0.0068 (Table 5, WNT ON and WNT OFF conditions) to ~0.0043 (dotted line) corresponds to the
528   cytoplasmic concentration observed (solid line). D) Graph depicting the predicted total nuclear CTNNB1 concentration as a function of k3.
529   The solid horizontal line indicates the concentration measured for the S45F mutant by FCS. Note that the value of k3 that matches the
530   observed cytoplasm concentration (dotted line) does not match the experimentally determined concentration in the nucleus (solid line). E-
531   F) Graphs depicting the fraction of particles with the second diffusion component (i.e. SGFP2-CTNNB1 containing complex) measured by FCS
532   for wild-type and S45F mutant (E) and after 24-hour CHIR99021 treatment (F). The increase in the bound fraction in the oncogenic mutant
533   or after GSK3 inhibition we find, is comparable to what we observed in WNT3A stimulated cells (Figure 5D). G) Graph showing the predicted
534   nuclear bound fraction of CTNNB1as a function of k3 with the TCF/CTNNB1 binding affinity of the model (Table 4) for WNT OFF (k9/k8 =320,
535   pink line) and for WNT ON (k9/k8=33.5, blue line). Note that for WNT ON, the value for the nuclear bound fraction approximates the
536   experimentally determined slow fraction for the S45F mutant (solid line, panel E) at the value for k3 that matches the cytoplasmic
537   concentration of CTNNB1 (dotted line). H) Graph showing the predicted nuclear/cytoplasmic (N/C)-ratio as a function of k3 with TCF/CTNNB1
538   binding affinity of the model (Table 4) for WNT OFF (k9/k8=320, pink line) and WNT ON (k9/k8=33.5, blue line). Note that, although for WNT
539   ON the value of the N/C-ratio increases with k3, there is still nuclear exclusion (N/C-ratio lower than 1, dashed line) at the value of k3 that
540   matches the cytoplasmic CTNNB1-concentration (dotted line). I-K) The N/C-ratio as measured by FCS for wild-type and S45F mutant (I), after
541   24-hour CHIR99021 treatment (J) and after 4 hour WNT3A treatment (K). Note that all perturbations lead to nuclear accumulation (N/C-
542   value exceeding 1). L) Graph showing the predicted N/C-ratio as a function of k3 with the WNT ON value for k9/k8 with the nuclear shuttling
543   ratio of the model (k6/k7 Table 4),corresponding to WNT OFF (k6/k7=0.96, pink line) and WNT ON (k6/k7=1.17, blue line), respectively. Note
544   that the WNT ON value of k6/k7 increases the N/C-ratio to nuclear accumulation at the value for k3 that matches the cytoplasmic
545   concentration (dotted line). M) Graph depicting the predicted total cytoplasmic CTNNB1 concentration as a function of k3 with WNT ON and
546   WNT OFF values for k9/k8 and k6/k7Note that modulation of k9/k8 and k6/k7 has no effect on the predicted cytoplasmic concentration of
547   CTNNB1. The horizontal solid line is the experimentally determined cytoplasmic CTBNN1 concentration (cf. panel B); the vertical dotted line
548   is at the value of k3 that best reproduces this experimental finding in the model. N) Graph depicting the predicted total nuclear CTNNB1
549   concentration as a function of k3 for WNT ON and WNT OFF values for k9/k8 and k6/k7. Note that if both k9/k8 and k6/7 are changed from
550   their WNT OFF values the predicted nuclear concentration of CTBNN1 better matches the experimentally determined concentration
551   (horizontal solid line) at the value for k3 that matches the cytoplasm concentration (vertical dotted line).
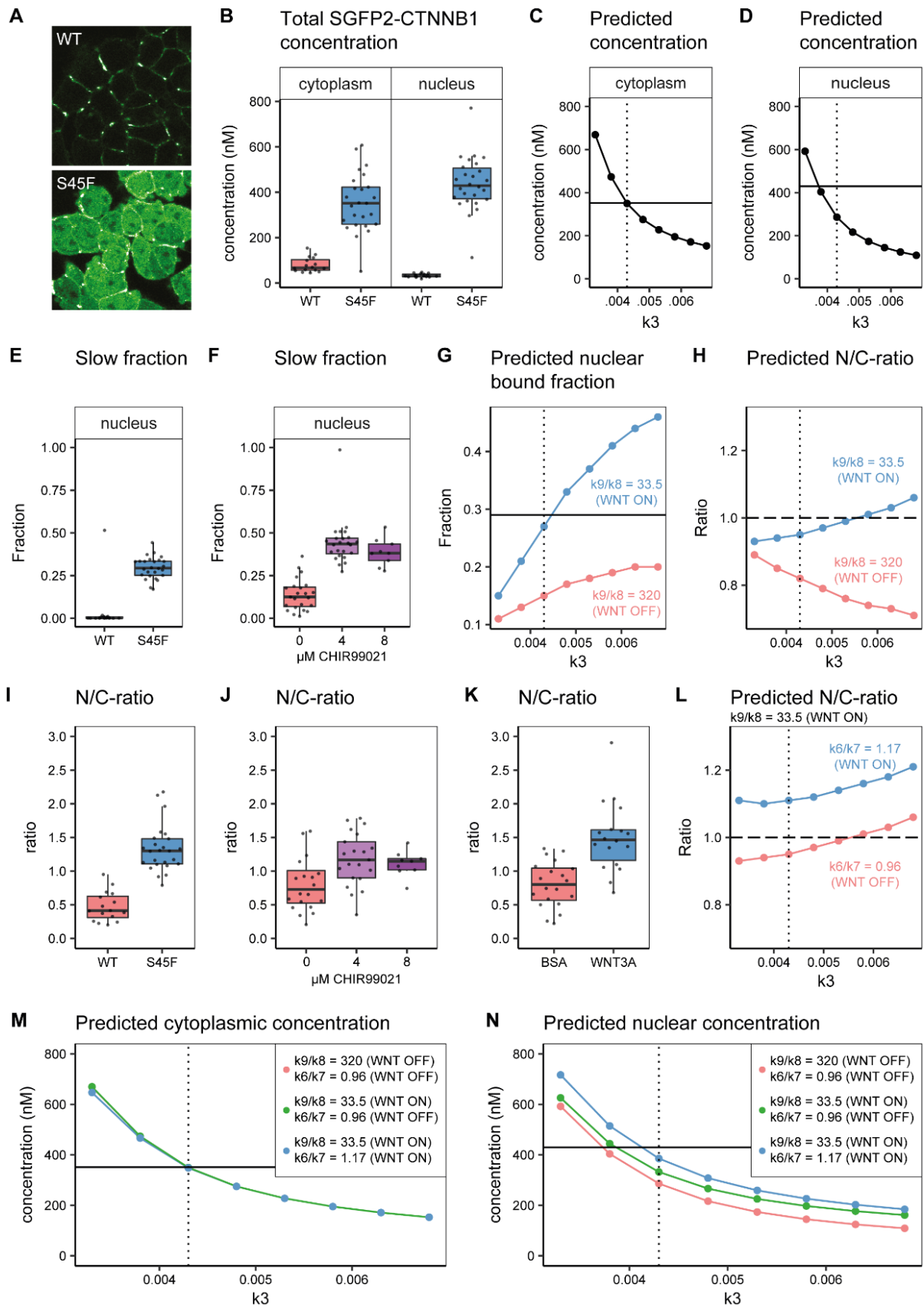
Discussion

553   WNT signaling is critical for tissue development and homeostasis. Although most core players

554   and many of their molecular interactions have been uncovered, dynamic spatiotemporal

555   information with sufficient subcellular resolution remains limited. As both genome editing

556

557   approaches and quantitative live-cell microscopy have advanced further, the goal of studying

558   WNT/CTNNB1 signaling at endogenous expression levels in living cells now is within reach.

559   Maintaining endogenous expression levels is important, as overexpression may lead to

560   altered stoichiometry of signaling components, as well as changes in subcellular localization

561   (Gibson et al., 2013; Mahen et al., 2014). Indeed, it has been shown that exogenously

562   expressed CTNNB1 is less signaling competent, probably due to its post-translational

563   modification status (Hendriksen et al., 2008). Here we generated functional HAP1$^{SGFP2\text{-}CTNNB1}$

564   knock-in cell lines to study the dynamic behavior and subcellular complex state of

565   endogenous CTNNB1 in individual living human cells in both a physiological and oncogenic

566   context.

567   Using live-cell microscopy and automated cell segmentation, we observe that endogenous

568   CTNNB1 only increases 1.7-fold in the cytoplasm and 3.0-fold in the nucleus after WNT3A

569   treatment, which is consistent with the literature (Jacobsen et al., 2016; Kafri et al., 2016;

570   Massey et al., 2019).

571   Next, we used state-of-the-art, quantitative microscopy to measure the absolute

572   concentration of CTNNB1 within different subcellular compartments and in different

573   complex-states in living cells. The findings from these experiments challenge the dogma that

574   mainly monomeric CTNNB1 accumulates upon WNT pathway stimulation. Moreover, our

575   integrative approach of quantitative imaging and computational modelling revealed three

30

576   critical nodes of CTNNB1 regulation, namely CTNNB1 degradation, nuclear shuttling and

577   nuclear retention, which together describe the CTNNB1 turnover, subcellular localization and

578   complex status under both physiological and oncogenic conditions.

579   Cytoplasmic regulation of CTNNB1

580   Using FCS, we determined that in unstimulated HAP1 cells a substantial fraction of SGFP2-

581   CTNNB1 is associated with a very large, slow-diffusing cytoplasmic complex (Figure 4-5). The

582   main known cytoplasmic complex containing CTNNB1 is the destruction complex. The

583   combined weight of the individual destruction complex components (AXIN, APC, CSNK1 and

584   GSK3) would be expected to result in a much higher mobility than that displayed by the

585   cytoplasmic CTNNB1-containing complex we observed. However, evidence is growing that

586   the destruction complex forms large phase separated aggregates (also termed biomolecular

587   condensates) (reviewed in Schaefer and Peifer, 2019). Oligomerization of AXIN and APC

588   underlies the formation of these aggregates, and this in turn appears to be required for

589   efficient degradation of CTNNB1 (Fiedler et al., 2011; Kunttas-Tatli et al., 2014; Pronobis et

590   al., 2017; Spink et al., 2000). There is some evidence that these aggregates form at (near)

591   endogenous levels (Fagotto et al., 1999; Faux et al., 2008; Mendoza-Topaz et al., 2011;

592   Pronobis et al., 2015; Schaefer et al., 2018; Thorvaldsen et al., 2015), but it is still an open

593   question what the exact composition and size of the destruction complex is in a physiological

594   context. It should be noted that our imaging does not visualize such aggregates (Figure 3A).

595   In addition, our N&B data indicate that few, if any, complexes exist that contain multiple

596   SGFP2-CTNNB1 molecules in the absence or presence of WNT3A stimulation – something that

597   would be expected in biomolecular condensates formed by the oligomerization of CTNNB1

598   binding partners. Only following the introduction of an S45F mutation, which results in

31

599   constitutive inhibition of CTNNB1 phosphorylation and degradation, we observe a brightness

600   increase that would be compatible with the accumulation of multiple SGFP2-CTNNB1^{S45F}

601   molecules in a single cytoplasmic complex. This indicates that while the destruction complex

602   might be multivalent in both a physiological and an oncogenic context, CTNNB1 occupancy of

603   the complex is low under physiological conditions, but increased in oncogenic signaling. This

604   has major impacts on how we conceptualize the workings of the CTNNB1 destruction

605   machinery – especially in the context of cancer, since mutations in CTNNB1 (affecting

606   occupancy) may have very different biochemical consequences than mutations in APC

607   (affecting multimerization and valency of the destruction complex itself).

608   The mechanism on destruction complex deactivation remains controversial (Tortelote et al.,

609   2017; Verkaar et al., 2012). The current literature suggests that the destruction complex is

610   sequestered to the FZD-LRP receptor complex upon WNT pathway stimulation. Several

611   models exist for how the membrane sequestration inhibits CTNNB1 degradation, including

612   LRP mediated GSK3 inhibition (Stamos et al., 2014), sequestration of GSK3 in multi vesicular

613   bodies (Taelman et al., 2010), (partial) dissociation of the destruction complex (Liu et al.,

614   2005; Tran and Polakis, 2012), and saturation of CTNNB1 within an intact destruction complex

615   (Li et al., 2012). Our data clearly show that a substantial fraction of CTNNB1 in the cytoplasm

616   remains bound upon pathway stimulation (Figure 5D). This is not predicted by any of the

617   above mentioned models and challenges the long-held view that mainly monomeric CTNNB1

618   accumulates.

619   Additionally, we show that the cytoplasmic CTNNB1 complex in WNT3A or CHIR99021 treated

620   cells as well as in S45F mutant cells has an increased mobility compared to control cells (Figure

621   5E). Therefore, while the diffusion coefficient is still very low (indicating a very large complex),

32

622   this implies it is a vastly different complex than that observed in the absence of WNT

623   stimulation. The fact that cells in which GSK3 phosphorylation is inhibited through S45F

624   mutation or CHIR99021 treatment show similar behavior, suggests that the size of the

625   cytoplasmic complex is directly linked to the phosphorylation status of CTNNB1. The

626   destruction complex has been shown to associate with (parts of) the ubiquitin and

627   proteasome machinery (Li et al., 2012; Lui et al., 2011; Schaefer et al., 2020). One interesting

628   possibility, therefore, is that phosphorylated CTNNB1 is required for coupling the destruction

629   complex to the ubiquitination and proteasome machinery. In fact, although not explicitly

630   mentioned in the main text, supplementary table 1 of Li et al., 2012 shows that in HEK293

631   cells, which harbor no mutation in the core components of the WNT pathway, CTNNB1 was

632   found to interact with subunits of the proteasome, whereas in the S45F-CTNNB1 mutant cell

633   line Ls174T these interactions were not detected. In conclusion, although we do not directly

634   determine its identity, our measured biophysical parameters of the cytoplasmic CTNNB1

635   complex are consistent with it representing a large, multivalent destruction complex that is

636   coupled to the proteasome as long as CTNNB1 is being phosphorylated.

637   Nuclear regulation of CTNNB1

638   The key function of CTNNB1 downstream of WNT is to regulate transcription of TCF/LEF target

639   genes (Doumpas et al., 2019; Schuijers et al., 2014). Proteomic analyses have shown that the

640   WNT enhanceosome consists of CTNNB1, TCF/LEF, PYGO and BCL9 and several other large

641   proteins (Fiedler et al., 2015; van Tienen et al., 2017). Using FCS, we showed that CTNNB1

642   resides in a nuclear complex with a diffusion coefficient that is compatible with such a DNA-

643   bound transcriptional complex (Figure 5E) (Lam et al., 2012).

644   Although CTNNB1 is known to associate with TCF/LEF factors in response to WNT/CTNNB1

645   signaling to drive transcription (Franz et al., 2017; Schuijers et al., 2014), we also detect low

646   levels of nuclear CTNNB1 complex in the absence of a WNT stimulus (Figure 5C). The diffusion

647   coefficient of the nuclear CTNNB1 complex does not change upon the addition of WNT3A

648   (Figure 5E), suggesting that some CTNNB1 is already associated with the DNA even in the

649   absence of a WNT stimulus. At this point, we cannot exclude the contribution of TCF/LEF

650   independent DNA binding (Armstrong et al., 2012; Essers et al., 2005; Kormish et al., 2010),

651   or anomalous subdiffusion in the nucleus, either due to physical obstruction , transient DNA-

652   binding events protein or protein complex formation (Dross et al., 2009; Kaur et al., 2013;

653   Wachsmuth et al., 2000), as FCS only allows us to probe the speed of this complex.

654   However, upon pathway activation through WNT3A, CHIR99021 or S45F mutation we see a

655   consistent increase in the fraction and absolute levels of this slow-diffusing nuclear CTNNB1

656   complex (Figure 5E, Figure 8E-F), compatible with increased CTNNB1 binding to its target

657   sites. For WNT stimulation, we measured that the concentration of bound SGFP2-CTNNB1 in

658   the nucleus increased to a 89 nM, which corresponds to something in the order of 20,000

659   bound CTNNB1 molecules in one nucleus, assuming a small nuclear volume of 0.36 pL (Tan et

660   al., 2012). Published CHIPseq studies report many CTNNB1 DNA binding sites, ranging from

661   several hundred to several thousand sites in mammalian cells (Cantù et al., 2018; Doumpas

662   et al., 2019; Schuijers et al., 2014). It is therefore highly likely that at least part of the slow-

663   diffusing CTNNB1 particles we measure indeed represents CTNNB1 that is associated with the

664   WNT enhanceosome.

665   Regulation of CTNNB1 nuclear accumulation

666   In HAP1 cells, endogenous CTNNB1 is excluded from the nucleus in the absence of WNT. Our

667   live imaging data reveal an immediate and preferential increase in nuclear CTNNB1 upon

668   WNT3A stimulation, until an equilibrium is reached between the cytoplasmic and nuclear

669   levels (Figure 3D). This is consistent with previous observations in HEK293 cells stably

670   overexpressing low levels of YFP-CTNNB1 (Kafri et al., 2016).

671   Intriguingly, CTNNB1 does not contain nuclear import or export signals and can translocate

672   independently of classical importin and exporter pathways (Fagotto et al., 1998; Wiechens

673   and Fagotto, 2001; Yokoya et al., 1999). Hence, the molecular mechanism of CTNNB1

674   subcellular distribution remains incompletely understood. Evidence from Fluorescence

675   Recovery After Photobleaching (FRAP) studies suggest that the increase in nuclear CTNNB1 is

676   due to changes in binding to its interaction partners in the cytoplasm and nucleus (retention)

677   rather than active changes in nuclear import and export rates (shuttling) (Jamieson et al.,

678   2011; Krieghoff et al., 2006). We argue that the two are not mutually exclusive, as our

679   experimental data and computational model show that WNT regulates both

680   nucleocytoplasmic shuttling and nuclear retention of CTNNB1. Indeed, we see an increase of

681   nuclear CTNNB1 complexes in the nucleus (Figure 5C-D) and the dissociation of CTNNB1 from

682   TCF is reduced almost 10-fold in WNT signaling conditions in our computational model (Table

683   5). Our model predicts that this increased nuclear retention indeed also increases the

684   nuclear/cytoplasmic ratio (Figure 8H). However, to reconcile our computational prediction

685   with our experimental observations we additionally need to include a shift from nuclear

686   export to nuclear import upon pathway activation (Figure 6, Figure 8). Our integrated

687   experimental biology and computational modelling approach thus reveals that WNT signaling

688 not only regulates the absolute levels of CTNNB1 through destruction complex inactivation,

689 but also actively changes its subcellular distribution through nuclear retention and shuttling.

690 The fact that direct inhibition of GSK3 mediated phosphorylation of CTNNB1 results in the

691 same behavior, indicates that the phosphorylation status of CTNNB1 plays a critical role. This

692 further emphasizes the importance of posttranslational modifications and conformational

693 changes in CTNNB1 for its subcellular localization and function (Gottardi and Gumbiner, 2004;

694 Sayat et al., 2008; Valenta et al., 2012; van der Wal and van Amerongen, 2020; Wu et al.,

695 2008) .

696 <u>Challenges and opportunities for fluorescence fluctuation spectroscopy techniques</u>

697 Using fluorescence fluctuation spectroscopy techniques (FCS and N&B) we have quantified

698 endogenous CTNNB1 concentrations and complexes in living cells for the first time, which

699 provided novel and long-awaited biophysical parameters for computational modelling.

700 Moreover, our approach has also yielded novel insights into CTNNB1 regulation that challenge

701 current dogmas in the field. If we are correct, this has important consequences. First, if only

702 part of the cytoplasmic CTNNB1 pool is uncomplexed (i.e. free or monomeric), regardless of

703 whether the WNT/CTNNB1 pathway is off or on (either via physiological WNT3A stimulation

704 or via oncogenic activation), this is a rewrite of the textbook model. Second, if the slow-

705 diffusion cytoplasmic CTNNB1 complex indeed represents a proteasome-associated

706 destruction complex, this would fuel a debate that has remained unresolved for many years

707 (Li et al., 2012; Verkaar et al., 2012). As more studies will use these image-based techniques

708 to determine biophysical properties of WNT/CTNNB1 signaling components (Ambrosi et al.,

709 2020; Eckert et al., 2020), the field will undoubtedly learn how to interpret these findings.

710   As with any technique, there are several limitations to consider. First of all, for the

711   determination of the absolute concentration by FCS it should be noted that a small portion of

712   SGFP2-CTNNB1 could be in a non-fluorescent state. Although our FCS analysis model already

713   accounts for dynamic dark states such as the triplet state, non-matured fluorophores could

714   lead to a slight underestimation of our concentrations. However, this is expected to be a very

715   small fraction as SGFP2 has very good maturation kinetics (Kremers et al., 2007). Secondly,

716   our findings concerning the diffusion kinetics are limited by the assumptions we make in the

717   FCS fitting model. Although obvious mistakes in underlying assumptions immediately become

718   clear due to bad fitting results and can therefore be excluded, not every wrong assumption

719   will stand out accordingly. Our data clearly shows that assuming only one diffusion speed for

720   CTNNB1 in HAP1 cells would be incorrect (Figure 4). However, whether with the second

721   diffusion speed we measure a single distinct, large complex, or rather an average of multiple

722   different CTNNB1 containing complexes cannot be determined in our current set-up. In

723   addition, we assume that CTNNB1 is present as a free-floating monomer (as fixed for our first

724   component), based on previous observations (Gottardi and Gumbiner, 2004; Maher et al.,

725   2010). However, at least one report suggests that CTNNB1 is not present as a monomer but

726   rather in small cytoplasmic complexes of ~200 kDa (Gerlach et al., 2014). As diffusion speed

727   is relatively insensitive to differences in size (e.g. an 8-fold increase in protein mass is

728   expected to result in only a 2-fold reduction of the diffusion coefficient for a spherical

729   particle), it is possible that we do not measure truly free-floating CTNNB1, but rather smaller

730   complexes. In addition, point FCS is limited to a single position in the cell. Therefore, in

731   addition to the intercellular differences in the WNT signaling response of individual cells, our

732   measurements also sample intracellular heterogeneity caused by the presence of organelles

733   and molecular crowding. Notwithstanding these limitations, we have been able to show that

734   a large portion of CTNNB1 is present in a very large complex in both stimulated and

735   unstimulated conditions and that this complex has a statistically and biologically significant

736   different speed after WNT3A treatment.

737   The biophysical parameters we obtained from point FCS and N&B have allowed us to learn

738   more about the speed and occupancy of the SGFP2-CTNNB1 complexes in living cells.

739   Moreover, using different stimuli and perturbations of the pathway we have been able to link

740   this to the phosphorylation status of CTNNB1. However, FCS and N&B do not provide

741   conclusive evidence on the identity and composition of these complexes. An exciting

742   possibility would be to label additional components presumed to be present in the CTNNB1-

743   containing complexes at the endogenous level to uncover the precise composition and

744   stoichiometry of protein complexes involved in WNT signaling. For instance, Fluorescence

745   Cross Correlation Spectroscopy (FCCS) could be employed to test if two proteins reside within

746   the same complex (Elson, 2011; Hink, 2014; Macháň and Wohland, 2014). Ultimately, a

747   combination of such quantitative functional imaging techniques, biochemical and proteomic

748   approaches, together with additional perturbations will need to be employed to further our

749   understanding of the dynamic composition of endogenous CTNNB1 complexes, as well as to

750   help us resolve the molecular mechanism underlying nucleocytoplasmic shuttling and nuclear

751   retention. As both genome editing and live cell imaging techniques continue to improve,

752   additional possibilities will open up to address longstanding questions in cellular signaling in

753   a physiological context with high spatial and temporal resolution. New opportunities and

754   challenges await as these investigations extend to 3D organoid cultures, developing embryos

755   and living organisms.

Material and Methods

DNA Constructs

The following constructs were used: pSpCas9(BB)-2A-Puro (PX459) V2.0 ((Ran et al., 2013), a kind gift from Feng Zhang, available from Addgene, plasmid #62988), MegaTopflash ((Hu et al., 2007), a kind gift from Dr. Christophe Fuerer and Dr. Roel Nusse, Stanford University), CMV Renilla (E2261,Promega, Madison, WI), pSGFP2-C1 ((Kremers et al., 2007), a kind gift from Dorus Gadella, available from Addgene, plasmid #22881), pmScarlet-i_C1 (Bindels et al., 2017), a kind gift from Dorus Gadella, available from Addgene, plasmid # 85044), pSYFP2-C1 ((Kremers et al., 2006),a kind gift from Dorus Gadella, available from Addgene, plasmid #22878), mTurquoise2-C1 ((Goedhart et al., 2012), a kind gift from Dorus Gadella, available from Addgene, plasmid # 54842), pEGFP (Clontech, Mountain View, CA), $pEGFP_2$ and $pEGFP_3$ ((Pack et al., 2006), a kind gift from Masataka Kinjo) and pBluescript II KS(+) (Stratagene, La Jolla, CA).

The gRNA targeting the start codon in exon2 of human *CTNNB1* was designed using the MIT webtool (crispr.mit.edu) and cloned into pX459. Oligos RVA567 and RVA568 (Table 6) encoding the gRNA were annealed, and ligated into BbsI-digested pX459 plasmid as previously described (Ran et al., 2013) to obtain pX459-CTNNB1-ATG. The gRNA targeting codon 3 of *CTNNB1* for mutagenesis of Serine 45 to Phenylalanine (S45F) was similarly designed and cloned by introducing RVA561 and RVA562 (Table 6) into pX459, yielding pX459-CTNNB1-S45.

The repair plasmid for SGFP2-CTNNB1 (pRepair-SGFP2-CTNNB1) was cloned using Gibson cloning (Gibson et al., 2009). First, a repair plasmid including the Kozak sequence from the pSGFP2-C1 plasmid was generated (pRepair-Kozak-SGFP2 -CTNNB1). For this, 5' and 3'

779   homology arms were PCR amplified from genomic HEK293A DNA with primers RVA618 and

780   RVA581 (5' arm) or RVA619 and RVA584 (3' arm). SGFP2 was amplified with Gibson cloning

781   from pSGFP2-C1 with primers RVA582 and RVA583 and the backbone was amplified from SacI

782   digested pBlueScript KS(+) with primers RVA622 and RVA623. The final repair construct

783   (pRepair-SGFP2-CTNNB1) contains the endogenous *CTNNB1* Kozak sequence before the

784   SGFP2 ATG. To obtain (pRepair-SGFP2-CTNNB1), the backbone and homology regions were

785   amplified from pRepair-SGFP2-Kozak-CTNNB1 with primers RVA1616 and RVA1619 and an

786   SGFP2 without the Kozak sequence was amplified from pSGFP2-C1 with primers RVA1617 and

787   RVA1618. To generate color variants of the repair plasmid SYFP2, mScarlet-i and mTurquoise2

788   were also amplified from their respective C1 vectors with primers RVA 1617 and RVA 1618.

789   PCR products were purified and assembled with a Gibson assembly master mix with a 1:3

790   (vector:insert) molar ratio. Gibson assembly master mix was either purchased (E2611S, NEB)

791   or homemade (final concentrations: 1x ISO buffer (100mM Tris-HCL pH 7.5, 10mM MgCl2,

792   0.2M dNTPs (R0181, Thermo Scientific), 10mM DTT (10792782, Fisher), 5% PEG-8000

793   (1546605, Sigma-Aldrich, St Louis, MO), 1mM NAD+ (B9007S, NEB)), 0.004 U/µl T5

794   exonuclease (M0363S, NEB), 0.5 U/µl Phusion DNA Polymerase (F-530L, Thermo Scientific)

795   and 4 U/µl Taq DNA ligase (M0208S, NEB)).

796   The following plasmids are available from Addgene: pX459-CTNNB1-ATG (#153429), pX459-

797   CTNNB1-S45   (#164587),   pRepair-SGFP2-CTNNB1   (#153430),   pRepair-mScI-CTNNB1

798   (#153431), pRepair-SYFP2-CTNNB1 (#153432), pRepair-mTq2-CTNNB1 (#153433)).

799

Primers used

Table 6: primers/oligonucleotides used in this study

RVA24	CAAGTTTGTTGTAGGATATGCCC
RVA25	CGATGTCAATAGGACTCCAGA
RVA124	AGTGTGAGGTCCACGGAAA
RVA125	CCGTCATGGACATGGAAT
RVA555	GCCAAACGCTGGACATTAGT
RVA558	AGACCATGAGGTCTGCGTTT
RVA561	CACCGTTGCCTTTACCACTCAGAGA
RVA 562	AAACTCTCTGAGTGGTAAAGGCAAC
RVA567	CACCGTGAGTAGCCATTGTCCACGC
RVA568	AAACGCGTGGACAATGGCTACTCAC
RVA581	tgctcaccatggtggGATTTTCAAAACAGTTGTATGGTATACTTC
RVA582	actgttttgaaaatcCCACCATGGTGAGCAAGGGC
RVA583	agtagccattgtccaCTTGTACAGCTCGTCCATGCCG
RVA584	gacgagctgtacaagTGGACAATGGCTACTCAAGGTTTG
RVA618	atacgactcactatagggcgaattggagctGATGCAGTTTTTTTCAATATTGC
RVA619	ttctagagcggccgccaccgcggtggagctCTCTCTTTTCTTCACCACAACATTTTATTTAAAC
RVA622	AAGAGAGAGCTCCACCGCGGTGGCGGCCG
RVA623	TGCATCAGCTCCAATTCGCCCTATAGTGAGTCG
RVA1616	tgtccacgctgGATTTTCAAAACAGTTGTATGG
RVA1617	atacaactgttttgaaaatccagcgtggacaATGGTGAGCAAGGGCGAG
RVA1618	cacaaaccttgagtagccatCTTGTACAGCTCGTCCATGC
RVA1619	ATGGCTACTCAAGGTTTGTGTCATTAAATC
RVA2540	CTTACCTGGACTCTGGAATCCATTCTGGTGCCACTACCACAGCTCCTTTCCTGTCCGGTAAAGGCAATCCTGAGGAAGAGGATGTGGATACCTCCCAAGT

Cell Culture, Treatment and Transfection

HAP1 cells (a kind gift from Thijn Brummelkamp, NKI) were maintained in full medium (colorless IMDM (21056023, Gibco, Thermo Fisher Scientific, Waltham, MA) supplemented with 10% FBS (10270106, Gibco) and 1X Glutamax (35050061, Gibco)) under 5% CO2 at 37°C in humidifying conditions and passaged every 2-3 days using 0.25% Trypsin-EDTA (25200056, Gibco). Cells were routinely tested for mycoplasma. We verified the haploid identity of the parental HAP1^{WT} by karyotyping of metaphase spreads. To maintain a haploid population, cells were resorted frequently (see below) and experiments were performed with low passage number cells.

41

812   Where indicated, cells were treated with CHIR99021 (6mM stock solution in DMSO) (1677-5,

813   Biovision, Milpitas, CA) or Recombinant Mouse Wnt-3a (10µg/ml stock solution in 0.1% BSA

814   in PBS) (1324-WN-002, R&D systems, Bio-Techne, Minneapolis, MN) with DMSO and 0.1% BSA

815   in PBS as vehicle controls, respectively.

816   Cells were transfected using Turbofect (R0531, ThermoFisher, Thermo Fisher Scientific,

817   Waltham, MA), X-tremeGene HP (6366546001, Roche, Basel, Switzerland) or Lipofectamine

818   3000 (Invitrogen, Thermo Fisher Scientific, Waltham, MA) in Opti-MEM (Gibco) according to

819   the manufacturer's instructions.

HAP1$^{SGFP2-CTNNB1}$ and HAP1$^{SGFP2-CTNNB1(S45F)}$ generation

821   800.000 HAP1 cells/well were plated on 6-well plates. The following day, cells were

822   transfected with Turbofect and 2000 ng DNA. pX459-CTNNB1-ATG and pRepair-SGFP2-

823   CTNNB1 were transfected in a 2:1, 1:1 or 1:2 ratio. pSGFP2-C1, pX459 or pX459-CTNNB1-ATG

824   were used as controls. From 24 to 48 hours after transfection cells were selected with 0.75

825   µg/ml puromycin (A1113803, Gibco). Next, cells were expanded and passaged as needed until

826   FACS sorting at day 9. For FACS analysis and sorting cells were washed, trypsinized,

827   resuspended with full medium and spun down at 1000 rpm for 4 minutes. For sorting, cells

828   were stained with 1 µg/ml Dapi (D1306, Invitrogen) in HF (2 % FBS in HBSS (14175053, Gibco)),

829   washed with HF and resuspended in HF. To determine the haploid population, a separate

830   sample of cells was stained with 5 µM Vybrant® DyeCycleTM Violet Stain (V35003, Invitrogen)

831   in full medium for 30 minutes and kept in vibrant containing medium. Cells were filtered with

832   a 70 µm filter and then used for FACS sorting and analysis on a FACSARIA3 (BD, Franklin Lanes,

833   NJ). Vybrant-stained cells were analyzed at 37° and used to set a size gate only containing

834   haploid cells. Dapi-stained cells were single cell sorted at 4°C into 96-well plates, that were

835   previously coated overnight with 0.1 % gelatin (G9391, Sigma-Aldrich) in MQ and contained

836   full medium supplemented with 1 % penicillin/streptomycin (15140122, Gibco) and 0.025 M

837   HEPES (H3375 Sigma-Aldrich, 1 M stock solution, pH 7.4, filter sterilized). The 3 independent

838   clones used in this study were obtained from separate transfections of the same parental cell

839   line. Clones were genotyped and sanger sequenced using primers RVA555 and RVA558 (Table

840   6).

841   HAP1$^{SGFP2-CTNNB1(S45F)}$ were generated from HAP1$^{SGFP2-CTNNB1}$ clone 1. The same procedure as

842   above was followed with slight adaptations; Cells were transfected 1000 ng

843   pX459-CTNNB1-S45 or pX459 with 2 or 4 µl 10mM repair oligo (RVA 2540) with Turbofect,

844   selected with puromycin and expanded as described above. Haploid single cells were sorted

845   after 11 days as described above. For haploid size discrimination Vybrant™ DyeCycle™ Ruby

846   Stain (V10273) was used. The 5 clones used in this study were obtained from 2 separate

847   transfection (clone 2,3,16,24 from the same transfection, clone 27 from a second

848   transfection). Clones were genotyped using primers RVA555 and RVA558 (Table 6), followed

849   by HpaII (ER0511, ThermoFisher) restriction as per the manufacturer's instruction. RVA555

850   was used for sanger sequencing.

851   Resorting of the cell lines was also performed with the same FACS procedure, with collection

852   of cells in 15 mL tubes containing full medium with 1 % penicillin and 0.025 M HEPES.

853   FACS data were analyzed and visualized with FlowJo™.

854   Luciferase Assay

855   For luciferase assays, 100.000 cells per well were seeded on a 24-well plate. Cells were

856   transfected with 1µl X-tremeGene HP and 400 ng MegaTopflash reporter and 100 ng CMV-

857   Renilla or 500 ng SGFP2-C1 as a negative control 24 hours later. Cells were treated with the

43

858   indicated concentration of CHIR99021 24 hours after transfection and after another 24 hours

859   medium was removed and the cells were harvested with 50 µl Passive Lysis Buffer (E1941,

860   Promega). Luciferase activity was measured on a GloMax Navigator (Promega) using 10µl

861   lysate in a black OptiPlate 96-well plate (6005279, Perkin Elmer, Waltham, MA) and 50 µL

862   homemade firefly and luciferase reagents (according to (Fuerer et al., 2014; Hampf and

863   Gossen, 2006)).

864   For luciferase assays, three technical replicates (i.e. three wells transfected with the same

865   transfection master mix) were pipetted and measured for each sample in each experiment.

866   For each technical triplicate, the average MegaTopflash activity was calculated and depicted

867   as a single dot in Figure 2C and Figure 7 supplement 1G. Three independent biological

868   experiments, each thus depicted as an individual dot, were performed. To calculate

869   MegaTopflash activity, Renilla and Luciferase luminescence values were corrected by

870   subtracting the average background measured in the SGFP2-transfected control.

871   MegaTopflash activity was calculated as the ratio of corrected Firefly and Renilla

872   luminescence and normalized to the average reporter activity of the relative DMSO control.

873   <u>Western Blot</u>

874   The remaining lysates from the technical triplicates of the luciferase assay were combined

875   and they were cleared by centrifugation for 10 minutes at 12.000 g at 4°C. Western blot

876   analysis was performed and quantified as previously described (Jacobsen et al., 2016).

877   Antibodies were used with the following dilutions, 1:1000 Non-phosphorylated (Active) β-

878   catenin clone D13A1 (8814S, Cell Signaling, Danvers, MA), 1:2000 total β-catenin clone 14

879   (610153, BD), 1:1000 α-Tubulin clone DM1A (T9026, Sigma-Aldrich), 1:1000 GFP polyclonal

880   (A-6455, Invitrogen), 1:20.000 IRDye 680LT Goat anti-Rabbit IgG (926-68021, LI-COR, Lincoln,

881   NE), 1:20.000 IRDye 800CW Donkey anti-Mouse IgG (926–32212, LI-COR). Raw data for all

882   blots have been made available at https://osf.io/vkexg/.

883   qRT-PCR

884   For qRT-PCR analysis, 100.000 HAP1 cells per well were seeded on a 24-well plate. After 48

885   hours, cells were treated with indicated concentrations of CHIR99021. Cells were harvested

886   24 hours after treatment. RNA was isolated with Trizol (15596018, Invitrogen) according to

887   the manufacturer's instructions. cDNA was synthesized using SuperScriptIV (18090010,

888   Invitrogen) according to the manufacturer's instructions. qRT-PCR was performed with

889   SyberGreen (10710004, Invitrogen). The endogenous WNT target gene *AXIN2* was amplified

890   using primers RVA124 and RVA125, and HPRT housekeeping control was amplified using

891   primers RVA24 and RVA25.

892   For qRT-PCR experiments, three technical replicates (i.e. three reactions with the same cDNA)

893   were pipetted and measured for each sample in each experiment. For each technical

894   triplicate, the mean fold-change in AXIN2 expression was calculated and depicted as a single

895   dot in Figure 2D and Figure 7 supplement 1H. Three independent biological experiments, each

896   thus depicted as an individual dot, were performed. Relative expression levels of *AXIN2* were

897   calculated using the comparative Delta-Ct method (Livak and Schmittgen, 2001; Schmittgen

898   and Livak, 2008). Briefly, *AXIN2* expression was normalized for *HPRT* expression and then the

899   relative fold-change to a WT DMSO sample was calculated for all clones and conditions.

900   Time-lapse imaging

901   The day before imaging, 88.000 cells/well were seeded on an 8 well chamber slide with glass

902   bottom (80827-90, Ibidi, Gräfelfing, Germany). HAP1$^{SGFP2-CTNNB1}$ clone 2 was used for the main

903   Figure 3, all 3 clones were used for Figure 3 supplement 1. HAP1$^{SGFP2-CTNNB1(S45F)}$ clone 2 was

904   imaged for Figure 8A. Approximately 6 hours before imaging, medium was replaced with full

905   medium supplemented with 1% penicillin/streptomycin, 0.025M HEPES and 500nM SiR-DNA

906   (SC007, Spirochrome, Stein am Rhein, Switzerland). Time lapse experiments were performed

907   on an SP8 confocal microscope (Leica Microsystems, Wetzlar, Germany) at 37°C with a HC PL

908   APO CS2 63x/1.40 oil objective (15506350, Leica), 488 and 633 lasers, appropriate AOBS

909   settings, using HyD detectors for fluorescent signal with a 496-555 for SGFP2-CTNNB1 and

910   643-764 bandpass for SiR-DNA, and a transmission PMT. Using multi-position acquisition, up

911   to 24 images were captured every 5 minutes. Focus was maintained using AFC autofocus

912   control on demand for every time point and position. Automated cell segmentation and

913   intensity quantification was performed using a custom CellProfiler™ pipeline (made available

914   at https://osf.io/6pmwf/). Output data was further analyzed in R/RStudio. Cells with a

915   segmented cytoplasmic area of less than 10 pixels were excluded. Intensities were normalized

916   per position to the average intensity in the cellular compartment (nucleus or cytoplasm) for

917   that position before the addition of the compounds. The imaging settings resulted in low

918   signal in regions not occupied by cells (~10% of the nuclear intensity, and ~5% of the

919   cytoplasmic intensity in untreated cells), and the data was therefore not background-

920   corrected. The nuclear cytoplasmic ratio was calculated by dividing the raw nuclear intensity

921   by the raw cytoplasmic intensity. Movies and still images were extracted with FIJI/ImageJ.

922   FCS and N&B cell preparation and general settings

923   Two days before FCS and N&B experiments, 44.000 cells/well were seeded on an 8-well

924   chamber slide with a glass bottom (80827-90, Ibidi). For low, FFS-compatible expression of

925   control samples, HAP1^{WT} cells were transfected with ~5 ng pSGFP2-C1, pEGFP (monomer),

926   pEGFP$_2$ (dimer) or pEGFP$_3$ (trimer) and ~200 ng pBlueScript KS(+) per well with Turbofect, X-

927   tremeGene HP or Lipofectamine 3000 the day before the experiment. Lipofectamine 3000

928   yielded the best transfection efficiency. For Figure 4, 5, 8K and accompanying supplements,

929   HAP1$^{SGFP2-CTNNB1}$ clone 2 was used. For Figure 7, 8 and accompanying supplements, CHIR99021

930   data was recorded and pooled for all three HAP1$^{SGFP2-CTNNB1}$ clones, and S45F data was

931   recorded and pooled from HAP1$^{SGFP2-CTNNB1(S45F)}$ clones 2, 24 and 27 and HAP1$^{SGFP2-CTNNB1}$ clone

932   1 (the parental line for these S45F mutant clones) was used as the wild-type control.

933   FCS and N&B measurements were performed on an Olympus FV-1000 equipped with SepiaII

934   and PicoHarp 300 modules (Picoquant, Berlin, Germany) at room temperature. An Olympus

935   60x water immersed UPLS Apochromat (N.A. 1.2) objective was used for FCS acquisition and

936   Figure 3 supplement 1E, and an Olympus 60x silicon immersed UPLS Apochromat (N.A. 1.4)

937   objective was used for N&B measurements. Green fluorophores were excited with a 488 nm

938   diode laser (Picoquant) pulsing at 20 MHz and detected through a 405/480-488/560/635 nm

939   dichroic mirror (Chroma, Bellows Falls, VT) and 525df45 nm bandpass filter (Semrock,

940   Rochester, NY) with an Avalanche Photodiode (APD) (MPD, Bolzano, Italy). For, figure 2

941   supplement 1E and for FCS and N&B reference images the same laser and dichroic were used,

942   but the signal was detected through a 505-540 bandpass filter with an internal PMT of the FV-

943   1000 Olympus microscope.

944   <u>FCS data acquisition and analysis</u>

945   For FCS measurements, a confocal image was recorded. In this reference image, a single pixel

946   was set as region of interest (ROI), based on its localization in the cytoplasm or nucleus as

947   judged by the transmission image. In this ROI, the fluorescence intensity was measured over

948   time using an APD, for typically 120 seconds.

949   FCS measurements were analyzed in FFS Dataprocessor version 2.3 (SSTC, Minsk, Belarus).

950   The autocorrelation curve ($G(\tau)$) was calculated from the measured intensity (I) according to

951   equation 1. Intensity traces with significant photobleaching, cell movement or focal drift were

952   excluded from further analysis (see supplementary file 1 – tab FCS measurements and fitting).

953   From other traces a portion of the trace with minimal (less than 10%) intensity drift or

954   bleaching was selected to generate autocorrelation curve (AC).

$$G(\tau) = 1 + \frac{<\delta I(t) * \delta I(t+\tau)>}{<I>^2} \qquad \text{Eq. 1}$$

955

956   The resulting AC was fitted with a Triplet-state-diffusion model, described in equation 2. G_∞

957   accounts for offset in the AC for example by intensity drift. N is the average of the number of

958   particles that reside in the confocal volume. F_{trip} and τ_{trip} describe the fraction of molecules in

959   the dark state and the relaxation of this dark state respectively. Of note, in this case, F_{trip} and

960   τ_{trip} account both for blinking of the fluorescent molecules and for the afterpulsing artefact of

961   the APD. $\tau_{diff,i}$ describes the diffusion rate of the fluorescent molecules with the corresponding

962   fraction, F_i. This diffusion time depends on the structural parameter (sp), which is defined as

963   the ratio of the axial (ω_z) over the radial axis (ω_{xy}) of the observation volume.

$$G(\tau) = G_\infty + \frac{1}{<N>} * \frac{F_{trip}}{1-F_{trip}} e^{\frac{-\tau}{\tau_{trip}}} * \sum_j \frac{F_i}{\left(1 + \frac{\tau}{\tau_{diff,i}}\right)\sqrt{1 + \frac{\tau}{\tau_{diff,i} * sp^2}}} \qquad \text{Eq. 2}$$

964   The apparent particle numbers (N_{apa}) for SGFP2-CTNNB1 were corrected for autofluorescence

965   and bleaching (equation 3). The autofluorescence ($I_{autofluorescence}$) of HAP1 cells in the

966   nucleus and cytoplasm was measured in untransfected HAP1 cells using the same settings as

967   for FCS measurements. The correction for moderate bleaching is based on the intensity of the

968   selected portion of the intensity trace for AC calculation (I$_{ana}$) and the intensity at the start of

969   the measurement (I$_{start}$).

970   The size and shape of the observation volume was calibrated daily by measuring Alexa Fluor™

971   488 NHS Ester (A20000, Molecular probes, Thermo Scientific, stock dilution in MQ) in PBS in

972   a black glass-bottom cell imaging plate with 96 wells (0030741030, Eppendorf, Hamburg,

973   Germany). From the FCS measurements of Alexa488, the τ_{diff} and sp were determined by

974   fitting with a single diffusion and blinking component. The diffusion coefficient (D) of

975   Alexa488 in aqueous solutions at 22.5 °C is 435 $\mu m^2 s^{-1}$ (Petrášek and Schwille, 2008). From

976   these parameters, the axial diameter can be determined with equation 4 and the volume can

977   be approximated by a cylinder (equation 5). This allows for transformation of particle

978   numbers to concentrations (equation 5) and diffusion times to diffusion coefficients (equation

979   4) that are independent of measurement settings and small daily changes in alignment of the

980   microscope.

$$N_{corr} = N_{apa} * \left[1 - \frac{I_{autofluorescence}}{I_{total}}\right]^2 * \left[\frac{I_{start}}{I_{ana}}\right] \qquad \text{Eq. 3}$$

$$\tau_{diff} = \frac{\omega_{xy}^2}{4D} \qquad \text{Eq. 4}$$

$$V = 2\pi\omega_{xy}^3 * sp \qquad \text{Eq. 5}$$

$$C = \frac{N_{corr}}{V * N_A} \qquad \text{Eq. 6}$$

981   The model to fit SGFP2-CTNNB1 measurements contained 2 diffusion components. The first

982   diffusion component was fixed to the speed of monomeric SGFP2-CTNNB1. To estimate the

983   speed of monomeric SGFP2-CTNNB1, the speed of free floating SGFP2, transfected in HAP1

984   cells, was measured to be 24.1 $\mu m^2 s^{-1}$ using FCS. Subsequently, this speed was used to

985   calculate the speed of monomeric SGFP2-CTNNB1 with Einstein-Stokes formula (Equation 7).

986   As the temperature (T), dynamic viscosity (η) and Boltzmann's constant (k_B) are equal

987   between SGFP2 and SGFP2-CTNNB1 measurements, the expected difference in diffusion

988   speed is only caused by the radius (r) of the diffusing molecule assuming a spherical protein.

989   The difference in radius was approximated by the cubic root of the ratio of the molecular

990   weight of the SGFP2-CTNNB1 fusion protein (88 + 27=115 kDa) and the size of the SGFP2

991   protein (27 kDa), thus expecting a 1.62 times lower diffusion coefficient (compared to free

992   floating SGFP2) of 14.9 $\mu m^2 s^{-1}$ for SGFP2-CTNNB1. It must be noted that, especially for larger

993   protein complexes, the linearity between the radius of the protein and the speed is not

994   ensured, if the shape is not globular, and due to other factors such as molecular crowding in

995   the cell and hindrance from the cytoskeletal network. We therefore did not estimate the size

996   of the measured CTNNB1 complexes, but rather compared them to measurements from other

997   FCS studies.

$$D = \frac{k_B T}{6\pi\eta r}$$
Eq. 7

998   In the fitting model, the structural parameter was fixed to the one determined by the

999   Alexa488 measurements of that day. To ensure good fitting, limits were set for other

1000   parameters; G_∞ [0.5-1.5], N [0.001, 500], τ_{trip} [$1*10^{-6}$-0.05 ms], τ_{diff2} [10-150 ms]. This model

1001   was able to fit most Autocorrelation Curves from FCS measurements. In case of clear misfits,

1002   as judged by the distribution of residuals around the fitted curves, the measurement was

1003   excluded (see supplementary file 1 – tab FCS measurements and fitting).

1004   N&B data acquisition and analysis

1005   For N&B analysis, 50 images were acquired per measurement with a pixel time of 100 µs/pixel

1006   and a pixel size of 0.138-0.207 µm. The fluorescent signal was acquired with the APD

1007   described above for the FCS measurements. As a control and to optimize acquisition settings,

1008   HAP1 cells transfected with SGFP2, EGFP monomer, dimer or trimer were measured alongside

1009   HAP1$^{SGFP2-CTNNB1}$ cells treated with BSA, WNT3A, DMSO or CHIR99021, or HAP1$^{SGFP2-CTNNB1(S45F)}$

1010   cells. APD readout was converted to a TIF stack using a custom build *.ptu* converter (Crosby

1011   et al., 2013). This TIF stack was further analyzed using an ImageJ macro script (modified from

1012   (Crosby et al., 2013), made available at https://osf.io/ys5qw/) based on Digman, Dalal,

1013   Horwitz, & Gratton, 2008. Within the script, average brightness and particle numbers were

1014   calculated for nuclear or cytoplasmic ROIs, which were set based on transmission image (see

1015   Figure 5F). Static or slow-moving particles, including membrane regions, were excluded by

1016   thresholding and/or ROI selection, since they can severely impact the brightness measured.

1017   Data were further analyzed in R/RStudio. Brightness was normalized to the median value of

1018   the EGFP-monomer brightness measured on the same day in the same cellular compartment

1019   (nucleus/cytoplasm). Our FCS and N&B analysis assume a different confocal volume. In FCS

1020   we assume a cylinder with factor $\gamma=1$, whereas in N&B we assume a 3D-Gauss with factor

1021 $\gamma=0.3536$. To be able to compare particle numbers obtained with both techniques, particle

1022   numbers obtained with N&B were divided by the factor $\gamma=0.3536$.

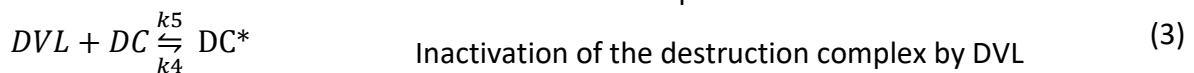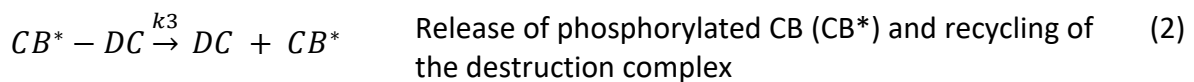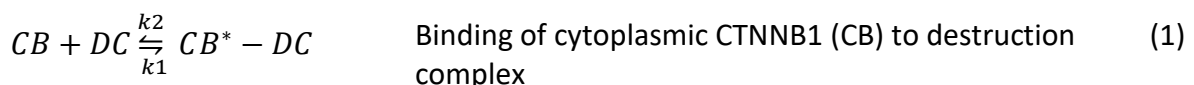1023   Data representation and statistical analysis

1024   Data processing and representation were performed in RStudio (version 1.1.456 running R

1025   3.5.1 or 3.6.1). 95% confidence intervals of the median mentioned in the text and shown in

1026   Table 1-2 and Supplementary file 1 were calculated using PlotsOfDifferences (Goedhart,

51

1027   2019). The P-values in Table 3 and Supplementary file 1 were also calculated using

1028   PlotsOfDifferences, which uses a randomization test and makes no assumption about the

1029   distribution of the data. Representation of the imaging data in Figure 4 supplement 2 and in

1030   supplementary movies 3-4 were generated in RStudio using a script based on

1031   PlotsOfDifferences (made available at https://osf.io/sxakf/).

1032   Model description

1033   We developed a minimal model for WNT signaling based on a previous model from the

1034   Kirschner group (Lee et al., 2003). The model is available as an interactive app at

1035   https://wntlab.shinyapps.io/WNT_minimal_model/ and the R source code of the model is

1036   available at https://osf.io/jx29z/ (WNT_minimal_model_v2.3.R).

1037   Our minimal model comprises the following reactions:

$$CB + DC \underset{k1}{\overset{k2}{\rightleftharpoons}} CB^* - DC$$ Binding of cytoplasmic CTNNB1 (CB) to destruction complex   (1)

$$CB^* - DC \overset{k3}{\rightarrow} DC + CB^*$$ Release of phosphorylated CB (CB*) and recycling of the destruction complex   (2)

$$DVL + DC \underset{k4}{\overset{k5}{\rightleftharpoons}} DC^*$$ Inactivation of the destruction complex by DVL   (3)

$$CB \underset{k6}{\overset{k7}{\rightleftharpoons}} NB$$ Nucleocytoplasmic shuttling of CB to and from the nucleus   (4)

$$NB + TCF \underset{k8}{\overset{k9}{\rightleftharpoons}} NB - TCF$$ Binding of NB to TCF   (5)
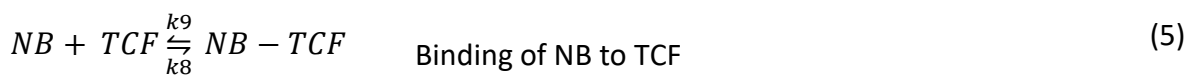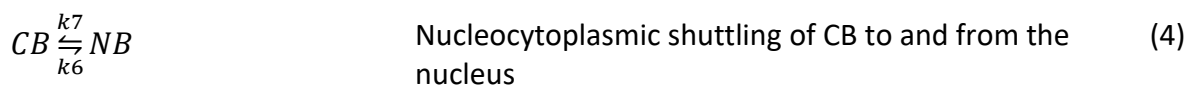
1038   Below, we show the differential equations that govern the concentrations of the different

1039   compounds over time for the reactions described above. Table 4 in the main text gives the

1040   correspondence between the variables (i.e. x_1) in the differential equations and the model

1041   name (i.e. CB) in the reactions. The parameter w in equations (7) and (8) is $w = 0$ in the

1042   absence of WNT and $w = 1$ if WNT is present, i.e. in our minimal model the inactive form of

52

1043   the destruction complex (DC*) is only present if WNT is present. The parameter b in equation

1044   (6) represents the constant production of CTNNB1, corresponding to v_{12} in Lee et al., 2003.

$$\frac{dx_1}{dt} = -k_1 x_1 x_2 + k_2 x_3 - k_6 x_1 + k_7 x_5 + b \tag{6}$$

$$\frac{dx_2}{dt} = -k_1 x_1 x_2 + (k_2 + k_3) x_3 - w(k_4 x_2 - k_5 x_4) \tag{7}$$

$$\frac{dx_3}{dt} = k_1 x_1 x_2 - (k_2 + k_3) x_3 \tag{8}$$

$$\frac{dx_4}{dt} = w(k_4 x_2 - k_5 x_4) \tag{9}$$

$$\frac{dx_5}{dt} = k_6 x_1 - k_7 x_5 - k_8 x_5 x_6 + k_9 x_7 \tag{10}$$

$$\frac{dx_6}{dt} = -k_8 x_5 x_6 + k_9 x_7 \tag{11}$$

$$\frac{dx_7}{dt} = k_8 x_5 x_6 - k_9 x_7 \tag{12}$$

1045

Equilibrium conditions without WNT

1046

1047   The parameters in our model can in part be determined from our measurements of the

1048   equilibrium concentrations of CB, NB and their complexes, see Table 4-5 in the main text.

1049   Where we could not determine the parameters from our measurements, we used published

1050   values as indicated.

1051   Under equilibrium conditions, the concentrations of the compounds do not change with time

1052   and the left-hand side of equations (6) - (12) is zero. From equations (10) and (11) we can

1053   determine the ratio of the rate constants k_6 and k_7 from the measured values of x_1 and x_5:

$$k_6 x_1 = k_7 x_5 \Leftrightarrow \frac{k_6}{k_7} = \frac{x_5}{x_1} = \frac{87}{91} = 0.96 \tag{13}$$

1054

53

1055   From equations (6), (8), (10) and (11) we have:

$$-k_3 x_3 + b = 0 \Leftrightarrow k_3 = \frac{b}{x_3} = \frac{0.423}{62.5} = 0.0068 \text{ min}^{-1} \tag{14}$$

1056   Our reaction (1) corresponds closely to step 8 in Lee et al. therefore, we use the value of the

1057   dissociation constant $K_8 = 120$ nM from Lee et al. for our dissociation constant $K_1 = \frac{k_2}{k_1}$.

1058   The concentration of the destruction complex is obtained from equation (1) under

1059   equilibrium conditions using equations (6), (8), (10), (11) and (14)

1060 $-k_1 x_1 x_2 + k_2 x_3 + b = 0$

1061   The value of b is assumed to be small compared to the two other terms, so we calculate the

1062   concentration of the destruction complex as:

1063 $x_2 = K_1 \frac{x_3}{x_1} = 120 \frac{62.5}{91} = 82.4$ nM. It was then verified in our interactive app that this value

1064   for the destruction complex is indeed consistent with the equilibrium conditions without WNT

1065   stimulation.

1066   To calculate the dissociation constant for the NB-TCF complex, we estimate an equilibrium

1067   concentration for free TCF (x_6) from Tan et al. (2012). From their Figure 11 it is seen that the

1068   bound TCF concentration in equilibrium in the presence of WNT has about the same value as

1069   the initial free TCF concentration and that no initial bound TCF is present. However, we

1070   measured NB-TCF also in the initial state. Therefore, we consider the free TCF concentration

1071   value from Tan et al. as a lower bound for the estimate of total TCF. Also, from Figure 11 of

1072   Tan et al. (2012) we estimate that of the initial free TCF, a fifth remains in the nucleus as free

1073   TCF after WNT is turned on. We measured 86 nM NB-TCF in the nucleus after the application

1074   of WNT. This leads to an estimate of the total concentration of TCF, TCF^0, in the nucleus of:

54

1075 $[TCF^0] = 86 + 0.2 \times 86 = 103$ nM. If we assume that the total TCF concentration does

1076   not change by the application of WNT, we calculate the dissociation constant of the NB-TCF

1077   complex from equation (12):

$$k_8 x_5 (TCF^0 - x_7) = k_9 x_7 \Rightarrow \frac{k_9}{k_8} = K_2 = \frac{x_5(TCF^0 - x_7)}{x_7} = \frac{87*81}{22} = 320 \text{ nM} \qquad (15)$$

1078

1079   Equilibrium conditions with WNT

1080   We model the action of WNT by deactivation of the destruction complex by DVL through

1081   reaction 3 by setting $w = 1$ in equations (7) and (9). The dissociation constant of CB*-DC, K_1,

1082   is assumed not to change in the presence of WNT. The measurements of free CB and NB in

1083   equilibrium (see Table 2) give for the ratio of k_6 and k_7:

$$k_6 x_1 = k_7 x_5 \Leftrightarrow \frac{k_6}{k_7} = \frac{x_5}{x_1} = \frac{170}{145} = 1.17 \qquad (16)$$

1084   The value of the rate of decay of the phosphorylated complex CB*-DC, k_3, is found to be the

1085   same for the "without WNT" situation:

$$-k_3 x_3 + b = 0 \Leftrightarrow k_3 = \frac{b}{x_3} = \frac{0.423}{62.5} = 0.0068 \text{ min}^{-1} \qquad (17)$$

1086   To uniquely determine the ratio of k_4 and k_5, we need the concentrations of the destruction

1087   complex DC and DC* neither of which we have access to. We can, however, fit this ratio with

1088   our model to the measured values of x_1 and x_7 and find $k_4/k_5 = 1.7$.

1089   We again calculate the dissociation constant of the NB-TCF complex from equation (12), using

1090   the concentrations for NB and NB-TCF obtained with FCS.

$$k_8 x_5 (TCF^0 - x_7) = k_9 x_7 \Rightarrow \frac{k_9}{k_8} = K_2 = \frac{x_5(TCF^0 - x_7)}{x_7} = \frac{170*17}{86} = 33.6 \text{ nM} \qquad (18)$$

1091   Notice that we determined the ratios of the rate constants from the measured equilibrium

1092   values of free and bound CTNNB1 in the cytoplasm and the nucleus. This means that our rate

1093   constants are determined up to a multiplicative factor: the equilibrium equations do not

1094   change if all rate constants k_i and the parameter b are multiplied by the same factor, $Rate$.

1095   The factor $Rate$ determines how fast our model system reaches equilibrium. By comparing

1096   the times equilibrium was reached by the cytoplasmic and nuclear SGFP2-CTNNB1 signals

1097   (Figure 4 C, D) of about 4.5 hours, we fitted a factor $Rate = 20$ for our model.

1098   Our model shows that the ratios of k_6/k_7 and k_9/k_8 are different for the conditions without

1099   and with WNT stimulation, suggesting a change in mechanism for nuclear shuttling of CTNNB1

1100   and nuclear retention of CTNNB1 in going from the WNT 'off' situation to the WNT 'on'

1101   situation. It seems likely that such changes do not occur instantaneously. In our model we

1102   therefore allow a gradual rise in k_5/k_4 and a gradual transition of the ratios of k_6/k_7 and

1103 k_9/k_8 from WNT 'off' to the WNT 'on'. In our model this is included by setting a parameter

1104   ("Steep") that indicates the time after application of WNT the transition from WNT 'off'

1105   parameter values to WNT 'on' parameter values is complete. The value that gives a good

1106   approximation of the experimentally observed concentration curves is *Steep =150* minutes

1107   (Figure 6 panels B-F).

Acknowledgements

Figure supplements

Figure 1 - supplement 1: FACS Gating strategy for haploid HAP1 cells.

Figure 1 - supplement 2: *SGFP2-CTNNB1* locus

Figure 2 - supplement 1: Verification of the WNT/CTNNB1 responsiveness of HAP1 cells.

Figure 3 - supplement 1: Verification of imaging results with WNT3A three independent HAP1[SGFP2-CTNNB1] clones.

Figure 3 - supplement 2: Difference analysis of SGFP2-CTNNB1 fluorescence.

Figure 3 supplement 3: Unnormalized nuclear and cytoplasmic intensity measurements.

Figure 5 - supplement 1: Quantification of SGFP2-CTNNB1 particles, fluorescence and fluorescence lifetime.

Figure 5 supplement 2: Number and Brightness analysis

Figure 7 supplement 1 Generation and characterization of a S45F mutant cell line (HAP1[SGFP2-CTNNB1(S45F)]).

Figure 8 supplement 1 Live imaging of HAP1[SGFP2-CTNNB1] upon CHIR99021 stimulation.

Figure 8 supplement 2 additional biophysical properties of SGFP2-CTNNB1[S45F] and SGFP2-CTNNB1 under CHIR99021 stimulation.

Figure 1 – supplement 1: FACS Gating strategy for haploid HAP1 cells. A-C) Single-cell gating based on forward scatter (FSC) and side scatter (SSC). D) Live cell gating based on DAPI exclusion. E-F) Haploid cell sorting based on Vibrant live-cell DNA dye. E) Haploid cell cycle profile. Only cells in G1 can be confidently identified as haploid (1n). The second peak contains both G2/M haploid cells, as well as diploid (2n) and polyploid events. Of note, the depicted HAP1[WT] population is mainly haploid. F) Back-gating of the haploid G1 population from E onto the forward and side scatter plot. A stringent gate is set based on cell size to ensure only G1 (1n) cells qualify for sorting.

58
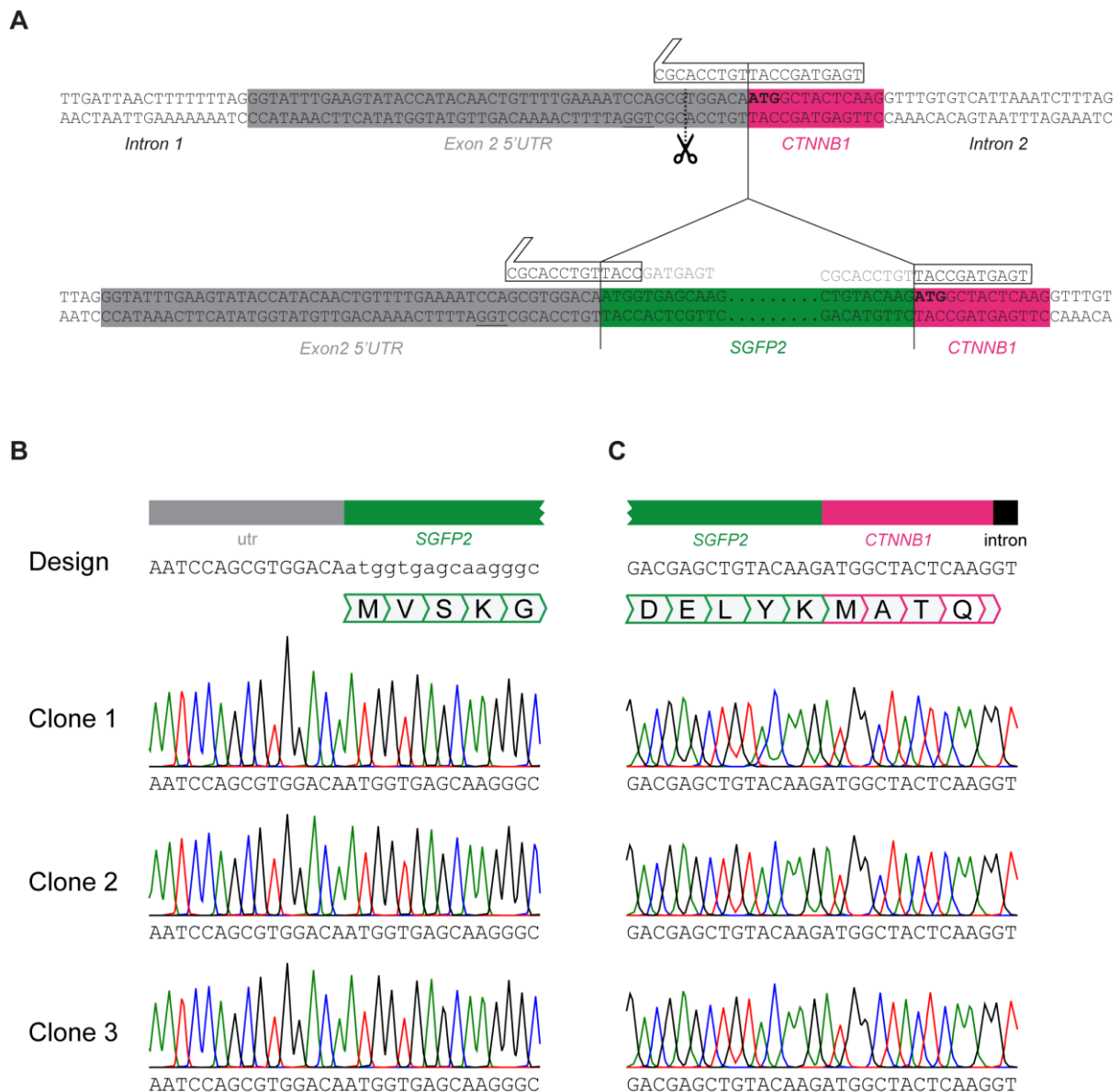
Figure 1 – supplement 2: *SGFP2-CTNNB1* locus A) Detailed view of *CTNNB1* exon 2 depicting gRNA design relative to the wildtype (top) and repaired (bottom) CTNNB1 allele. Note that the repair template contains the same sequence as the repaired allele depicted here. CTNNB1 sequences are shown in capital letters, SGFP2 sequences shown in lowercase. 5' UTR, *SGFP2* and *CTNNB1* and intron regions are indicated below the colored boxes. The gRNA (white arrow box above sequence) overlaps the start codon (depicted in bold), resulting in a Cas9-mediated double-strand break in the 5'UTR (predicted cut site indicated by dotted line and scissor, PAM site underlined). After successful homologous recombination, most of the gRNA binding site is destroyed, thus minimizing the chance of cutting the repair template or re-cutting the repaired allele. PCR based screening confirmed that 22/23 single-cell sorted clones indeed showed an integration of the expected size at the CTNNB1 locus. Complete sequence coverage of the insertion site in exon 2 was obtained for 9/11 sequenced clones, of which 8 showed the desired repair, and 1 clone showed an additional point mutation in the repaired locus. B-C) Sequencing of three independent HAP1[SGFP2-CTNNB1] clones on the 5' (B) and the 3' (C) end of *SGFP2* integration in exon 2 of *CTNNB1*. Sanger sequencing of the endogenous *CTNNB1* locus of clone 1, clone 2 and clone 3 shows an exact match to the design and thus correct homology directed repair.
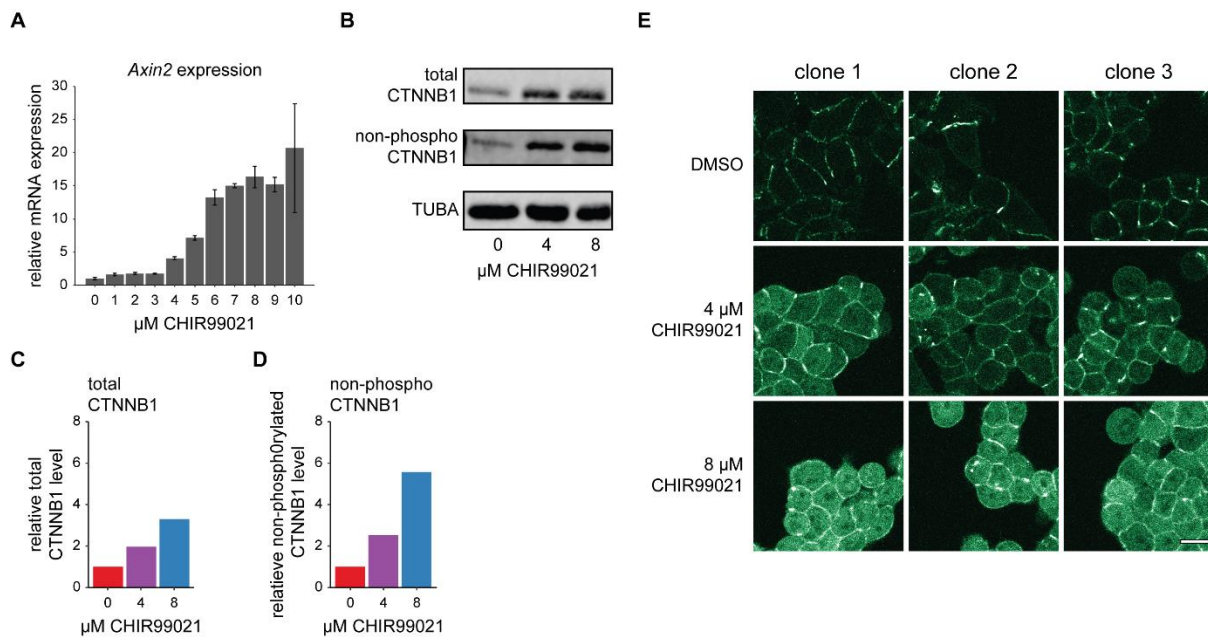
Figure 2 supplement 1: Verification of the WNT/CTNNB1 responsiveness of HAP1 cells. A) Graph depicting *AXIN2* qRT-PCR results from HAP1[WT] cells treated with the indicated range of CHIR99021 (1-10 μM) or DMSO vehicle control (0 μM) for 24 hours. *HPRT* was used as a reference gene. Error bars represent standard deviation within technical triplicates from n=1 biological experiment. Based on this, we selected 4uM and 8 μM as intermediate and high levels of WNT/CTNNB1 pathway induction for follow up experiments. B) Western blot, showing the increase in total (top) and non-phosphorylated (i.e. active) CTNNB1 levels (middle) in response to pathway stimulation. HAP1[WT] cells were treated for 24 hours with 4 or 8 μM CHIR99021, or DMSO vehicle control (0 μM). Alpha-Tubulin (TUBA, bottom) serves as a loading control. C-D) Quantification of the western blot from (B) depicting the relative fold change of total CTNNB1 (C) or non-phosphorylated CTNNB1 (D) to DMSO control corrected for Tubulin loading. E) Representative confocal microscopy images of three independent HAP1[SGFP2-CTNNB1] clones, treated for 24 hours with 4 or 8 μM CHIR99021, or DMSO vehicle control. Scalebar is 10 μm.
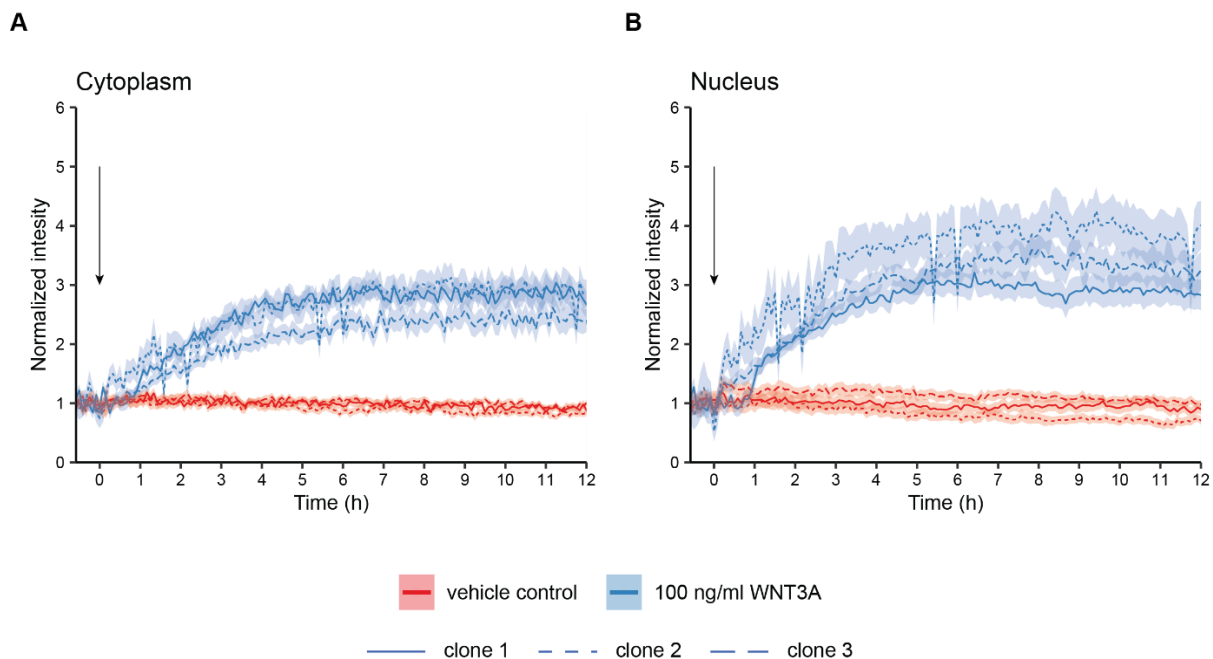

Figure 3 supplement 1: Graphs showing quantification of time-lapse microscopy experiments with three independent HAP1[SGFP2-CTNNB1] clones. Stills of this experiment are shown in Figure 3C. Segmentation was performed as described in Figure 4. Arrow indicates the moment of starting the different treatments (BSA in red or 100 ng/ml WNT3A in blue). Solid lines represent the mean normalized intensity and shading the 95% confidence interval in the cytoplasm (A) or nucleus (B). Line pattern indicates the three different clones. n=13-158 cells for each condition and time point for n=1 biological experiment.
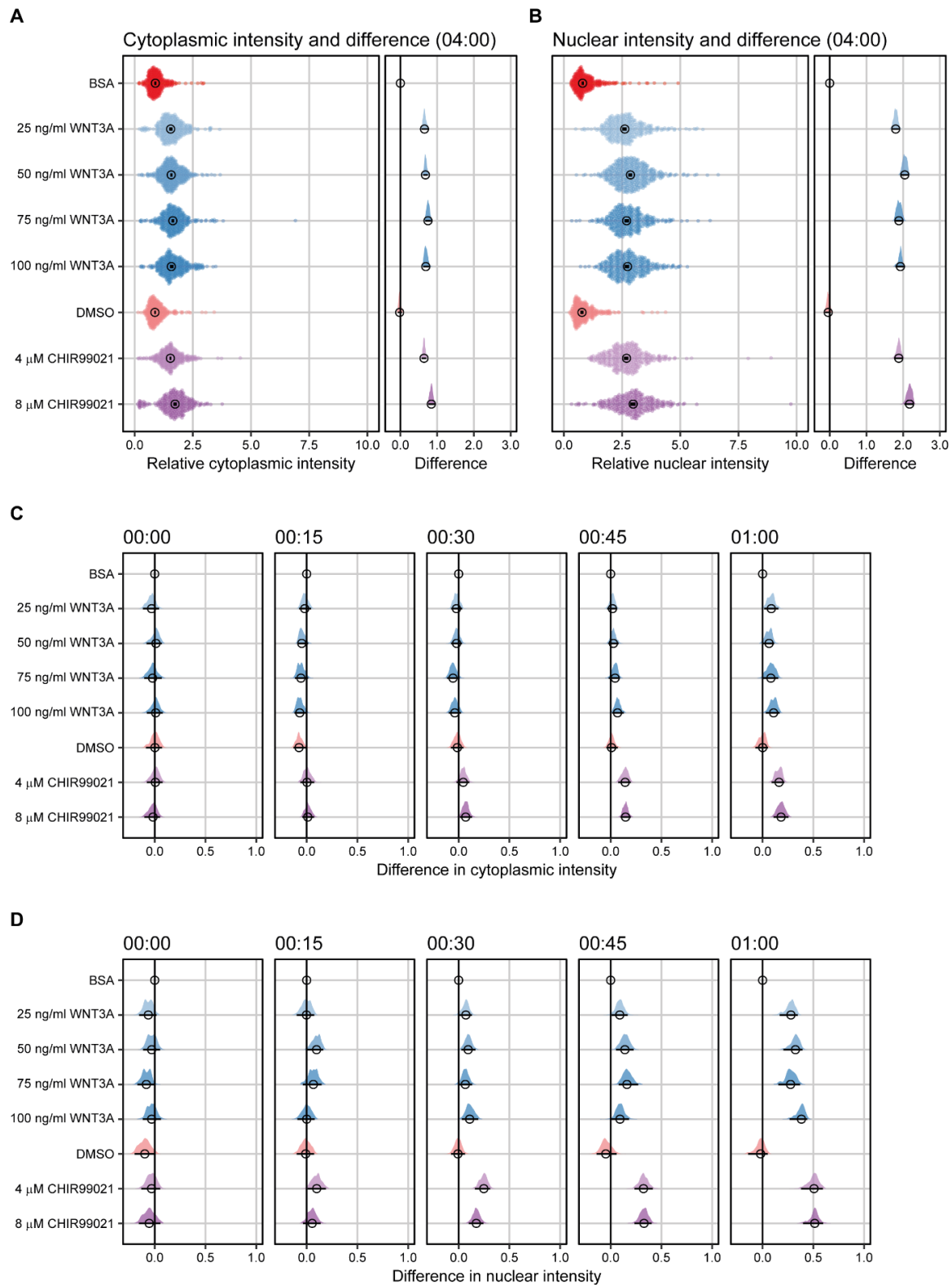
Figure 3 supplement 2: Difference analysis of SGFP2-CTNNB1 fluorescence. A-B) Plots depicting the relative intensity (left) and the difference in relative intensity to BSA treated cells (right) in the cytoplasm (A) and nucleus (B) after 4 hours of treatment. Circles indicate the median value and bars indicate the 95% CI. In the relative intensity plot (left) the distribution is built from individual data points in a violin-type fashion to faithfully represent the distribution of data. In the difference plot (right) the distribution of differences is represented in a half violin plot. If the 95% CI in the difference plot does not overlap the zero line, which indicates no difference, the sample is significantly different from BSA control condition. C-D) Plots depicting the difference in relative intensity in the cytoplasm (C) and nucleus (D) between the moment of addition and 1 hour of treatment. Titles indicate the time (hh:mm). The distribution of differences is represented in a half violin plot. Circles indicate the median value and bars indicate the 95% CI. If the 95% CI does not overlap the zero line, which indicates no difference, the sample is significantly different from the BSA control condition.
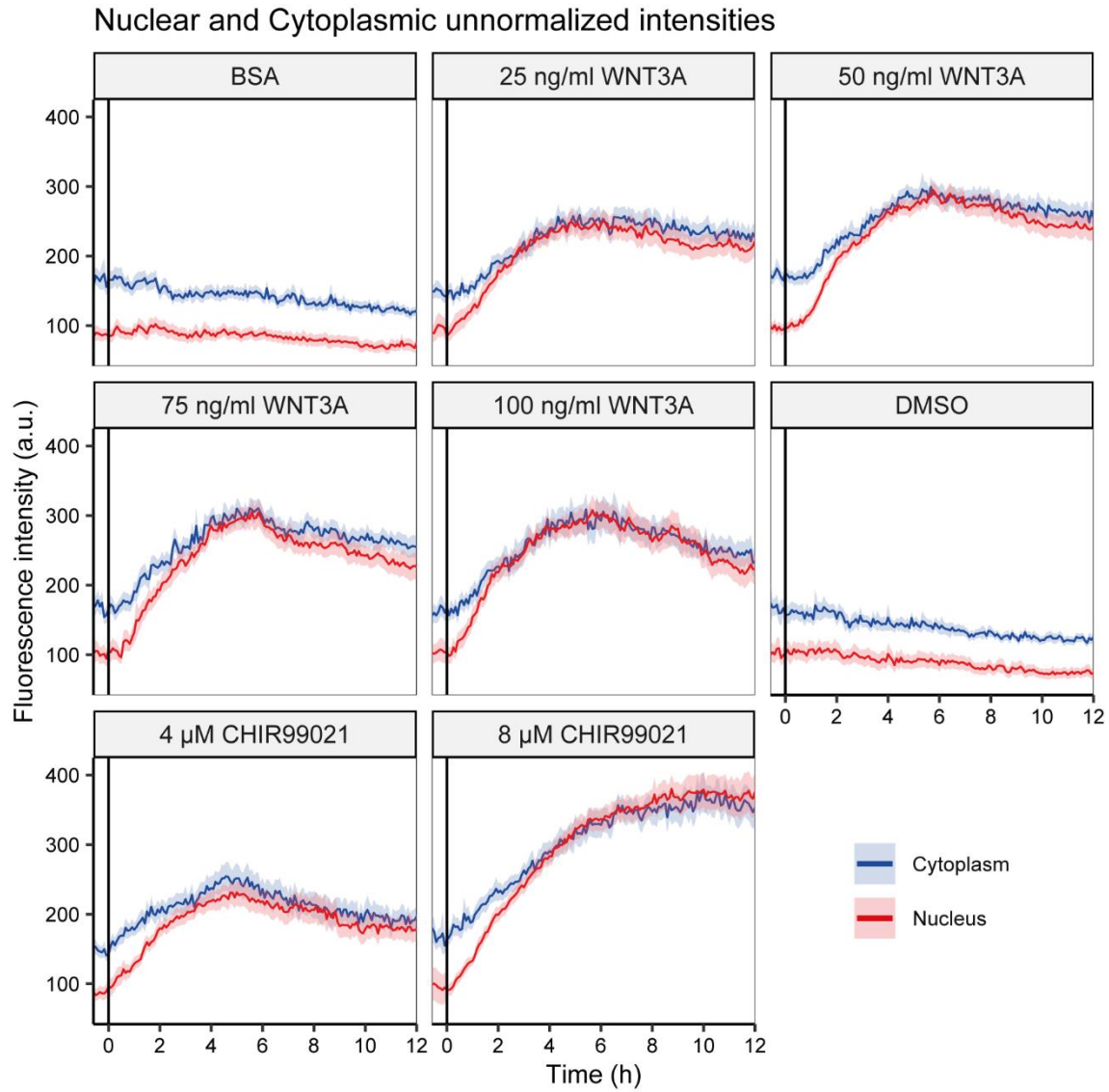
61

Figure 3 supplement 3: Unnormalized nuclear and cytoplasmic intensity measurements. Graphs showing the unnormalized fluorescence intensities quantified for a single biological replicate shown in Figure 3. The vertical black lines indicate the moment of starting the different treatments (as indicated on top of each graph). Solid lines represent the mean normalized intensity and shading the 95% confidence interval in the cytoplasm (blue) or nucleus (red). n=64-148 cells for each condition and time point.
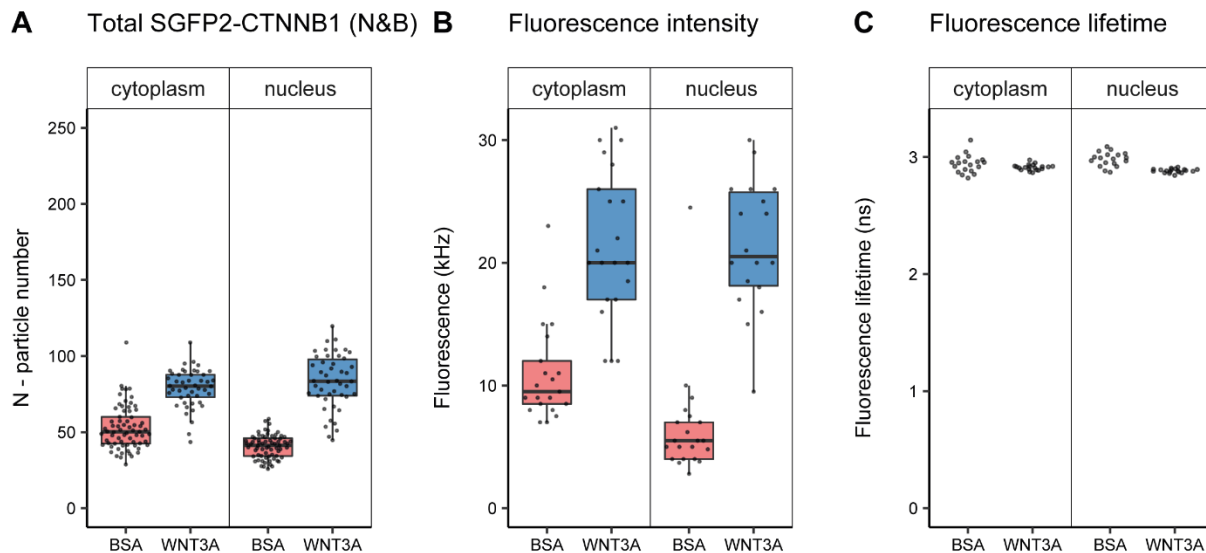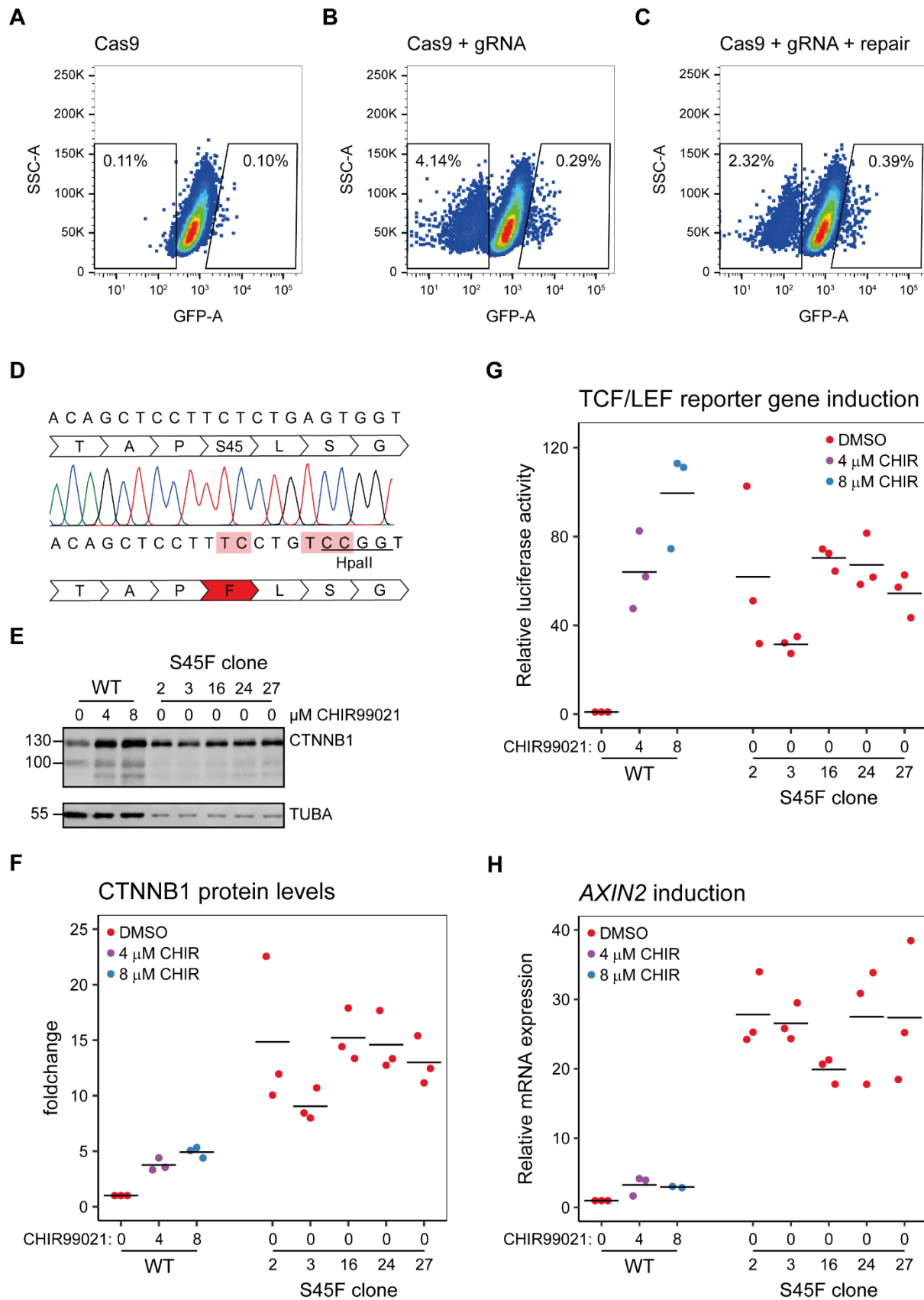
Figure 5 supplement 1 Quantification of SGFP2-CTNNB1 particles, fluorescence and fluorescence lifetime. Details on sample size and statistics can be found in supplementary file 1. A) Graph depicting the total number of SGFP2-CTNNB1 particles as measured with N&B. B) Graph depicting the average fluorescence intensity at the start of the FCS measurement. The increase in SGFP2-CTNNB1 fluorescence in the cytoplasm (2.1-fold) exceeds the increase in the SGFP2-CTNNB1 concentration (1.1-fold, Figure 5A), but does correspond to the relative increase measured by time-lapse imaging (1.7-fold, Figure 4C). C) Graph depicting fluorescence lifetimes calculated from the FCS measurements. The Fluorescence lifetime of SGFP2-CTNNB1 is independent of the subcellular compartment and treatment. Therefore, photophysical effects are not the cause for the difference between the fold-change in fluorescence and concentrations of the FCS measurements as described in (B).
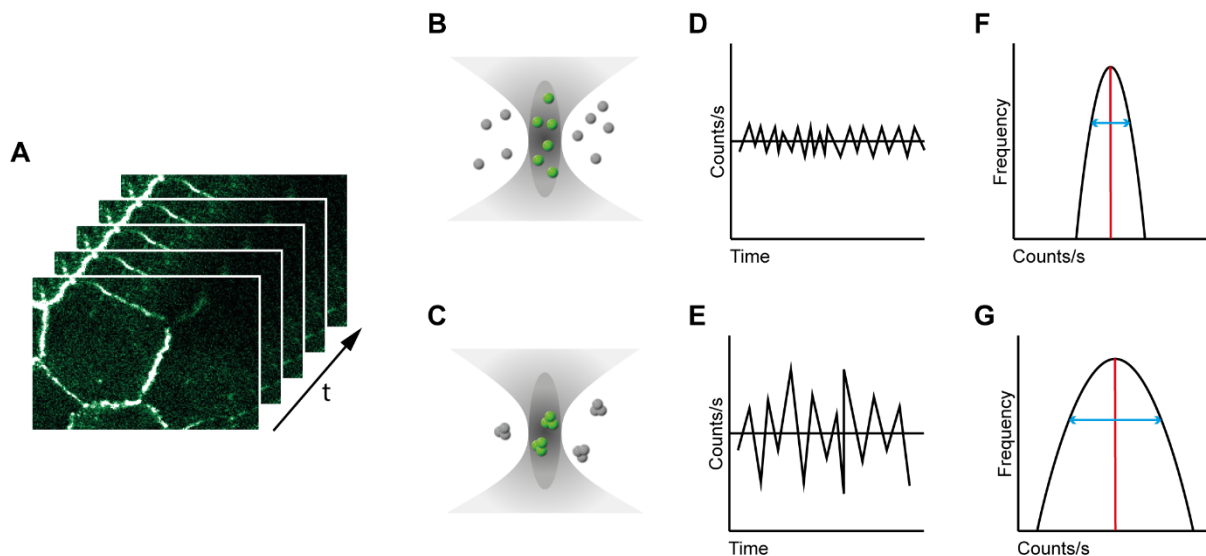
Figure 5 supplement 2: Number and Brightness analysis A) A series of images are acquired over time (t) B-C) Representation of the confocal volume in a single pixel of the image in (A) representing monomers with a brightness of 1 (B) and trimers with a brightness of 3 (C) both confocal volumes emit a fluorescence of 6. D-E) Graph depicting the variation in fluorescence, measured by an APD in counts/s, in a single pixel over time for the monomer (D) and trimer (E). With a higher brightness the variation around the average becomes larger. Note that the time-scale in N&B is much larger than in FCS (Figure 4 A-C) due to the use of images rather than a single point and therefore the variation is no longer dependent on diffusion kinetics. F-G) Graph depicting the distribution of fluorescence observed in a single pixel. The average (red line) in our case is the same for 6 monomers (F) or 2 trimers (G), but the standard deviation (blue line) is much larger for the trimer. The average and standard deviation are used to calculate the number

1201

1206   oligo repair, led to a reduction in the population with decreased SGFP2 fluorescence (representing cells repaired with NHEJ that resulted in
1207   a loss of the SGFP2-CTNNB1 fusion protein) and an increase in the population with increased SGFP2 fluorescence (representing cells repaired
1208   with NHEJ that resulted in a stabilizing SGPF2-CTNNB1 truncation, mutation, insertion or deletion as well as cells with the correct HDR
1209   resulting in the stabilizing S45F mutation). Cells with increased fluorescence were sorted as single haploid cells (see Figure 1 Supplement 1)
1210   and expanded for further analysis D) Graphical representation of part of the 3rd exon of SGFP2-CTNNB1 before (top) and after (bottom)
1211   CRISPR/Cas9-mediated mutagenesis. Sanger sequencing is shown for one correctly targeted clone. The mutation changes the 45th serine to
1212   a phenylalanine (S45F) and additionally removes the gRNA binding site and a silent mutation that introduces a HpaII restriction site for
1213   screening purposes. Mutated bases are indicated in light red. 14/32 single cell clones showed the expected genotyping fragment size and
1214   7/32 showed large insertions or deletions. 7/14 clones showed the expected genotyping band contained the HpaII restriction site, 3/14 did
1215   not. Sanger sequencing coverage for the exon3 locus was obtained for 6/7 clones and all showed correct targeting (as shown for 1 clone
1216   here). Five clones were further analyzed; Clone 2,3,16 and 24 are from one single transfection, clone 27 from an independent transfection.
1217   E) Western blot, showing SGFP2-CTNNB1^{WT} (WT) and SGFP2 CTNNB1^{S45F} (S45F clone) protein levels. All panels are from one blot that was
1218   cut at the 70 kDa mark. Top: HAP1$^{SGFP2-CTNNB1(WT)}$ and HAP1$^{SGFP2-CTNNB1(S45F)}$ clones express the SGFP2-CTNNB1 protein at the expected height.
1219   Bottom: alpha-Tubulin (TUBA) loading control. A representative image of n=3 independent experiments is shown. F) Quantification of
1220   Western blots from n=3 independent experiments, including the one in, normalized to the SGFP2-CTNNB1^{WT} control (E), showing that the
1221   S45F clones express higher levels of SGFP2-CTNNB1 than their HAP1$^{SGFP2-CTNNB1(WT)}$ parental line, even after 24h treatment with 8μM
1222   CHIR99021. Horizontal bar indicates the mean. G) Graph depicting the results from a MegaTopflash dual luciferase reporter assay, showing
1223   increased levels of TCF/LEF reporter gene activation for and HAP1$^{SGFP2-CTNNB1(S45F)}$, comparable to HAP1$^{SGFP2-CTNNB1(WT)}$ cells treated for 24 hours
1224   with 8μM CHIR99021 treatment. Data points from n=3 independent experiments are shown. Horizontal bar indicates the mean. Values are
1225   depicted relative to the DMSO control, which was set to 1 for each individual cell line. H)
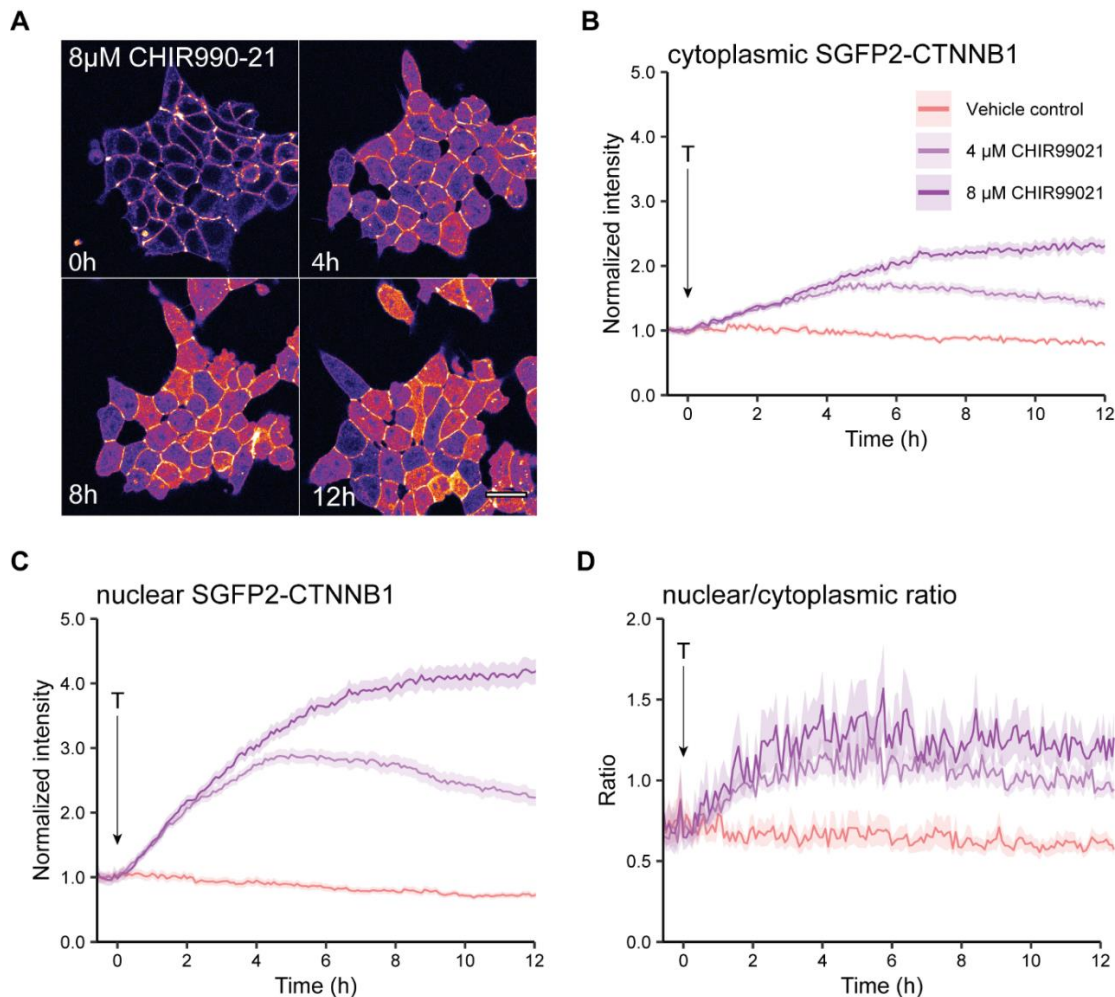
1226

1227   **Figure 8 supplement 1** Live imaging of HAP1$^{SGFP2-CTNNB1}$ upon CHIR99021 stimulation. A) Representative stills from confocal time-lapse
1228   experiments corresponding to Supplementary Movies 3, showing an increase of SGFP2-CTNNB1 after treatment with 8μM CHIR99021. Scale
1229   bar = 20 μm. B-D) Quantification of time-lapse microscopy series, using the segmentation pipeline shown in Figure 3E. Arrow indicates the
1230   moment of starting the different treatments (T, see legend in B for details). B-C) Graph depicting the normalized intensity of SGFP2-CTNNB1
1231   in the cytoplasm (B) or nucleus (C) over time. Solid lines represent the mean normalized fluorescence intensity and shading indicates the
1232   95% confidence interval. n=166-400 cells for each condition and time point, pooled data from n=3 independent biological experiments. D)
1233   Graph depicting the nuclear/cytoplasmic ratio of SGFP2-CTNNB1 over time, calculated from raw intensity values underlying (B) and (C). This
1234   experiment was recorded simulateously with the data shown in Figure 3. Additional data representation of this experiment is found in Figure
1235   3 supplement 2 and Supplementary movies 4-6.
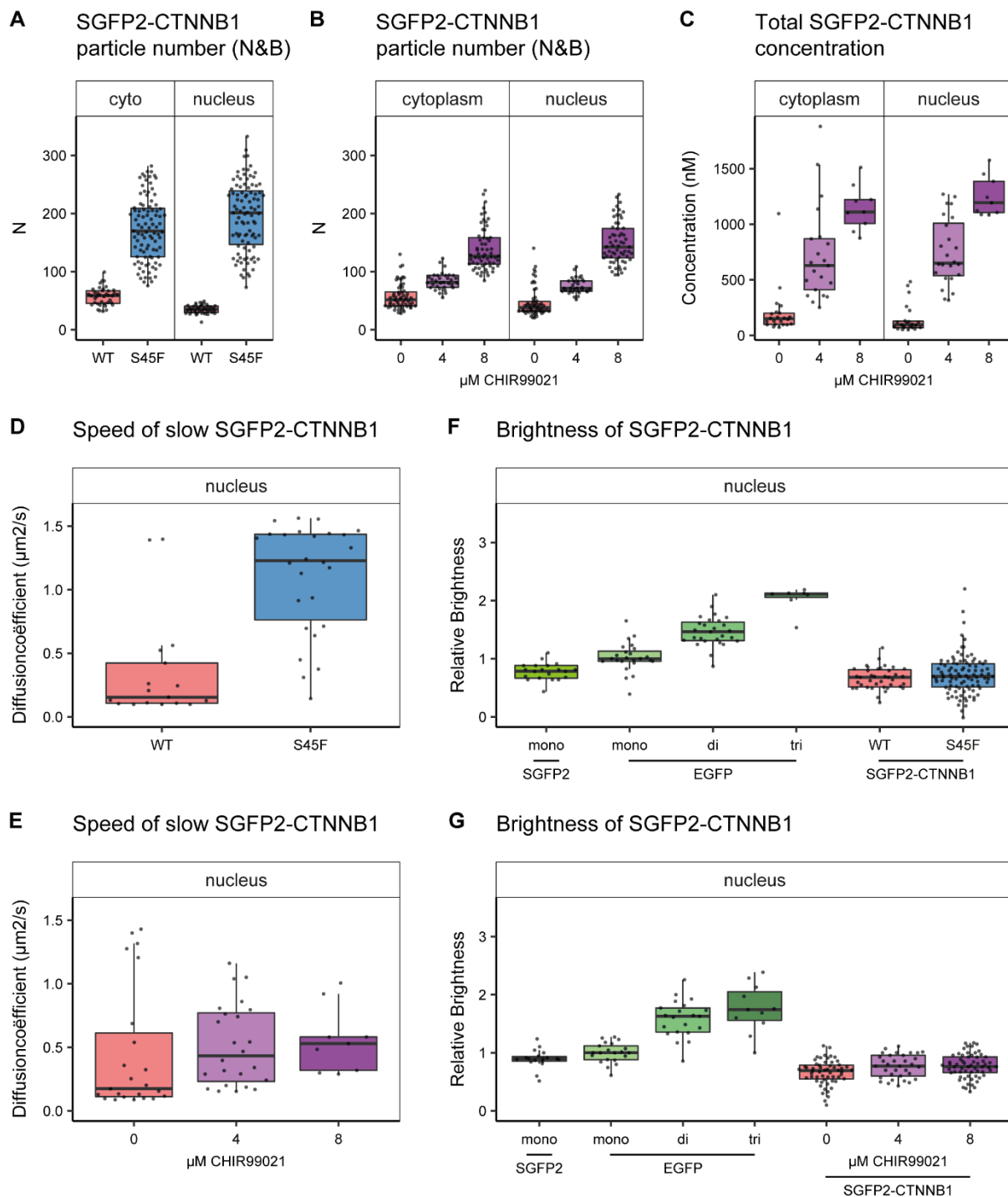
Figure 8 supplement 2 additional biophysical properties of SGFP2-CTNNB1^{S45F} and SGFP2-CTNNB1 under CHIR99021 stimulation. The S45F mutant was introduced using CRISPR (see Figure 7 supplement 1) and CHIR treated and control cells were measured after 24 hours. Details on sample size and statistics can be found in supplementary file 1. A-B) Graph depicting the total number of SGFP2-CTNNB1 particles as measured with N&B upon S45F mutation (A) or CHIR99021 stimulation (B). C) Graph depicting the total concentration of SGFP2-CTNNB1 particles (monomeric plus complexed) as measured with FCS upon CHIR99021 treatment. D-E) Graphs depicting the speed of the second diffusion component (i.e. SGFP2-CTNNB1 containing complex) in the nucleus measured by FCS for S45F mutant (D) or 24 hour CHIR99021 treatment (E). E-F) Graph depicting the molecular brightness of SGFP2-CTNNB1 in the nucleus relative to controls as measured with N&B. EGFP monomer was used for normalization and EGFP dimer and trimer as controls for N&B measurements.

66

Supplementary Movie legends

Supplementary Movie 1-3: Representative movies of confocal time-lapse experiments, showing SGFP2-CTNNB1 (left, green), SiR-DNA staining (middle, magenta) and transmission image (right, grey) after treatment with vehicle control (BSA) (**Supplementary Movie 1**), 100 ng/ml WNT3A (**Supplementary Movie 2**) or 8 μM CHIR99021 (**Supplementary Movie 3**). Time of addition is at 00:00:00 (indicated at the top left). Scale bar in the lower right represents 20μm.

Supplementary Movie 4-6: Movies showing the quantification of time-lapse microscopy series (from Figure 4 and Supplementary Movie 1-3) at each time point showing all individual cells from 3 biological experiments. Time of addition of the indicated substances is at 00:00:00 (indicated at the top left). The left graph represents the raw data (colored dots, each dot is one cell, n=155-400 cells for each condition and time point), the median (black circle) and the 95% CI of the median (black bar). The right graph represents the median difference (black circle) from the treatments to the control (BSA). When the 95% CI (black bar) does not overlap 0, the difference between the two conditions is significant.

Supplementary Movie 4: Quantification of the normalized intensity of SGFP2-CTNNB1 in the cytoplasm. Significant changes in intensity can first be observed after 40 minutes of 8 μM CHIR99021, and after 70-80 minutes of 4 μM CHIR99021 or 25-100ng/ml WNT3A treatment.

Supplementary Movie 5: Quantification of the normalized intensity of SGFP2-CTNNB1 in the nucleus. Significant changes in intensity can be observed for all treatments (but not controls) after 20-50 minutes.

Supplementary Movie 6: Quantification of the nuclear-cytoplasmic ratio of SGFP2-CTNNB1, calculated from raw intensity values underlying Supplementary Movies 4 and 5. Significant changes in the nuclear-cytoplasmic ratio can be observed for all treatments (but not controls) after 20-50 minutes.

Supplementary Files

Supplementary File 1: Tables of all summary statistics (mean, median, 95% confidence intervals, differences, p-values) of the FCS and N&B parameters show in Figure 5, 7 and 8 and accompanying supplements.

References

1274   Aberle, H., Bauer, A., Stappert, J., Kispert, A., and Kemler, R. (1997). β-catenin is a target for

1275   the ubiquitin-proteasome pathway. EMBO J. *16*, 3797–3804.

1276   Agajanian, M.J., Walker, M.P., Axtman, A.D., Ruela-de-Sousa, R.R., Serafin, D.S., Rabinowitz,

1277   A.D., Graham, D.M., Ryan, M.B., Tamir, T., Nakamichi, Y., et al. (2019). WNT Activates the

1278   AAK1 Kinase to Promote Clathrin-Mediated Endocytosis of LRP6 and Establish a Negative

1279   Feedback Loop. Cell Rep. *26*, 79-93.e8.

1280   Ambrosi, G., Voloshanenko, O., Eckert, A., Kranz, D., Nienhaus, G.U., and Boutros, M. (2020).

1281   Allele-specific endogenous tagging and quantitative analysis of β-catenin in colon cancer

1282   cells. BioRxiv.

1283   van Amerongen, R., and Nusse, R. (2009). Towards an integrated view of Wnt signaling in

1284   development. Development *136*, 3205–3214.

1285   van Amerongen, R., Bowman, A.N., and Nusse, R. (2012). Developmental stage and time

1286   dictate the fate of Wnt/β-catenin-responsive stem cells in the mammary gland. Cell Stem

1287   Cell *11*, 387–400.

1288   Amit, S., Hatzubai, A., Birman, Y., Andersen, J.S., Ben-shushan, E., Mann, M., Ben-neriah, Y.,

1289   and Alkalay, I. (2002). Axin-mediated CKI phosphorylation of β-catenin at Ser 45: a molecular

1290   switch for the Wnt pathway. Genes Dev. *16*, 1066–1076.

1291   Andersson, B.S., Beran, M., Pathak, S., Goodacre, A., Barlogie, B., and McCredie, K.B. (1987).

1292   Ph-positive chronic myeloid leukemia with near-haploid conversion in vivo and

1293   establishment of a continuously growing cell line with similar cytogenetic pattern. Cancer

1294   Genet. Cytogenet. *24*, 335–343.

1295   Armstrong, N.J., Fagotto, F., Prothmann, C., and Rupp, R.A.W. (2012). Maternal Wnt/β-

1296   catenin signaling coactivates transcription through NF-κB binding sites during xenopus axis

1297   formation. PLoS One *7*.

1298   Bain, J., Plater, L., Elliott, M., Shpiro, N., Hastie, C.J., Mclauchlan, H., Klevernic, I., Arthur,

1299   J.S.C., Alessi, D.R., and Cohen, P. (2007). The selectivity of protein kinase inhibitors: A further

1300   update. Biochem. J. *408*, 297–315.

1301   Barker, N., van Es, J.H., Kuipers, J., Kujala, P., van den Born, M., Cozijnsen, M., Haegebarth,

1302   A., Korving, J., Begthel, H., Peters, P.J., et al. (2007). Identification of stem cells in small

1303   intestine and colon by marker gene Lgr5. Nature *449*, 1003–1007.

1304   Behrens, J., von Kries, J.P., Kühl, M., Bruhn, L., Wedlich, D., Grosschedl, R., and Birchmeier,

1305   W. (1996). Functional interaction of beta-catenin with the transcription factor LEF-1. Nature

1306   *382*, 638–642.

1307   Bilic, J., Huang, Y.-L., Davidson, G., Zimmermann, T., Cruciat, C.-M.C.-M., Bienz, M., and

1308   Niehrs, C. (2007). Wnt induces LRP6 signalosomes and promotes dishevelled-dependent

1309   LRP6 phosphorylation. Science *316*, 1619–1622.

1310   Bindels, D.S., Haarbosch, L., van Weeren, L., Postma, M., Wiese, K.E., Mastop, M., Aumonier,

1311   S., Gotthard, G., Royant, A., Hink, M.A., et al. (2017). mScarlet: a bright monomeric red

1312   fluorescent protein for cellular imaging. Nat. Methods *14*, 53–56.

1313   Bugter, J.M., Fenderico, N., and Maurice, M.M. (2020). Mutations and mechanisms of WNT

1314   pathway tumour suppressors in cancer. Nat. Rev. Cancer.

1315   Canaj, H., Hussmann, J.A., Li, H., Beckman, K.A., Goodrich, L., Cho, Nathan, H., Li, Y.J., Santos,

1316   D.A., McGeever, A., Stewart, E.M., et al. (2019). Deep profiling reveals substantial

69

1317   heterogeneity of integration outcomes in CRISPR knock-in experiments. BioRxiv.

1318   Cantù, C., Felker, A., Zimmerli, D., Prummel, K.D., Cabello, E.M., Chiavacci, E., Méndez-

1319   Acevedo, K.M., Kirchgeorg, L., Burger, S., Ripoll, J., et al. (2018). Mutations in Bcl9 and Pygo

1320   genes cause congenital heart defects by tissue-specific perturbation of Wnt/β-catenin

1321   signaling. Genes Dev. *32*, 1443–1458.

1322   Carette, J.E., Raaben, M., Wong, A.C., Herbert, A.S., Obernosterer, G., Mulherkar, N.,

1323   Kuehne, A.I., Kranzusch, P.J., Griffin, A.M., Ruthel, G., et al. (2011). Ebola virus entry requires

1324   the cholesterol transporter Niemann-Pick C1. Nature *477*, 340–343.

1325   Chhabra, S., Liu, L., Goh, R., Kong, X., and Warmflash, A. (2019). Dissecting the dynamics of

1326   signaling events in the BMP, WNT, and NODAL cascade during self-organized fate patterning

1327   in human gastruloids. PLOS Biol. *17*, e3000498.

1328   Crosby, K.C., Postma, M., Hink, M.A., Zeelenberg, C.H.C., Adjobo-Hermans, M.J.W., and

1329   Gadella, T.W.J. (2013). Quantitative analysis of self-association and mobility of Annexin A4

1330   at the plasma membrane. Biophys. J. *104*, 1875–1885.

1331   Digman, M.A., Dalal, R., Horwitz, A.F., and Gratton, E. (2008). Mapping the number of

1332   molecules and brightness in the laser scanning microscope. Biophys. J. *94*, 2320–2332.

1333   Doumpas, N., Lampart, F., Robinson, M.D., Lentini, A., Nestor, C.E., Cantù, C., and Basler, K.

1334   (2019). TCF / LEF dependent and independent transcriptional regulation of Wnt/β-catenin

1335   target genes . EMBO J. *38*, 1–14.

1336   Dross, N., Spriet, C., Zwerger, M., Müller, G., Waldeck, W., and Langowski, J. (2009).

1337   Mapping eGFP oligomer mobility in living cell nuclei. PLoS One *4*, 1–13.

1338   Eckert, A.F., Gao, P., Wesslowski, J., Wang, X., Rath, J., Nienhaus, K., Davidson, G., and

1339   Nienhaus, G.U. (2020). Measuring ligand-cell surface receptor affinities with axial line-

1340   scanning fluorescence correlation spectroscopy. Elife *9*.

1341   Elson, E.L. (2011). Fluorescence correlation spectroscopy: Past, present, future. Biophys. J.

1342   *101*, 2855–2870.

1343   Essers, M.A.G.G., De Vries-Smits, L.M.M.M., Barker, N., Polderman, P.E., Burgering, B.M.T.T.,

1344   and Korswagen, H.C. (2005). Functional interaction between β-catenin and FOXO in

1345   oxidative stress signaling. Science (80-.). *308*, 1181–1184.

1346   Essletzbichler, P., Konopka, T., Santoro, F., Chen, D., Gapp, B. V., Kralovics, R.,

1347   Brummelkamp, T.R., Nijman, S.M.B., and Bürckstümmer, T. (2014). Megabase-scale deletion

1348   using CRISPR/Cas9 to generate a fully haploid human cell line. Genome Res. *24*, 2059–2065.

1349   Fagotto, F., Glück, U., and Gumbiner, B.M. (1998). Nuclear localization signal-independent

1350   and importin/karyopherin-independent nuclear import of β-catenin. Curr. Biol. *8*, 181–190.

1351   Fagotto, F., Jho, E.H., Zeng, L., Kurth, T., Joos, T., Kaufmann, C., and Costantini, F. (1999).

1352   Domains of Axin involved in protein-protein interactions, Wnt pathway inhibition, and

1353   intracellular localization. J. Cell Biol. *145*, 741–756.

1354   Faux, M.C., Coates, J.L., Catimel, B., Cody, S., Clayton, A.H.A., Layton, M.J., and Burgess, A.W.

1355   (2008). Recruitment of adenomatous polyposis coli and beta-catenin to axin-puncta.

1356   Oncogene *27*, 5808–5820.

1357   Fiedler, M., Mendoza-Topaz, C., Rutherford, T.J., Mieszczanek, J., and Bienz, M. (2011).

1358   Dishevelled interacts with the DIX domain polymerization interface of Axin to interfere with

1359   its function in down-regulating β-catenin. Proc. Natl. Acad. Sci. U. S. A. *108*, 1937–1942.

1360   Fiedler, M., Graeb, M., Mieszczanek, J., Rutherford, T.J., Johnson, C.M., and Bienz, M.

1361   (2015). An ancient Pygo-dependent Wnt enhanceosome integrated by chip/LDB-SSDP. Elife

1362   *4*, 1–22.

1363   Franz, A., Shlyueva, D., Brunner, E., Stark, A., and Basler, K. (2017). Probing the canonicity of

1364   the Wnt/Wingless signaling pathway. PLoS Genet. *13*, 1–18.

1365   Fuerer, C., Nostro, M.C., and Constam, D.B. (2014). Nodal·Gdf1 heterodimers with bound

1366   prodomains enable serum-independent nodal signaling and endoderm differentiation. J.

1367   Biol. Chem. *289*, 17854–17871.

1368   Gammons, M., and Bienz, M. (2018). Multiprotein complexes governing Wnt signal

1369   transduction. Curr. Opin. Cell Biol. *51*, 42–49.

1370   Gerlach, J.P., Emmink, B.L., Nojima, H., Kranenburg, O., and Maurice, M.M. (2014). Wnt

1371   signalling induces accumulation of phosphorylated β-catenin in two distinct cytosolic

1372   complexes. Open Biol. *4*, 140120.

1373   Gibson, D.G., Young, L., Chuang, R.Y., Venter, J.C., Hutchison, C.A., and Smith, H.O. (2009).

1374   Enzymatic assembly of DNA molecules up to several hundred kilobases. Nat. Methods *6*,

1375   343–345.

1376   Gibson, T.J., Seiler, M., and Veitia, R.A. (2013). The transience of transient overexpression.

1377   Nat. Methods *10*, 715–721.

1378   Goedhart, J. (2019). PlotsOfDifferences - a web app for the quantitative comparison of

1379   unpaired data. BioRxiv 578575.

1380   Goedhart, J., von Stetten, D., Noirclerc-Savoye, M., Lelimousin, M., Joosen, L., Hink, M.A.,

1381   van Weeren, L., Gadella, T.W.J., and Royant, A. (2012). Structure-guided evolution of cyan

1382   fluorescent proteins towards a quantum yield of 93%. Nat. Commun. *3*, 751.

1383   Gottardi, C.J., and Gumbiner, B.M. (2004). Distinct molecular forms of β-catenin are

1384   targeted to adhesive or transcriptional complexes. J. Cell Biol. *167*, 339–349.

1385   Hampf, M., and Gossen, M. (2006). A protocol for combined Photinus and Renilla luciferase

1386   quantification compatible with protein assays. Anal. Biochem. *356*, 94–99.

1387   Hendriksen, J., Jansen, M., Brown, C.M., van der Velde, H., van Ham, M., Galjart, N.,

1388   Offerhaus, G.J., Fagotto, F., and Fornerod, M. (2008). Plasma membrane recruitment of

1389   dephosphorylated β-catenin upon activation of the Wnt pathway. J. Cell Sci. *121*, 1793–

1390   1802.

1391   Hink, M. a. (2014). Quantifying intracellular dynamics using fluorescence fluctuation

1392   spectroscopy. Protoplasma *251*, 307–316.

1393   Holstein, T.W. (2012). The evolution of the wnt pathway. Cold Spring Harb. Perspect. Biol. *4*,

1394   1–17.

1395   Holzmann, J., Politi, A.Z., Nagasaka, K., Hantsche-Grininger, M., Walther, N., Koch, B., Fuchs,

1396   J., Dürnberger, G., Tang, W., Ladurner, R., et al. (2019). Absolute quantification of cohesin,

1397   CTCF and their regulators in human cells. Elife *8*, 1–31.

1398   Hu, M., Kurobe, M., Jeong, Y.J., Fuerer, C., Ghole, S., Nusse, R., and Sylvester, K.G. (2007).

1399   Wnt/β-catenin signaling in murine hepatic transit amplifying progenitor cells.

1400   Gastroenterology *133*, 1579–1591.

1401   Jacobsen, A., Heijmans, N., Verkaar, F., Smit, M.J., Heringa, J., van Amerongen, R., and

1402   Feenstra, K.A. (2016). Construction and experimental validation of a Petri net model of

1403   Wnt/β-catenin signaling. PLoS One *11*, 1–30.

1404   Jamieson, C., Sharma, M., and Henderson, B.R. (2011). Regulation of β-catenin nuclear

1405   dynamics by GSK-3β involves a LEF-1 positive feedback loop. Traffic *12*, 983–999.

1406   Kafri, P., Hasenson, S.E., Kanter, I., Sheinberger, J., Kinor, N., Yunger, S., and Shav-Tal, Y.

1407   (2016). Quantifying β-catenin subcellular dynamics and cyclin D1 mRNA transcription during

1408   Wnt signaling in single living cells. Elife *5*, 1–29.

1409   Kaur, G., Costa, M.W., Nefzger, C.M., Silva, J., Fierro-González, J.C., Polo, J.M., Bell,

1410   T.D.M.M., and Plachta, N. (2013). Probing transcription factor diffusion dynamics in the

1411   living mammalian embryo with photoactivatable fluorescence correlation spectroscopy.

1412   Nat. Commun. *4*, 1637.

1413   Kitazawa, M., Hatta, T., Ogawa, K., Fukuda, E., Goshima, N., and Natsume, T. (2017).

1414   Determination of rate-limiting factor for formation of beta-catenin destruction complexes

1415   using absolute protein quantification. J. Proteome Res. *16*, 3576–3584.

1416   Kormish, J.D., Sinner, D., and Zorn, A.M. (2010). Interactions between SOX factors and

1417   Wnt/β-catenin signaling in development and disease. Dev. Dyn. *239*, 56–68.

1418   Kotecki, M., Reddy, P.S.S., and Cochran, B.H. (1999). Isolation and characterization of a near-

1419   haploid human cell line. Exp. Cell Res. *252*, 273–280.

1420   Kremers, G.-J., Goedhart, J., van den Heuvel, D.J., Gerritsen, H.C., and Gadella, T.W.J. (2007).

1421   Improved green and blue fluorescent proteins for expression in bacteria and mammalian

1422   cells. Biochemistry *46*, 3775–3783.

1423   Kremers, G.J., Goedhart, J., Van Munster, E.B., Gadella, T.W.J.J., Munster, E.B. Van, and

1424   Gadella, T.W.J.J. (2006). Cyan and yellow super fluorescent proteins with improved

1425   brightness , protein folding , and FRET förster radius. Biochemistry *45*, 6570–6580.

1426   Krieghoff, E., Behrens, J., and Mayr, B. (2006). Nucleo-cytoplasmic distribution of β-catenin

1427   is regulated by retention. J. Cell Sci. *119*, 1453–1463.

1428   Kunttas-Tatli, E., Roberts, D.M., and McCartney, B.M. (2014). Self-association of the APC

1429   tumor suppressor is required for the assembly, stability, and activity of the Wnt signaling

1430   destruction complex. Mol. Biol. Cell *25*, 3424–3436.

1431   Lam, C.S., Mistri, T.K., Foo, Y.H., Sudhaharan, T., Gan, H.T., Rodda, D., Lim, L.H., Chou, C.,

1432   Robson, P., Wohland, T., et al. (2012). DNA-dependent Oct4-Sox2 interaction and diffusion

1433   properties characteristic of the pluripotent cell state revealed by fluorescence spectroscopy.

1434   Biochem. J. *448*, 21–33.

1435   Latres, E., Chiaur, D.S., and Pagano, M. (1999). The human F box protein β-Trcp associates

1436   with the Cul1/Skp1 complex and regulates the stability of β-catenin. Oncogene *18*, 849–854.

1437   Lebensohn, A.A.M., Dubey, R., Neitzel, L.R., Tacchelly-Benites, O., Yang, E., Marceau, C.D.,

1438   Davis, E.M., Patel, B.B., Bahrami-Nejad, Z., Travaglini, K.J., et al. (2016). Comparative genetic

1439   screens in human cells reveal new regulatory mechanisms in WNT signaling. Elife *5*, e21459.

1440   Lee, E., Salic, A., Krüger, R., Heinrich, R., and Kirschner, M.W. (2003). The roles of APC and

1441   axin derived from experimental and theoretical analysis of the Wnt pathway. PLoS Biol. *1*,

1442   116–132.

1443   Li, V.S.W., Ng, S.S., Boersema, P.J., Low, T.Y., Karthaus, W.R., Gerlach, J.P., Mohammed, S.,

1444   Heck, A.J.R., Maurice, M.M., Mahmoudi, T., et al. (2012). Wnt signaling through inhibition of

1445   β-catenin degradation in an intact Axin1 complex. Cell *149*, 1245–1256.

1446   Lim, X., Tan, S., Koh, W.W.L.C., Chau, R., Yan, K., Kuo, C.J., van Amerongen, R., Klein, A.M.,

1447   and Nusse, R. (2013). Interfollicular epidermal stem cells self-renew via autocrine Wnt

1448   signaling. Science (80-.). *342*, 1226–1230.

1449   Liu, C., Li, Y., Semenov, M., Han, C., Baeg, G.-H.H., Tan, Y., Zhang, Z., Lin, X., and He, X.

1450   (2002). Control of β-catenin phosphorylation/degradation by a dual-kinase mechanism. Cell

1451   *108*, 837–847.

1452   Liu, X., Rubin, J.S., and Kimmel, A.R. (2005). Rapid, Wnt-induced changes in GSK3β

1453   associations that regulate β-catenin stabilization are mediated by Gα proteins. Curr. Biol. *15*,

1454   1989–1997.

1455   Livak, K.J., and Schmittgen, T.D. (2001). Analysis of relative gene expression data using real-

1456   time quantitative PCR and the 2-ΔΔCT method. Methods *25*, 402–408.

1457   Loh, K.M., van Amerongen, R., and Nusse, R. (2016). Generating cellular diversity and spatial

1458   form: Wnt signaling and the evolution of multicellular animals. Dev. Cell *38*, 643–655.

1459   Lui, T.T.H., Lacroix, C., Ahmed, S.M., Goldenberg, S.J., Leach, C.A., Daulat, A.M., and Angers,

1460   S. (2011). The ubiquitin-specific protease USP34 regulates Axin stability and Wnt/β-Catenin

1461   Signaling. Mol. Cell. Biol. *31*, 2053–2065.

1462   Lustig, B., Jerchow, B., Sachs, M., Weiler, S., Pietsch, T., Karsten, U., van de Wetering, M.,

1463   Clevers, H., Schlag, P.M., Birchmeier, W., et al. (2002). Negative feedback loop of Wnt

1464   signaling through upregulation of conductin/axin2 in colorectal and liver tumors. Mol. Cell.

1465   Biol. *22*, 1184–1193.

1466   Macháň, R., and Wohland, T. (2014). Recent applications of fluorescence correlation

1467   spectroscopy in live systems. FEBS Lett. *588*, 3571–3584.

1468   Mahen, R., Koch, B., Wachsmuth, M., Politi, A.Z., Perez-gonzalez, A., Mergenthaler, J., Cai, Y.,

1469   Ellenberg, J., and Lippincott-schwartz, J. (2014). Comparative assessment of fluorescent

1470   transgene methods for quantitative imaging in human cells. Mol. Biol. Cell *25*, 3610–3618.

1471   Maher, M.T., Mo, R., Flozak, A.S., Peled, O.N., and Gottardi, C.J. (2010). β-Catenin

1472   phosphorylated at Serine 45 is spatially uncoupled from β-Catenin phosphorylated in the

1473   GSK3 domain: Implications for signaling. PLoS One *5*, e10184.

1474   Massey, J., Liu, Y., Alvarenga, O., Saez, T., Schmerer, M., and Warmflash, A. (2019). Synergy

1475   with TGFβ ligands switches WNT pathway dynamics from transient to sustained during

1476   human pluripotent cell differentiation. Proc. Natl. Acad. Sci. U. S. A. *116*, 4989–4998.

1477   Mendoza-Topaz, C., Mieszczanek, J., and Bienz, M. (2011). The Adenomatous polyposis coli

1478   tumour suppressor is essential for Axin complex assembly and function and opposes Axin's

1479   interaction with Dishevelled. Open Biol. *1*, 110013.

1480   Molenaar, M., van de Wetering, M., Oosterwegel, M., Peterson-Maduro, J., Godsave, S.,

1481   Korinek, V., Roose, J., Destrée, O., and Clevers, H. (1996). XTcf-3 transcription factor

1482   mediates beta-catenin-induced axis formation in Xenopus embryos. Cell *86*, 391–399.

1483   Morin, P.J., Sparks, A.B., Korinek, V., Barker, N., Clevers, H., Vogelstein, B., and Kinzler, K.W.

1484   (1997). Activation of β-catenin-Tcf signaling in colon cancer by mutations in β-catenin or

1485   APC. Science (80-.).

1486   Nusse, R., and Clevers, H. (2017). Wnt/β-Catenin signaling, disease, and emerging

1487   therapeutic modalities. Cell *169*, 985–999.

1488   Pack, C., Saito, K., Tamura, M., and Kinjo, M. (2006). Microenvironment and effect of energy

1489   depletion in the nucleus analyzed by mobility of multiple oligomeric EGFPs. Biophys. J. *91*,

1490   3921–3936.

1491   Pack, C.G., Yukii, H., Toh-E, A., Kudo, T., Tsuchiya, H., Kaiho, A., Sakata, E., Murata, S.,

1492   Yokosawa, H., Sako, Y., et al. (2014). Quantitative live-cell imaging reveals spatio-temporal

1493   dynamics and cytoplasmic assembly of the 26S proteasome. Nat. Commun. *5*, 3396.

1494   Petrášek, Z., and Schwille, P. (2008). Precise measurement of diffusion coefficients using

1495   scanning fluorescence correlation spectroscopy. Biophys. J. *94*, 1437–1448.

1496   Polakis, P. (2000). Wnt signaling and cancer. Genes Dev. *14*, 1837–1851.

1497   Pronobis, M.I., Rusan, N.M., and Peifer, M. (2015). A novel GSK3-regulated APC:Axin

1498   interaction regulates Wnt signaling by driving a catalytic cycle of efficient βcatenin

1499   destruction. Elife *4*, 1–31.

1500   Pronobis, M.I., Deuitch, N., Posham, V., Mimori-Kiyosue, Y., and Peifer, M. (2017).

1501   Reconstituting regulation of the canonical Wnt pathway by engineering a minimal β-catenin

1502   destruction machine. Mol. Biol. Cell *28*, 41–53.

1503   Ran, F.A., Hsu, P.D., Wright, J., Agarwala, V., Scott, D. a, and Zhang, F. (2013). Genome

1504   engineering using the CRISPR-Cas9 system. Nat. Protoc. *8*, 2281–2308.

1505   Rim, E.Y., Kinney, L.K., and Nusse, R. (2020). Beta-catenin-mediated Wnt signal transduction

1506   proceeds through an endocytosis-independent mechanism. Mol. Biol. Cell mbc.E20-02-

1507   0114.

1508   Sayat, R., Leber, B., Grubac, V., Wiltshire, L., and Persad, S. (2008). O-GlcNAc-glycosylation of

1509   β-catenin regulates its nuclear localization and transcriptional activity. Exp. Cell Res. *314*,

1510   2774–2787.

1511   Schaefer, K.N., and Peifer, M. (2019). Wnt/beta-catenin signaling regulation and a role for

1512   biomolecular condensates. Dev. Cell *48*, 429–444.

1513   Schaefer, K.N., Bonello, T.T., Zhang, S., Williams, C.E., Roberts, D.M., McKay, D.J., and Peifer,

1514   M. (2018). Supramolecular assembly of the beta-catenin destruction complex and the effect

1515   of Wnt signaling on its localitzation, molecular size, and activity in vivo.

1516   Schaefer, K.N., Pronobis, M., Williams, C.E., Zhang, S., Bauer, L., Goldfarb, D., Yan, F., Major,

1517   M. Ben, and Peifer, M. (2020). Wnt regulation: Exploring Axin-Disheveled interactions and

1518   defining mechanisms by which the SCF E3 ubiquitin ligase is recruited to the destruction

1519   complex. Mol. Biol. Cell mbcE19110647.

1520   Schmittgen, T.D., and Livak, K.J. (2008). Analyzing real-time PCR data by the comparative CT

1521   method. Nat. Protoc. *3*, 1101–1108.

1522   Schmitz, Y., Rateitschak, K., and Wolkenhauer, O. (2013). Analysing the impact of nucleo-

1523   cytoplasmic shuttling of β-catenin and its antagonists APC, Axin and GSK3 on Wnt/β-catenin

1524   signalling. Cell. Signal. *25*, 2210–2221.

1525   Schuijers, J., Mokry, M., Hatzis, P., Cuppen, E., and Clevers, H. (2014). Wnt-induced

1526   transcriptional activation is exclusively mediated by TCF/LEF. EMBO J. *33*, 146–156.

1527   Schwarz-Romond, T., Fiedler, M., Shibata, N., Butler, P.J.G., Kikuchi, A., Higuchi, Y., and

1528   Bienz, M. (2007). The DIX domain of Dishevelled confers Wnt signaling by dynamic

1529   polymerization. Nat. Struct. Mol. Biol. *14*, 484–492.

1530   Spink, K.E., Polakis, P., and Weis, W.I. (2000). Structural basis of the Axin–adenomatous

1531   polyposis coli interaction. EMBO J. *19*, 2270–2279.

1532   Stamos, J.L., Chu, M.L.-H.H., Enos, M.D., Shah, N., and Weis, W.I. (2014). Structural basis of

1533   GSK-3 inhibition by N-terminal phosphorylation and by the Wnt receptor LRP6. Elife *2014*,

1534   e01998.

1535   Taelman, V.F., Dobrowolski, R., Plouhinec, J.L., Fuentealba, L.C., Vorwald, P.P., Gumper, I.,

1536   Sabatini, D.D., and De Robertis, E.M. (2010). Wnt signaling requires sequestration of

1537   Glycogen Synthase Kinase 3 inside multivesicular endosomes. Cell *143*, 1136–1148.

1538   Tan, C.W., Gardiner, B.S., Hirokawa, Y., Layton, M.J., Smith, D.W., and Burgess, A.W. (2012).

1539   Wnt signalling pathway parameters for mammalian cells. PLoS One *7*, 31882.

1540   Tan, C.W., Gardiner, B.S., Hirokawa, Y., Smith, D.W., and Burgess, A.W. (2014). Analysis of

1541   Wnt signaling β-catenin spatial dynamics in HEK293T cells. BMC Syst. Biol. *8*, 44.

1542   Thorvaldsen, T.E., Pedersen, N.M., Wenzel, E.M., Schultz, S.W., Brech, A., Liestøl, K., Waaler,

1543   J., Krauss, S., and Stenmark, H. (2015). Structure, dynamics, and functionality of tankyrase

1544   inhibitor-induced degradasomes. Mol. Cancer Res. *13*, 1487–1501.

1545   van Tienen, L.M., Mieszczanek, J., Fiedler, M., Rutherford, T.J., and Bienz, M. (2017).

1546   Constitutive scaffolding of multiple Wnt enhanceosome components by legless/BCL9. Elife

1547   *6*, 1–23.

1548   Tortelote, G.G., Reis, R.R., de Almeida Mendes, F., and Abreu, J.G. (2017). Complexity of the

1549   Wnt/β-catenin pathway: Searching for an activation model. Cell. Signal. *40*, 30–43.

1550   Tran, H., and Polakis, P. (2012). Reversible modification of adenomatous polyposis coli (APC)

1551   with K63-linked polyubiquitin regulates the assembly and activity of the β-catenin

1552   destruction complex. J. Biol. Chem. *287*, 28552–28563.

1553   Valenta, T., Hausmann, G., and Basler, K. (2012). The many faces and functions of β-catenin.

1554   EMBO J. *31*, 2714–2736.

1555   Verkaar, F., Cadigan, K.M., and van Amerongen, R. (2012). Celebrating 30 years of Wnt

1556   signaling. Sci. Signal. *5*, mr2.

1557   Wachsmuth, M., Waldeck, W., and Langowski, J. (2000). Anomalous diffusion of fluorescent

1558   probes inside living cell investigated by spatially-resolved fluorescence correlation

1559   spectroscopy. J. Mol. Biol. *298*, 677–689.

1560   van der Wal, T., and van Amerongen, R. (2020). Walking the tight wire between cell

1561   adhesion and WNT signalling: a balancing act for β-catenin. Open Biol. *10*, 200267.

1562   Wiechens, N., and Fagotto, F. (2001). CRM1- and Ran-independent nuclear export of β-

1563   catenin. Curr. Biol. *11*, 18–28.

1564   Wiese, K.E., Nusse, R., and van Amerongen, R. (2018). Wnt signalling: conquering

1565   complexity. Development *145*, dev165902.

1566   Wu, X., Tu, X., Joeng, K.S., Hilton, M.J., Williams, D.A., and Long, F. (2008). Rac1 Activation

1567   Controls Nuclear Localization of β-catenin during Canonical Wnt Signaling. Cell *133*, 340–

1568   353.

1569   Yaguchi, K., Yamamoto, T., Matsui, R., Tsukada, Y., Shibanuma, A., Kamimura, K., Koda, T.,

1570   and Uehara, R. (2018). Uncoordinated centrosome cycle underlies the instability of non-

1571   diploid somatic cells in mammals. J. Cell Biol. *217*, 2463–2483.

1572   Yap, A.S., Brieher, W.M., and Gumbiner, B.M. (1997). Molecular and functional analysis of

1573   cadherin-based adherens junctions. Annu. Rev. Cell Dev. Biol. *13*, 119–146.

1574   Yokoya, F., Imamoto, N., Tachibana, T., and Yoneda, Y. (1999). β-Catenin can be transported

1575   into the nucleus in a ran-unassisted manner. Mol. Biol. Cell *10*, 1119–1131.

1576   Yokoyama, N., Markova, N.G., Wang, H., and Malbon, C.C. (2012). Assembly of Dishevelled

1577   3-based supermolecular complexes via phosphorylation and Axin. J. Mol. Signal. *7*, 8.

1578   Zhan, T., Rindtorff, N., and Boutros, M. (2017). Wnt signaling in cancer. Oncogene *36*, 1461–

1579   1473.

1580